Scilight

Sustainable Engineering Novit
https://www.sciltp.com/journals/sen



Review

Check for updates

Highly Stable and Practical Sodium-Ion Batteries: Key Materials, Electrode Engineering, Manufacturing, and Prospects

Lu Yue [1,*], Yujie Zhang [1], Jiajun Wan [1], Guoxu Nie [1], Huajun Zhao [1], Wenhui Zhang [1,*] and Huaiyu Shao [2,*]

[1] Department of Physics, Yancheng Institute of Technology, Yancheng 224051, China
[2] Institute of Applied Physics and Materials Engineering (IAPME), University of Macau, Macau, SAR, China
* Correspondence: yuelu66@126.com (L.Y.); zwhuizi000@sina.com (W.Z.); huaiyu.shao@um.edu.mo (H.S.)

How To Cite: Yue, L.; Zhang, Y.; Wan, J.; et al. Highly Stable and Practical Sodium-Ion Batteries: Key Materials, Electrode Engineering, Manufacturing, and Prospects. *Sustainable Engineering Novit* **2026**, *2*(4), 1. https://doi.org/10.53941/sen.2026.100015

Received: 30 June 2026
Revised: 10 September 2026
Accepted: 29 September 2026
Published: 16 November 2026

Abstract: Sodium-ion batteries (SIBs) are promising for large-scale energy storage owing to abundant sodium resources, low cost, and good manufacturing compatibility. However, their practical application remains limited by the structural stability of key materials, interfacial side reactions, cycle life, and safety. This review focuses on highly stable and practical SIBs and systematically summarizes the main failure mechanisms and stabilization strategies of cathode materials, anode materials, and electrolyte/electrode interfaces. Particular attention is paid to phase-transition suppression in layered oxides, framework strengthening of polyanionic compounds, defect regulation in Prussian blue/white materials, closed-pore structure optimization of hard carbon, solid electrolyte interphase (SEI)/cathode electrolyte interphase (CEI) formation, and interfacial stability of solid-state electrolytes. In addition, engineering strategies such as thick-electrode design, dry electrode manufacturing, thermal management, adaptive binders, and digital twin technologies are discussed from the perspective of material–electrode–device integration. Distinct from reviews centered on individual material classes, this work connects key-material failure mechanisms with electrode architecture, manufacturing, safety management, and industrialization, providing a full-chain materials–electrode–device–manufacturing perspective. Future efforts should focus on interfacial controllability, manufacturing consistency, and recycling sustainability to accelerate the large-scale application of SIBs.

Keywords: sodium-ion batteries; cathode materials; hard carbon anodes; electrolyte interface; stabilization strategies; engineering application

1. Introduction

The rapid deployment of intermittent renewable power and transport electrification is increasing demand for low-cost, long-life energy storage [1–3]. Although lithium-ion batteries dominate current markets, the concentration and price volatility of Li/Ni/Co resources motivate complementary chemistries for terawatt-hour-scale deployment [4,5].

Sodium-ion batteries (SIBs) are attractive because sodium is abundant, Fe/Mn-rich chemistries can reduce raw-material cost, and many manufacturing steps are compatible with existing Li-ion production lines [4,6–9]. In addition, the standard electrode potential of Na (−2.71 V) vs. the standard hydrogen electrode (SHE) supports competitive cell voltages while avoiding some of the resource constraints of lithium-based systems [8,9].

Copyright: © 2026 by the authors. This is an open access article under the terms and conditions of the Creative Commons Attribution (CC BY) license (https://creativecommons.org/licenses/by/4.0/).
Publisher's Note: Scilight stays neutral with regard to jurisdictional claims in published maps and institutional affiliations.

Substantial progress has already been made in the industrialization of SIBs. Commercial specifications have been achieved for cells at the 160 Wh kg^{-1} level, and SIBs using Prussian blue analogues (PBAs) as cathodes have begun to be used as backup power sources in scenarios such as data centers [8]. Despite their resource and cost advantages, stability remains a central bottleneck in the transition from laboratory performance to large-scale application. Layered-oxide cathodes can undergo phase transitions and structural collapse under deep desodiation [10,11], polyanionic compounds are limited by low electronic conductivity [12], and PBAs are sensitive to lattice water and defects [13]. Hard carbon anodes suffer irreversible Na consumption associated with defect/surface adsorption, electrolyte decomposition, and solid electrolyte interphase (SEI) formation/evolution [14–16], while alloy anodes undergo severe volume expansion [17]. Liquid electrolytes can form unstable interphases and solid-state systems still face substantial interfacial resistance [13,18]. These coupled material and interface limitations continue to constrain cycle life, energy efficiency, and manufacturing consistency [19,20].

Practical evaluation therefore requires a multiscale framework that links atomistic/interfacial degradation with cell-level lifetime, safety, and manufacturability. Advanced tools such as scanning transmission electron microscopy–electron energy-loss spectroscopy (STEM-EELS) and nanoscale electrochemical probes can resolve oxygen-vacancy and SEI evolution [21–23], while electrochemical–thermal coupled models quantify module-level heat-transfer requirements [24]. At the same time, standardized SIB-specific protocols remain incomplete: grid-storage protocols developed by Pacific Northwest National Laboratory (PNNL), traction-battery standards such as International Electrotechnical Commission (IEC) 62660, and emerging resources including BatteryLife and TWAICE provide useful starting points but do not yet fully capture sodium-specific degradation [25–33].

Accordingly, this review establishes a three-dimensional evaluation framework based on cycle life, safety, and system cost; analyzes key failure mechanisms in cathodes, anodes, and electrolytes; summarizes stabilization strategies including surface passivation, grain-boundary engineering, interfacial-chemistry modification, and high-entropy multicomponent design; and then extends the discussion to electrode architecture, dry processing, thermal management, digitalized manufacturing, cost reduction, and recycling. Compared with recent reviews centered on individual cathode families, hard carbon, or specific production challenges [6–9,12,13], the present review therefore provides a full-chain materials–electrode–device–manufacturing perspective that connects microscopic stability with practical implementation (Figure 1).

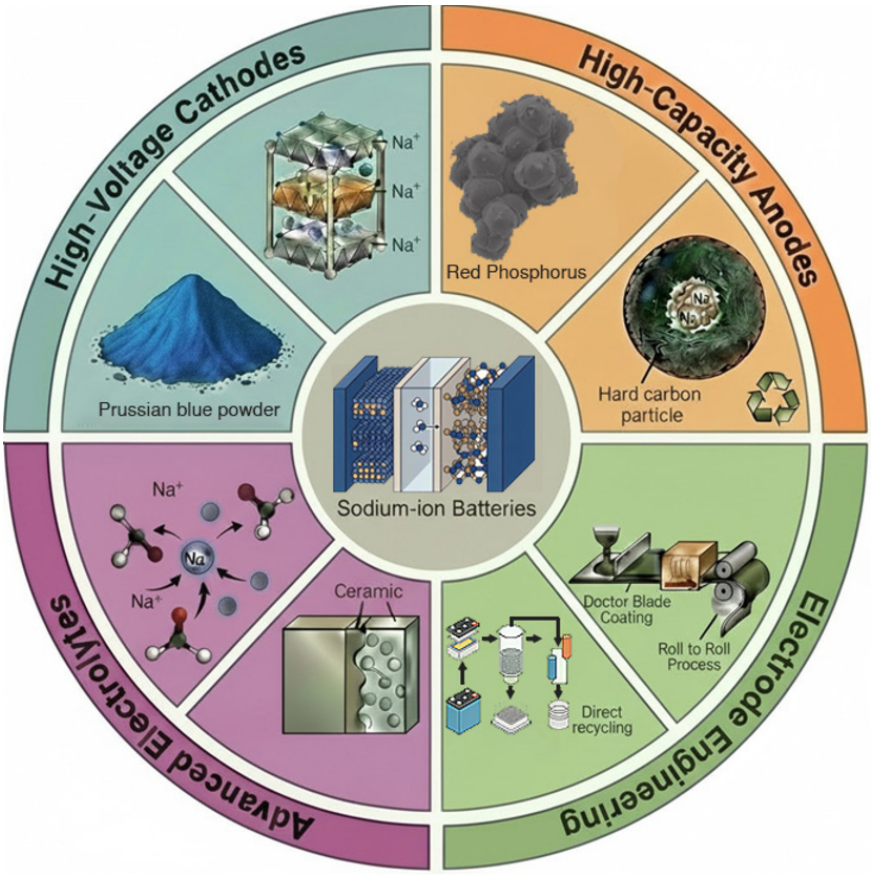


Figure 1. Overview of technological development for practical sodium-ion batteries: from key materials to energy-storage applications.

2. Failure Mechanisms of Key Materials and Advanced Stabilization Strategies

The practical development of SIBs is restricted by multiscale failure behavior in their material systems. Cathodes face phase-transition-induced structural collapse under deep desodiation, anode interfaces suffer from irreversible sodium loss and continuous SEI evolution, and electrolytes must simultaneously address dendrite growth and interfacial transport barriers. Starting from atomistic mechanism analysis, this section systematically reveals crystal distortion in layered oxides, closed-pore storage kinetics in hard carbon, and solvation-sheath reconstruction, while reviewing breakthrough stabilization strategies such as surface passivation, grain-boundary engineering, and interfacial-chemistry modification. These multidimensional, synergistic innovations not only provide theoretical benchmarks for material design but also establish a scientific bridge for building highly cyclable battery systems from laboratory research to industrialization (Figure 2).

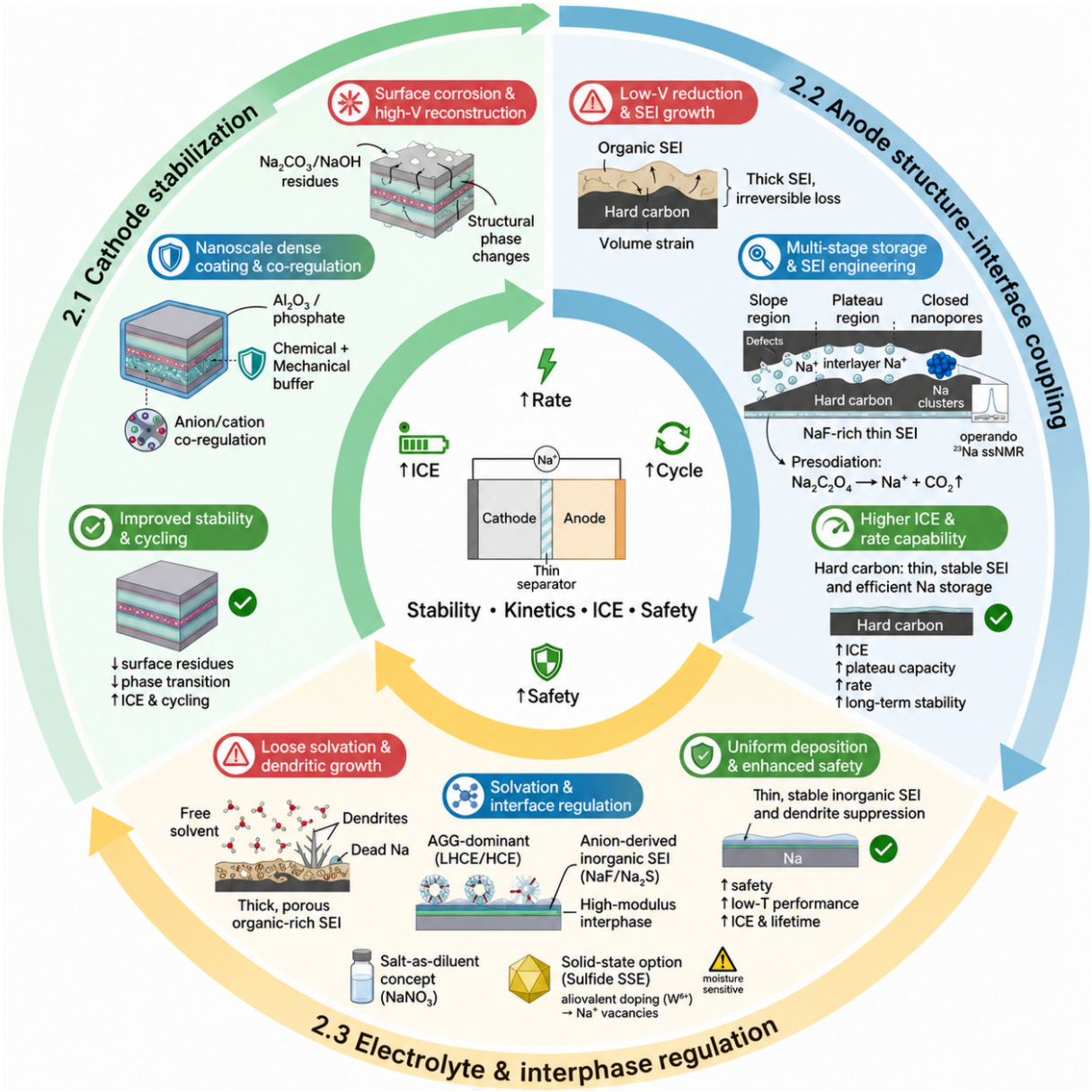


Figure 2. Schematic illustration of full-chain stability enhancement in sodium-ion batteries.

2.1. Cathode Materials: Failure Mechanisms, Structural Degradation, and Stabilization Strategies

As the core determinant of energy density and cost in SIBs, the structural stability of cathode materials directly governs cell cycle life and industrial viability. Layered transition-metal oxides, Na_xTMO_2 (TM = transition metal), are widely regarded as one of the most promising high-energy-density cathode families for SIBs because of their specific capacities of 120–180 mAh g^{-1} and tunable voltage plateaus of 2.5–3.8 V [6,34]. However, in the deep-desodiation region ($x \leq 0.4$–0.5), these materials often undergo multistep structural transformations from O3 to P3/OP4 and ultimately to a rock-salt phase, accompanied by c-axis contraction and rearrangement of the local

coordination environment, resulting in irreversible structural degradation of the electrode [35]. Atomistic theoretical and experimental studies show that increasing vacancy concentration in the Na layer promotes transition-metal (TM) interlayer migration and irreversible structural evolution. In $NaCrO_2$, after deep charge with extraction of more than 0.5 Na, TMs can occupy tetrahedral/octahedral sites in the Na layer, accompanied by irreversible phase transitions and lattice contraction along the c-axis. Similarly, in Fe-containing O3 layered oxides, atomic-resolution STEM directly confirms TM, especially Fe, migration into the Na layer after charging. Migrated TMs occupying tetrahedral and octahedral interstitial sites in the Na layer can form local spinel-like rearrangements, blocking Na^+ diffusion channels and accelerating performance decay. Studies of biphasic structures also show that high-voltage deep desodiation is often accompanied by abnormal interlayer contraction; for example, the c parameter decreases abnormally in the 4.0–4.3 V range and may induce phase transition [36,37]. This chain degradation mechanism of increased Na vacancies, c-axis contraction, reduced TM migration barriers, and rock-salt transformation has been systematically verified in representative systems such as $NaFeO_2$ and Na_xCrO_2 by in situ/ex situ X-ray diffraction (XRD), STEM-EELS, and first-principles calculations, providing clear targets for subsequent stabilization design [38].

In Situ high-energy X-ray diffraction (HEXRD) and transmission electron microscopy (TEM) results show that even in single-crystalline or high-quality-grained P2 phases, lattice thermal expansion/contraction induced by heat treatment or cycling exhibits anisotropic changes along the a and c axes, suggesting possible stress accumulation within particles and at grain boundaries [39]. Furthermore, with increasing Na^+/vacancy ordering, desodiation degree, or high-voltage charging (>4.2 V), the P2 phase is prone to transform into high-voltage phases such as P2′, OP4, or O2. These phase transitions are accompanied by drastic changes in interlayer spacing and lattice parameters, which seed structural instability and capacity decay [40]. To mitigate these unfavorable phase transitions and structural damage, recent studies have proposed heteroatom doping (e.g., Ti + Zn co-doping or high-valence W doping), combined with Na-site regulation and surface protective layers, to effectively suppress P2-to-O2 transformation, reduce Na^+/vacancy ordering, and enhance ion diffusion and structural reversibility, thereby markedly improving cycle stability and high-voltage performance [41,42]. Accordingly, the physical picture of cycling failure in layered Na_xTMO_2 has evolved from a simple "phase transition to macroscopic capacity decay" model to a coupled atom/ion/lattice-particle-grain-boundary-microcrack multiscale failure mechanism: high voltage/deep desodiation induces phase transition and anisotropic lattice strain, followed by stress/cracking and loss of active-material connectivity or blockage of ion channels.

To address the above issues, relatively mature stabilization strategies have been developed along two main directions: surface engineering and synergistic anion/cation regulation. Among them, the design of surface passivation layers serves as the first line of defense against air/moisture sensitivity and parasitic interfacial reactions. Recent studies have shown that constructing a nanometer-scale compact inorganic layer, such as Al_2O_3 or phosphate, on the surface of P2-type Na-based layered oxides, particularly Ni/Mn-containing systems, can effectively suppress the formation of alkaline by-products, including Na_2CO_3 and NaOH, induced by H_2O/CO_2 exposure (Figure 3a). This strategy also enables the recovery of initial Coulombic efficiency and rate/long-term cycling stability after aqueous slurry processing or exposure to humid environments. For example, the introduction of uniform phosphate coatings, such as $AlPO_4$ and Na_3PO_4, or analogous ion-conductive interlayers on P2 cathodes can reduce interfacial resistance and mitigate phase-transition- or stress-induced structural reconstruction (Figure 3b), thereby maintaining more than 90% capacity retention during long-term cycling at the 1C rate. For O3-type Na_xTMO_2 cathodes, the application of uniform Al_2O_3 coatings or surface-reconstructed $NaCaPO_4$ coatings under high cutoff voltages (≥4.0 V) can suppress high-voltage phase-boundary migration and particle pulverization, consume residual surface Na species, and improve Coulombic efficiency and capacity retention (Figure 3c). These effects demonstrate a dual "chemical–mechanical" buffering function (Figure 3d) [43,44].

Taking layered O3-type Na_xTMO_2 cathodes as an example, surface oxide coatings, such as Al_2O_3, are commonly employed to simultaneously enhance interfacial chemical stability and structural mechanical robustness, thereby improving cycling lifespan and rate capability. Zhao et al. [44] used $Al(OH)_3$ as the precursor in an O3–$NaNi_{1/3}Fe_{1/3}Mn_{1/3}O_2$ system, followed by grinding/mixing and thermal treatment, to construct a uniform Al_2O_3 protective layer in situ on the particle surface. In terms of long-term cycling performance, the sample coated with 0.5 wt% Al_2O_3 delivered a capacity retention of 60.7% after 200 cycles at 1C, representing an 18.4% improvement compared with the uncoated sample (Figure 3e). This indicates that the coating layer not only blocks environmental corrosion and direct electrolyte attack on active particles, but also functions as a "mechanical buffer layer" during phase transitions and stress concentration, thereby delaying lattice oxygen release and surface structural reconstruction (Figure 3f). Recent studies on O3-type Na_xTMO_2 cathodes have further confirmed that uniform Al_2O_3 coating can inhibit phase-boundary migration and particle pulverization during high-voltage cycling,

allowing O3 materials to maintain high capacity retention and Coulombic efficiency within a voltage window of 2.0–4.0 V [44].

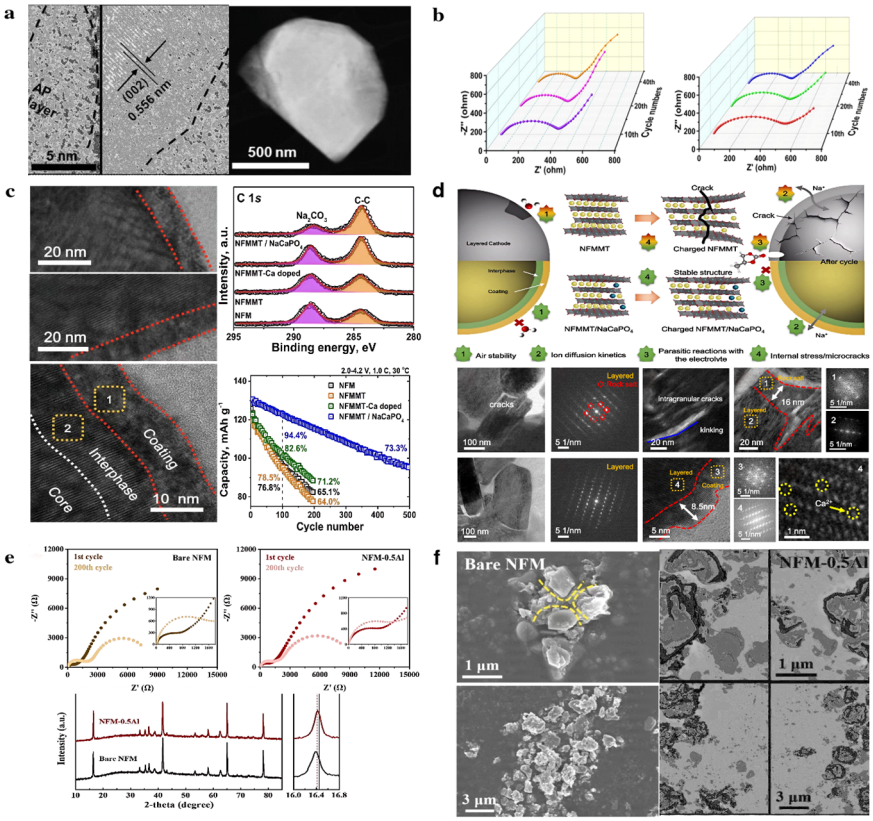


Figure 3. Surface-engineering strategies for layered oxide cathodes. (**a**) In Situ construction and morphology of a compact amorphous $AlPO_4$ (AP) nanolayer on a P2-type layered cathode; (**b**) electrochemical impedance spectroscopy (EIS)-tracked electrode/electrolyte interfacial resistance during cycling of the AP-coated P2 cathode. Reprinted with permission from Ref. [45]. Copyright 2024, Journal of Energy Chemistry; (**c**) "core–interfacial layer–coating" architecture of a $NaCaPO_4$ surface-reconstructed O3-type layered cathode, suppressing surface Na_2CO_3 formation; (**d**) corresponding interfacial-chemistry/crack-resistance mechanism under high-voltage cycling (≥4.0 V). Reprinted with permission from Ref. [43]. Copyright 2025, Nature Communications; (**e**) interfacial impedance and structural evolution of O3-$NaNi_{1/3}Fe_{1/3}Mn_{1/3}O_2$ (NFM) with 0.5 wt% Al_2O_3; (**f**) scanning electron microscopy (SEM) comparison of pristine NFM and NFM-0.5Al after 200 cycles at 1C (2.0–4.0 V). Reprinted with permission from Ref. [44]. Copyright 2025, Journal of Energy Storage.

On this basis, synergistic anion and cation doping has been employed to reconstruct the electronic and crystal structures of layered oxides from an intrinsic perspective, thereby enhancing their inherent structural stability. For instance, introducing F^- doping or Ti^{4+}/F^- co-doping into P2–$Na_{0.67}Ni_{0.33}Mn_{0.67}O_2$ can effectively strengthen TM–F bonding. Computational results indicate that partial substitution of O^{2-} by F^- increases the local bond energy by approximately 30% and raises the oxygen vacancy formation energy from ~1.5 eV to ~2.5 eV, thereby significantly suppressing irreversible lattice oxygen release at high voltages [46,47].

In terms of cathode composition design, entropy-mediated multication regulation has emerged as an effective strategy for enhancing the structural robustness of P2-type layered oxide cathodes. Compared with conventional single- or dual-cation systems, high-entropy configurations can increase configurational entropy and create highly diversified local coordination environments, thereby reducing the energetic driving force for cation ordering, transition-metal migration, and phase-boundary propagation. Recent first-principles and electrochemical analyses reveal that high configurational entropy can effectively mitigate transition-metal-centered octahedral distortion, suppress shear-type lattice deformation associated with P2→O2 layer gliding, and distribute charge compensation over multiple redox-active cations. Such entropy-stabilized structural and electronic regulation alleviates local over-oxidation, lattice strain accumulation, and irreversible phase evolution during high-voltage cycling, providing a mechanistic basis for the design of durable layered oxide cathodes for sodium-ion batteries [48]. In the O3–$Na_{1-x}[Ni_{0.33}Mn_{0.67}]O_2$ system, the synergistic strategy of high-valence Mo regulation and Mg doping can increase the oxygen vacancy formation energy, weaken the involvement of lattice oxygen and the tendency of TM migration,

and thus simultaneously mitigate voltage decay in the high-voltage region and long-term capacity fading. Related studies have validated this mechanism in O3 layered oxides through density functional theory (DFT) calculations and in situ characterization, demonstrating the feasibility of a general pathway of "increasing oxygen-vacancy formation energy → suppressing O2 release → stabilizing slab gliding and phase boundaries" [49].

Grain-boundary and grain-morphology engineering can further enhance structural toughness at the mesoscopic scale. Single-crystallization and large-grain strategies can substantially reduce the grain-boundary area and the fraction of high-energy grain boundaries, making microcracks more difficult to initiate and propagate along grain boundaries. Pamidi et al. [50] prepared single-crystalline P2–$Na_{0.7}Mn_{0.9}Mg_{0.1}O_2$, among which NMMO-1100 exhibited micrometer-sized, quasi-single-crystalline features with an average primary particle size of approximately 8.1 μm. After 50 cycles within a voltage window of 4.2–1.5 V, the material delivered a capacity retention of 83%; even within a wider voltage window of 4.5–1.5 V, it retained 69% of its capacity after 150 cycles, markedly outperforming NMMO-900 [50]. Xu et al. [51] compared quenching and slow-cooling processes during the solid-state synthesis of O3-$NaNi_{0.4}Mn_{0.4}Co_{0.2}O_2$ and revealed that quenching introduces pronounced synthesis-induced primary lattice strain. During subsequent charge/discharge cycling, this strain spontaneously relaxes, accompanied by the formation and propagation of nanogaps/nanocracks. Thus, crack formation is more likely a consequence of strain relaxation rather than being directly triggered by the layered-to-rock-salt phase transition. Moreover, lowering the cutoff voltage did not significantly alleviate capacity fading; for example, the capacity retention after 100 cycles was only 38.7% under 2.0–3.8 V cycling conditions [51].

Recent studies on La-doped O3-type layered cathodes have further demonstrated that La^{3+} substitution for Na^+ or TM^{n+} sites can strengthen La–O/TM–O bonding, increase the oxygen vacancy formation energy, and enhance lattice-oxygen stability. Meanwhile, La doping reduces the Na^+ diffusion barrier and promotes the reversible O3↔P3 phase transition, thereby substantially improving rate capability and long-term structural integrity. Post-cycling morphological characterization showed that the undoped sample suffered more severe cracking, whereas the La-doped sample exhibited fewer microcracks and better-preserved particle morphology [52]. Overall, surface coatings/passivation layers provide an outer "armor" against air and electrolyte corrosion, whereas anion/cation doping, grain-boundary regulation, and single-crystallization construct a stronger and more robust internal "skeleton". The synergy between these strategies establishes a structural-stability framework required for the practical transition of layered Na_xTMO_2 cathodes from laboratory research to industrial application [53].

Compared with layered oxides, polyanionic compounds, such as $Na_3V_2(PO_4)_3$ and $Na_3V_2(PO_4)_2F_3$, possess three-dimensional frameworks constructed from rigid [XO_4] polyhedra. These structures endow them with excellent thermal stability and limited volume variation, giving them intrinsic advantages in safety and cycling lifespan. Accordingly, polyanionic compounds are regarded as one of the most promising cathode routes for high-safety sodium-ion batteries. Their major limitation, however, lies in their extremely low intrinsic electronic conductivity, typically ~10^{-12} S cm^{-1}, which restricts their performance under thick-electrode and high-rate operating conditions. MXene-confined growth offers a new strategy for improving the conductivity of polyanionic cathodes. For instance, recent studies have fabricated $Na_3V_2(PO_4)_2F_3/Ti_3C_2T_x$ MXene nanocomposites, which significantly enhance electronic conductivity without disrupting the host crystal lattice, increasing the Na^+ diffusion coefficient to ~10^{-9} cm^2 s^{-1} and thereby improving rate performance [54].

On the other hand, nanotechnology engineering has become an important route for improving the electrochemical kinetics of fluorophosphate-based polyanionic cathodes, particularly $Na_3V_2(PO_4)_2F_3$. Strategies such as particle-size reduction, conductive-network construction, surface/interface modification, heteroatom doping, and heterostructure design can shorten Na^+ diffusion pathways, improve electronic conductivity, stabilize electrode/electrolyte interfaces, and enhance high-rate cycling performance [12,55,56]. Recently, ultrafast synthesis routes have also been reported, providing new possibilities for the large-scale application of $Na_3V_2(PO_4)_2F_3$ (NVPF) [57].

In terms of capacity enhancement, activating the high-voltage V^{4+}/V^{5+} redox couple is widely regarded as a key pathway to overcoming the capacity limitation of conventional transition-metal-redox-dominated mechanisms. Taking $Na_3V_2(PO_4)_3$ (NVP) as a representative polyanionic system, numerous studies in recent years have attempted to activate the V^{4+}/V^{5+} redox reaction through hetero-cation doping, such as high-entropy doping, carbon/conductive-network modification, and structural/morphological regulation, thereby improving capacity and energy density [12]. Recent work on trace high-entropy doping with Ca, Mg, Cr, Ti, Mn, and other elements has enabled the reversible participation of the V^{4+}/V^{5+} redox couple during charge/discharge, delivering a capacity of approximately 116 mAh g^{-1} at 1C, which is close to its theoretical value of 117.8 mAh g^{-1} [58]. A recent review further emphasized that although high-voltage V^{4+}/V^{5+} redox holds great potential for increasing theoretical energy density, achieving stable, reversible, and high-capacity output, for example approaching 200 mAh g^{-1}, while

maintaining long cycle life still faces multiple challenges associated with electronic conductivity, structural stability, and electrolyte/interface compatibility [59].

By precisely regulating multiple anionic units, such as $[PO_4]$ and $[P_2O_7]$, the framework rigidity and structural toughness can be enhanced, forming a second major design strategy that complements oxygen-redox-based capacity enhancement while emphasizing high stability. A representative class of studies focuses on $Na_4Fe_3(PO_4)_2(P_2O_7)$ (NFPP), a mixed-polyanion framework. This system contains both isolated $[PO_4]$ units and bridged $[P_2O_7]$ units, in which P–O covalent bonds and multicenter coordination construct a highly rigid three-dimensional framework. The intrinsic volume variation is typically below 3–4%, and continuous Na^+ migration pathways can be maintained even under high-rate operation and deep desodiation conditions [60]. Through heterovalent Mg^{2+} doping and defect engineering, NFPP/C composite cathodes exhibit pronounced pseudocapacitive behavior and ultralong cycling life even at high rates above 10C, with capacity retention remaining above 80% after more than 5000 cycles. This demonstrates that by regulating local polarization and the distribution of metastable Na^+ sites within a rigid framework, capacity and rate capability can be further improved without sacrificing structural stability [61]. From the general perspective of polyanionic cathodes, the inductive effect of $(PO_4)^{3-}$ helps increase the operating voltage, while strong P–O bonds endow the framework with higher structural and thermal stability. At the same time, different anionic groups involve trade-offs between voltage and capacity; for example, pyrophosphates suffer from limited theoretical capacity because of their relatively high molecular weight. Therefore, mixed-polyanion design or further elemental substitution/multicomponent synergy represents an effective approach to simultaneously optimize voltage, capacity, and kinetics [62].

Building on this concept, high-entropy strategies have been introduced into NFPP systems. Partial substitution of Fe sites by multiple transition metals, such as Mn, Mg, Co, Ni, and Cu, increases the configurational entropy and enhances structural stability, allowing the material to undergo a single-phase reaction during Na^+ insertion/extraction while reducing the volume variation to approximately 1.83% (Figure 4a). Benefiting from this low-strain and stable framework, high-entropy NFPP exhibits excellent rate capability and cycling stability even under high-current conditions, retaining a capacity of approximately 55 mAh g^{-1} at 10 A g^{-1} (Figure 4b) [63]. Another strategy focuses on NASICON- and NVPF-type structures, such as $Na_3V_2(PO_4)_2F_3$ and $Na_3V_2(PO_4)_3$, through framework doping and amplified inductive-effect design involving the $[PO_4]$ skeleton and its surrounding anionic environment (Figure 4e). On the one hand, partial substitution of O^{2-} by F^- or construction of a $[PO_4]$–F coordination environment can maintain the rigid PO_4 framework and small volume variation while raising the overall redox potential of V^{3+}/V^{4+} or V^{3+}/V^{5+} by 0.2–0.3 V through a strong inductive effect. On the other hand, introducing secondary metals, such as Mg, Cr, and Mn, at V or Fe sites and coupling this modification with surface carbon coating can further reduce lattice distortion and volume strain during charge/discharge (Figure 4c,f), enabling stable cycling for more than 2000 cycles within a high-voltage window of 2.0–4.3 V (Figure 4d) [64,65]. By optimizing anionic combinations, such as mixed $[PO_4]^{n-}/[P_2O_7]^{4-}/[SiO_4]^{4-}$ units, and local inductive effects, high voltage, high capacity, and high thermal stability can be simultaneously achieved without significantly amplifying volume expansion [66]. Overall, redox-activation-driven capacity enhancement and anionic-framework-reinforcement-driven rigidity/lifetime improvement are becoming complementary strategies in polyanionic cathodes. Together, these approaches establish a practical design framework for polyanionic cathodes with both high energy density and high structural stability [62,67].

Prussian blue analogues (PBAs) occupy an important position among sodium-ion battery cathodes because of their open frameworks, tunable compositions, and low cost, with the active materials themselves potentially costing less than 8 USD kg^{-1}. However, lattice-water-related issues have long hindered their practical application [68–70]. PBAs commonly contain 5–20 wt% crystallization water in their lattices. During charge/discharge and temperature fluctuations, this water can undergo desorption and recoordination, leading to distortion of the Fe–N/C–N framework and local volume changes, thereby inducing crack initiation and interfacial side reactions. Recent studies have shown that the water content of PBAs can be significantly reduced and their framework structures stabilized by optimizing synthesis and post-treatment strategies. For example, low-water-content Fe-PBA has been prepared using a nonaqueous-solvent precursor combined with a water-controlled secondary crystallization system, reducing the interstitial water content to approximately 2 wt%. Meanwhile, lattice defects are decreased and morphology becomes more regular, resulting in markedly improved cycling and rate performance at 1C compared with conventional aqueous coprecipitation samples [71]. Furthermore, mechanochemical synthesis via ball milling has been reported to produce low-water and phase-stable PBAs. Compared with conventional aqueous synthesis, this approach enables more precise control over water content and vacancy concentration, allowing the framework structure to remain stable during cycling [72]. Such strategies have already demonstrated cycling stability over thousands of cycles in several semi-solid-state or commercial modules [68]. At the industrial level, some European

companies have constructed MWh–GWh-scale systems based on crystallization-water-optimized PBA cathodes and demonstrated commercial applications in scenarios such as backup power supplies for data centers.

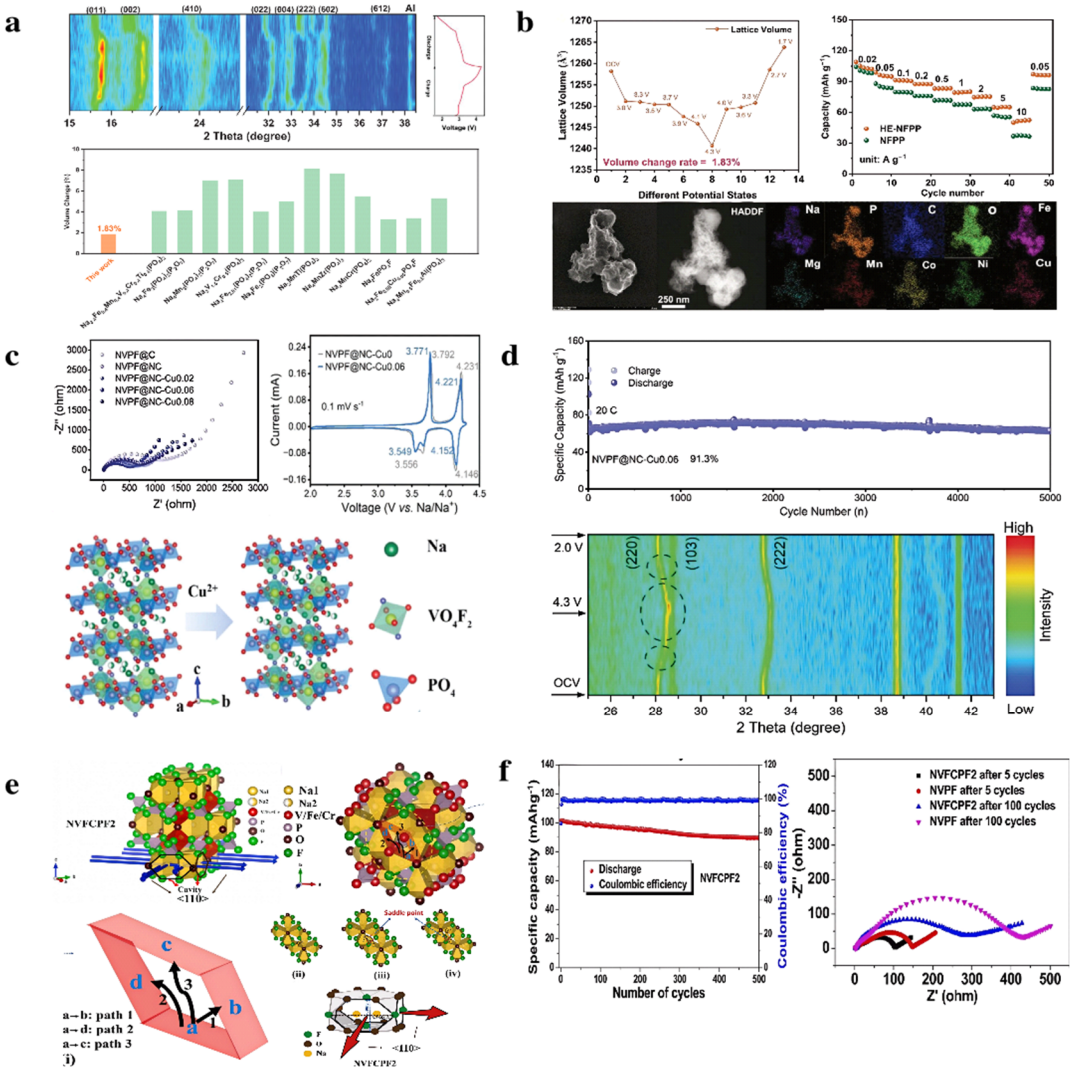


Figure 4. (**a**) Characterization of the single-phase Na^+ insertion/extraction behavior and ultralow volume variation ($\Delta V \approx 1.83\%$) of high-entropy NFPP; (**b**) High-rate/long-cycle performance of high-entropy NFPP and evidence of homogeneous multimetal solid-solution formation revealed by high-angle annular dark-field energy-dispersive X-ray spectroscopy (HAADF-EDS). Reprinted with permission from Ref. [63]. Copyright 2024, Small; (**c**) Enhanced electrochemical kinetics of Cu-substituted NVPF: reduced polarization/impedance and improved reaction reversibility; (**d**) Ultralong cycling stability of Cu-substituted NVPF and in situ XRD evidence of single-phase evolution and structural preservation. Reprinted with permission from Ref. [64]. Copyright 2024, Small; (**e**) Schematic illustration of Na^+ migration channels and key energy-barrier sites in the regulated NVPF framework, involving inductive effects and diffusion pathways; (**f**) Cycling stability and interfacial impedance evolution enabled by coupled doping/coating strategies, including capacity-retention and EIS comparisons. Reprinted with permission from Ref. [65]. Copyright 2024, Journal of Electroanalytical Chemistry.

Recent studies generally agree that the cycling degradation and rate limitations of PBAs are closely associated with $[Fe(CN)_6]$ vacancies, crystallization/coordinated water, and the resulting structural collapse and transition-metal dissolution (Figure 5c). Therefore, strategies such as crystal-structure/defect regulation, morphology and surface modification, and the construction of composite conductive networks or coating layers are commonly employed to enhance their stability and kinetic performance [73,74]. For example, Wang et al. [73] constructed three-dimensional carbon-coated high-entropy PBAs (HE-PBAs@C) and demonstrated that spray drying can reduce the crystallization-water content and improve reaction kinetics (Figure 5a). Meanwhile, carbon coating enhances electronic conductivity and alleviates lattice distortion during cycling, thereby enabling long-cycle stability and high-rate capability (Figure 5b) [73]. In addition, Li et al. [74] prepared Mn-based high-entropy PBA

cathodes via coprecipitation, with the composition of HE-HCF being $Na_{1.20}Mn_{0.38}Fe_{0.15}Ni_{0.14}Co_{0.15}Cu_{0.16}[Fe(CN)_6]_{0.82\square 0.18}\cdot 0.38H_2O$. (where □ denotes a $[Fe(CN)_6]$ vacancy).

High-entropy doping further reduced the crystallization-water content in the structure, and the electrode retained 85.3% of its initial capacity after 1000 cycles at 1 A g^{-1} (Figure 5d) [74]. Another study reported a K-based high-entropy PBA (HEPBA-K) (Figure 5e), with the chemical formula $K_{1.68}Mn_{0.21}Cu_{0.20}Ni_{0.20}Co_{0.19}Fe_{0.20}[Fe(CN)_6]_{0.87\square 0.13}\cdot 0.66H_2O$, which achieved a capacity retention of 78.7% after 3000 cycles at 1 A g^{-1} (Figure 5f) [75]. In another report published in 2025, the crystallization water, vacancies/defects, and interfacial side reactions in PBAs were simultaneously suppressed through heat treatment, crystal-structure optimization, and interfacial protection. This study explicitly highlighted that "bulk and interface" co-regulation represents one of the most effective approaches for improving the electrochemical performance and cycling lifespan of PBAs [76]. Other studies have shown that incorporating alkali-metal ions, such as K^+, can suppress vacancies and crystallization water in PBAs, thereby improving discharge capacity, rate capability, and cycling stability. This provides a feasible direction for developing industrially stable PBA cathodes through doping strategies [77]. Collectively, the latest results lead to a clear conclusion: practical PBA cathode design should strictly follow a combined strategy involving low crystallization-water content, high crystallinity, minimized vacancies/defects, interface/surface engineering, multimetal or high-entropy doping, and scalable synthesis. For stationary energy storage, backup power supplies, and low- to medium-rate energy-storage systems, PBAs are expected to exhibit strong future competitiveness [78].

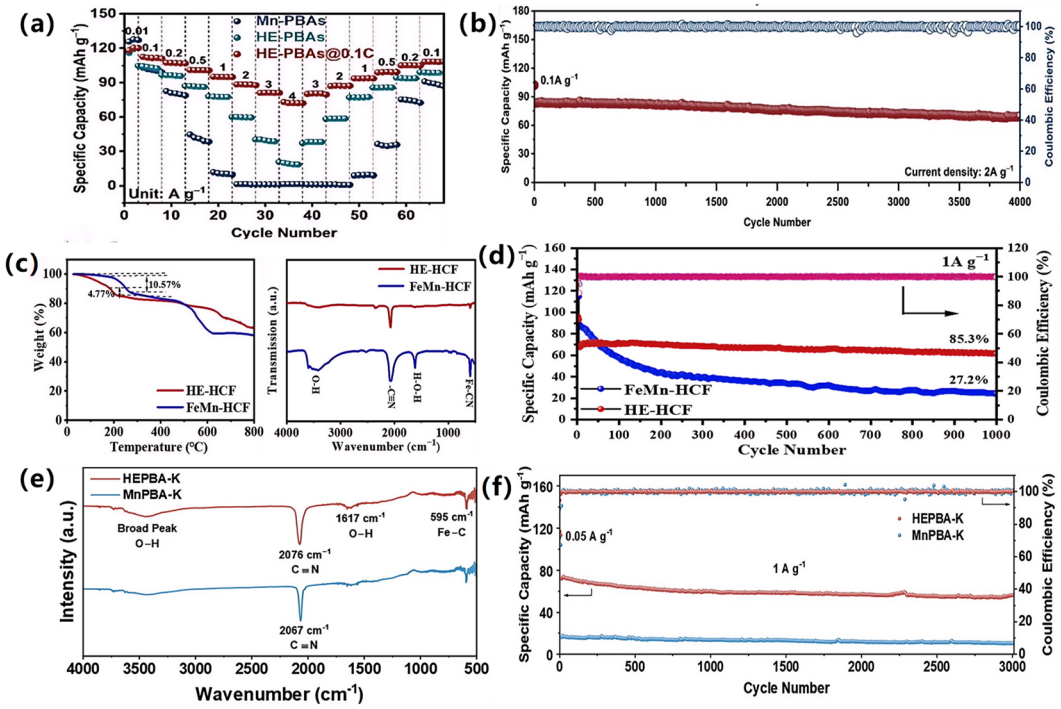


Figure 5. (**a**) Schematic illustration of the enhanced rate capability; (**b**) Long-term cycling performance of HE-PBAs@0.1C at a current density of 2 A g^{-1} after three initial cycles at 0.1 A g^{-1}. Reprinted with permission from Ref. [73]. Copyright 2024, Journal of Materials Chemistry A; (**c**) Thermal analysis and Fourier-transform infrared spectroscopy (FTIR) evidence showing that high-entropy doping reduces coordinated water in PBAs and correlates with vacancy occupation; (**d**) Cycling performance curves of FeMn-HCF and HE-HCF at a current density of 1.0 A g^{-1}. Reprinted with permission from Ref. [74]. Copyright 2025, Batteries; (**e**) Characterization of the particle morphology and coordination environment of K-based high-entropy PBAs. (**f**) Comparison of long-term cycling performance at 1 A g^{-1}. Reprinted with permission from Ref. [75]. Copyright 2025, Chemistry—A European Journal.

A comprehensive comparison of layered oxides, polyanionic cathodes, and PBAs, summarized in Table 1, reveals distinct but complementary advantages. Taking P2-type layered oxides as an example, P2-$Na_{2/3}Mn_{2/3}Ni_{1/3}O_2$ can deliver a specific capacity of approximately 160 mAh g^{-1} within 2.0–4.5 V. In rate-performance comparisons, P2-NaMN still retained approximately 81% of its capacity at 10C (1.84 A g^{-1}), while Nb-doped P2-NaMNNb achieved approximately 98% retention, demonstrating the high-rate potential of layered oxide systems [79]. Polyanionic cathodes combine advantages in safety and cycle life. Accelerating rate calorimetry (ARC) testing showed that NFPP//HC pouch cells did not exhibit a thermal-runaway triggering temperature T2, and the maximum temperature-rise rate was only 0.15 °C s^{-1}. Meanwhile, $Na_3Fe_2(PO_4)P_2O_7$/C

could be stably cycled for 5000 cycles at 10C. PBAs, by contrast, offer both low cost and low-temperature potential. FeVO-PBA has been reported to operate over a wide temperature range of −60 to 80 °C, with almost no capacity decay after 500 cycles at 1C and −30 °C. Its full cell retained approximately 80.1% of its capacity after 500 cycles at 1 A g^{-1}, and the pouch cell could still deliver stable output at −34.3 °C [80–82]. Looking forward, the development of highly stable and practical SIB cathodes is likely to involve the integration of the advantages of layered oxides, polyanionic compounds, and PBAs within multicomponent, multiphase, and multiscale structures. For example, Zou et al. [83] constructed an integrated polyanion–layered oxide cathode, NVFP–VO, consisting of an intergrown biphasic $Na_{3.5}V_{1.5}Fe_{0.5}(PO_4)_3/V_2O_3$ structure embedded in a porous carbon framework. This design enabled both high-rate capability and long cycle life, with the half cell retaining 72.6% of its capacity after more than 100,000 cycles at 100C. In another example, Cai et al. [84] proposed a hybrid-flow machine-learning (HFML) platform to rapidly screen and validate high-entropy layered oxide cathodes from a large candidate space. The identified $Na_{0.95}Li_{0.06}Ni_{0.25}Cu_{0.05}Fe_{0.10}Co_{0.05}Mn_{0.44}Ti_{0.05}O_2$ retained 83.6% of its capacity after 1200 cycles and delivered 110 mAh g^{-1} at 10C.

From a cross-material perspective, the common value of high-entropy and multicomponent design lies in increasing configurational entropy, reconstructing local chemical environments, and enabling multielement synergistic bonding, thereby reducing the driving force for phase transitions and improving defect tolerance. In layered oxides, multisite doping can regulate Na^+/vacancy ordering and TM–O bond strength, suppressing irreversible phase transitions under deep desodiation. In polyanionic systems, high-entropy substitution helps stabilize rigid frameworks and reduce volume strain. In PBAs, multimetal synergy can mitigate the detrimental effects of coordinated water and $[Fe(CN)_6]$ vacancies on framework stability [48,58,63,74,75]. Therefore, high-entropy strategies should not be regarded merely as multielement doping; rather, they should be integrated with phase-structure regulation, interfacial protection, and electrolyte matching to establish a systematic design methodology for long-life and practical sodium-ion batteries.

Table 1. Performance comparison and trend analysis of three types of cathode materials.

Performance/ Characteristic	Layered Oxides (Na_xTMO_2)	Polyanionic Compounds (Polyanion/NASICON, etc.)	PBAs (Prussian Blue Analogues)
Specific capacity (mAh g^{-1})	~160–190 (high-performance Mn/Ni mixed systems: 170–180) [85]	~110–135(e.g., $Na_3V_2(PO_4)_3$ systems) [86,87]	~100–115 (after lattice-water optimization/defect reduction) [88,89]
Rate capability	70–80% capacity retention at 5–10 C [88,90,91]	80–90% capacity retention at 10–20C [8,86,92]	80–85% capacity retention at 5C [88,89]
Environmental/ thermal stability	Prone to phase transformation and structural instability [90,93]	Resistant to ambient exposure and thermal abuse [91,92]	Affected by lattice/coordinated water; stability improves after optimization [62,88,89]
Cycling life	>1000 cycles for optimized samples; most remain <2000 cycles [85,90,91]	>1500–2000 cycles [8,86]	≥1000 cycles; long cycling >2000 cycles still requires further validation [62,88,89]
Raw-material/ manufacturing cost	Mature raw-material supply; stabilization designs increase cost [87,91]	Element-rich compositions and controllable synthesis [91,92]	Raw-material cost <8 USD kg^{-1} [88,89]

Note: The performance values are representative results collected from different material compositions, synthesis routes, and testing protocols. In particular, voltage window, current density/C-rate, electrolyte formulation, temperature, mass loading, and cell configuration vary among the cited studies; therefore, the values should not be interpreted as a strict head-to-head comparison [61,66,68–74]. Thermal-stability data are mainly derived from theoretical estimations or accelerated tests, whereas practical system-level data remain limited [62,63]. The cost values are material-level estimates and exclude manufacturing, cell assembly, and system-integration expenses [64,65].

2.2. Anode Materials: Na-Storage/Interfacial Failure Mechanisms and Structural–Interfacial Stabilization

The interfacial behavior and structural stability of anode materials in sodium-ion batteries directly determine the initial Coulombic efficiency (ICE), cycling lifespan, and low-temperature performance. This section is organized along the progression from industrially viable hard carbon to high-capacity alloy-type anodes and then to highly safe Ti-based intercalation materials. Hard carbon offers balanced advantages in cost and cycling stability and is currently the anode material closest to large-scale commercialization. Alloy-type anodes deliver high capacities but suffer from severe volume expansion, requiring multilevel buffering architectures and self-healing interphases. Ti-based oxides exhibit robust structural stability and high safety, but their capacity and electronic conductivity remain relatively low. These three routes correspond to three core challenges: interfacial side reactions, volumetric strain, and kinetic limitations, respectively. Taking hard carbon as an example, its low-

potential plateau below 0.1 V vs. Na^+/Na is beneficial for increasing the specific energy of full cells, but it also enhances the thermodynamic driving force for electrolyte reduction, resulting in irreversible Na loss during the initial cycle and continuous SEI thickening [7,94,95].

A widely used working model describes Na storage in hard carbon as a three-stage process involving the sloping region, plateau region, and cluster formation. In the relatively high-potential region (>≈0.1 V), Na storage mainly proceeds through adsorption/intercalation associated with defects, edge sites, and disordered interlayers. In the low-potential plateau region (<≈0.1 V), micropore filling and insertion into narrow interlayer spaces become increasingly important. In closed pores below about 1 nm, desolvated Na^+ can further aggregate into highly shielded, quasi-metallic Na clusters that contribute to plateau capacity (Figure 6a,b) [15,96]. Operando ^{23}Na solid-state NMR and complementary in situ/ex situ measurements distinguish more ionic Na environments in the sloping region from more strongly shielded Na environments in the plateau region, supporting an integrated adsorption–intercalation–pore-filling picture (Figure 6c,d) [97].

Nevertheless, the microscopic origin of plateau storage remains under active discussion. Highly shielded ^{23}Na NMR signals are consistent with quasi-metallic Na clusters, but the boundary between confined quasi-metallic species and truly metallic Na is not yet universally defined; likewise, the onset potential of pore filling is not fixed and may overlap with adsorption/interlayer insertion depending on pore size, pore accessibility, electrolyte, and characterization method [97–101]. The three-stage model should therefore be regarded as a system-dependent framework rather than a strictly separated sequence.

Under a simplified approximation, the capacity contribution in the sloping region of hard carbon can be regarded as being dominated by surface capacitive behavior and defect-site adsorption, whereas the plateau region is more closely associated with diffusion-controlled intercalation and pore filling, especially closed-pore filling. cyclic voltammetry (CV) kinetic analysis shows that the b-value in the plateau region is closer to 0.5, while that in the sloping region approaches 1, reflecting their distinct rate-controlling processes. Meanwhile, the irreversible peak at approximately 0.5 V in the initial cycle is related to electrolyte decomposition and SEI formation. The formation of a relatively uniform SEI helps suppress side reactions and polarization, thereby improving the reversibility and cycling stability of low-potential Na storage [102].

Systematic studies have shown that increasing the number of internal closed pores, or closed nanopores, in hard carbon can enhance the low-potential Na-storage contribution and improve overall electrochemical performance. For example, pore-sealing strategies summarized in recent reviews indicate that closed-nanopore-rich hard carbon can deliver a reversible capacity of approximately 299.1 mAh g^{-1}, whereas open-nanopore-rich samples may exhibit capacities as low as approximately 120 mAh g^{-1}, highlighting the critical influence of closed pores and pore-structure regulation on capacity and kinetics (Figure 7a) [103]. Ma et al. [104] introduced oxygen-containing groups through gas-phase pre-oxidation at 300 °C, followed by carbonization at 1400 °C, which suppressed graphitization and promoted the bending of carbon nanosheets to construct closed pores. The resulting CC-1400 exhibited a low specific surface area of 46 m^2 g^{-1} but a higher closed-pore volume of 0.081 cm^3 g^{-1}, enabling the plateau region below 0.1 V to be dominated by closed-pore filling (Figure 7b). As a result, it delivered a reversible capacity of 303.1 mAh g^{-1}, markedly higher than that of the open-pore carbon control sample, 161 mAh g^{-1}. Its Na-storage process can be summarized as a three-step mechanism: surface adsorption, interlayer insertion, and closed-pore filling (Figure 7c) [104]. Wu et al. [105] constructed ultramicroporous hard carbon spheres with pore sizes centered at approximately 0.52 nm through N/P co-doping. The proportion of pyridinic N increased from 26% in NUCS to 49% in NPUCS (Figure 7e). NPUCS achieved a reversible capacity of 257.7 mAh g^{-1} and an ICE of 75% in the initial cycle, both higher than those of NUCS, which delivered 176.3 mAh g^{-1} and 63%, respectively. Moreover, the plateau-region capacity increased from 130.0 to 206.0 mAh g^{-1} (Figure 7d) [105].

Operando and in situ characterization studies suggest that the pore structure of hard carbon must be optimized by balancing two competing requirements: sieving solvated Na^+ to trigger a low-potential plateau and maintaining reversible ion-transport kinetics. Li et al. [98] proposed a "sieving carbon" strategy in which the pore entrance diameter (PED) is controlled below 0.4 nm to sieve solvated Na^+, restrict electrolyte penetration, and suppress intrapore SEI/interfacial electric double layer (IEDL) formation. This design promotes Na clustering within the pores and enables a reversible and extended low-potential plateau below 0.1 V. Stratford et al. [99] combined operando pair distribution function (PDF) with operando ^{23}Na solid-state NMR to identify the formation of metallic Na clusters with diameters of approximately 13–15 Å at low potentials. Meanwhile, operando SANS results support a three-stage sodiation process involving surface adsorption, interlayer insertion, and nanopore insertion/filling (Figure 6e,f) [100].

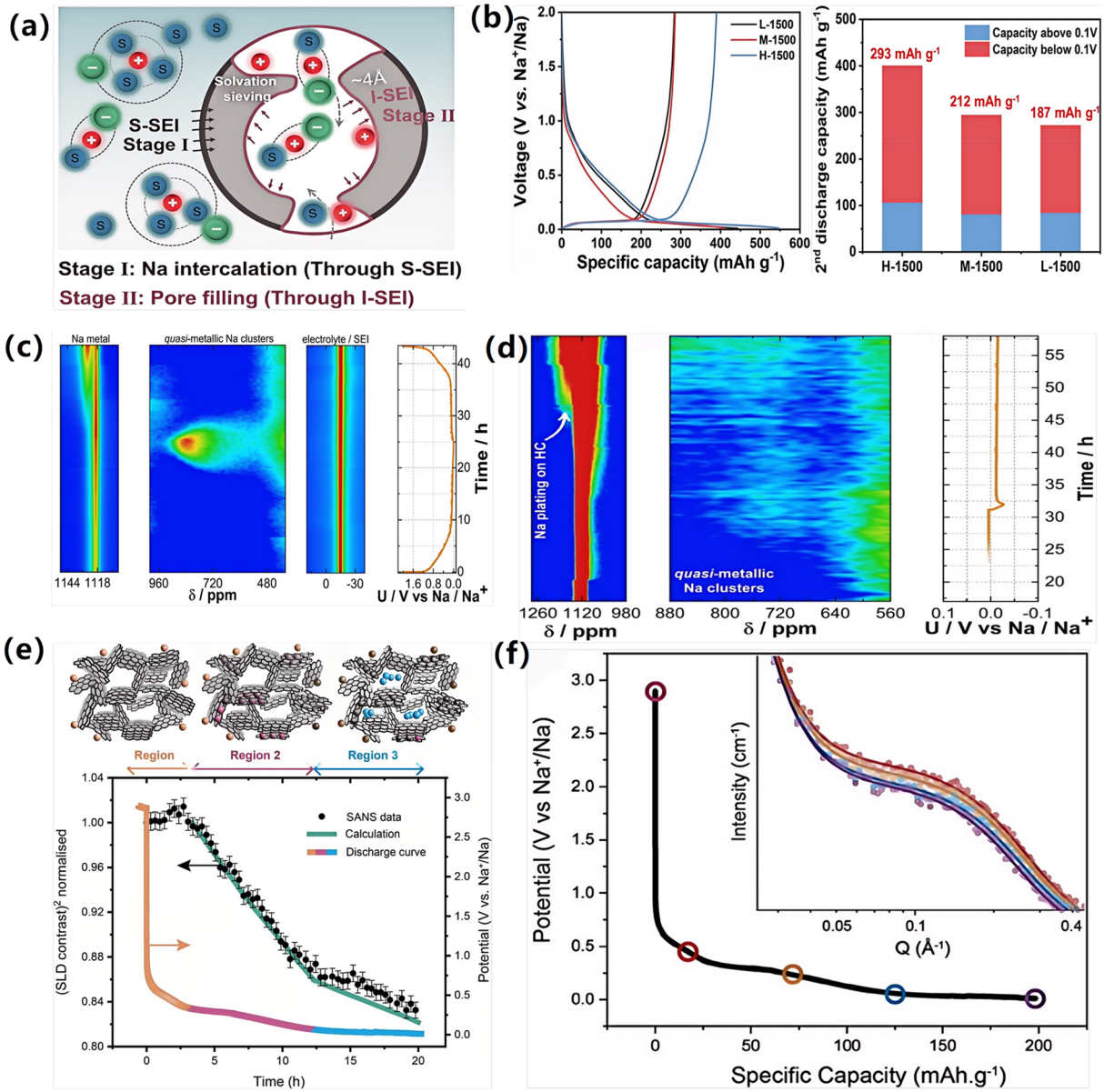


Figure 6. (**a**) Schematic illustration of the pre-desolvation process and dual-SEI formation in hard carbon materials; (**b**) Effect of pore-structure regulation on the capacity contributions from the sloping and plateau regions. Reprinted with permission from Ref. [96]. Copyright 2024, Nature Communications; (**c**) Identification of the chemical environment of quasi-metallic Na clusters in the plateau region by operando ^{23}Na solid-state nuclear magnetic resonance (NMR); (**d**) Operando NMR evidence for the formation and evolution of quasi-metallic Na clusters during the low-potential plateau stage. Reprinted with permission from Ref. [97]. Copyright 2025, Journal of Materials Chemistry A; (**e**) Structural response of hard carbon during the three-stage sodiation process revealed by operando small-angle neutron scattering (SANS); (**f**) Operando SANS scattering features corresponding to distinct Na-storage mechanisms in different potential regions. Reprinted with permission from Ref. [100]. Copyright 2024, Journal of Materials Chemistry A.

Qiu et al. [101] constructed closed-pore-rich hard carbon through one-step pyrolysis of zinc gluconate. During this process, the precipitation and subsequent etching of ZnO nanoparticles first generated open pores of 0.45–4 nm, while some pores shrank and transformed into closed pores at elevated temperatures. In Situ and ex situ evidence demonstrated that the sloping region mainly originates from defect adsorption, whereas the plateau region below 0.1 V is closely associated with the formation of Na clusters inside closed pores, thereby significantly enhancing the low-potential plateau contribution [101]. Overall, rational regulation of the closed-pore fraction and pore-mouth size plays a decisive role in improving plateau capacity, cycling stability, and low-temperature adaptability of hard carbon anodes. However, excessive pore closure or overly narrow pore sizes may restrict ion diffusion and destabilize the interface. Therefore, a precise balance between structural densification and diffusion kinetics must be achieved [106].

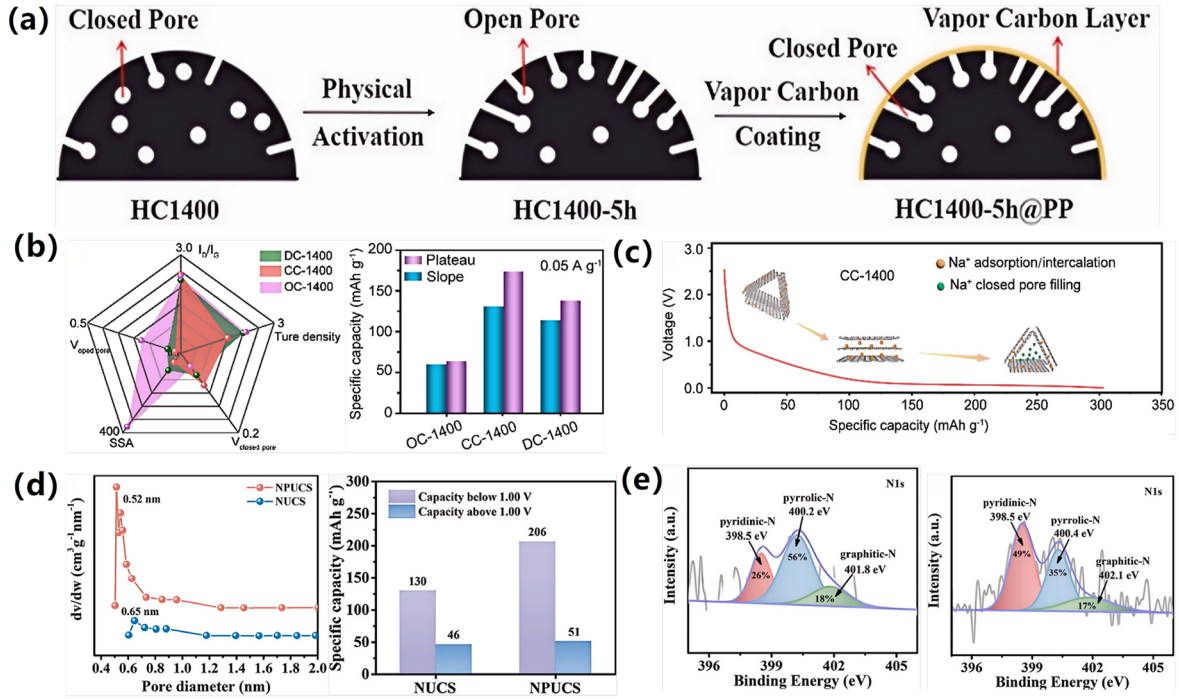


Figure 7. (**a**) Schematic illustration of pore-structure regulation in hard carbon. Reprinted with permission from Ref. [103]. Copyright 2024, Journal of Energy Storage; (**b**) Coupled relationship between closed-pore structural parameters and the capacity contributions from the sloping and plateau regions, as compared among OC-1400, DC-1400, and CC-1400; (**c**) Schematic illustration of the Na-ion storage mechanism in the CC-1400 electrode. Reprinted with permission from Ref. [104]. Copyright 2024, Chemical Engineering Journal; (**d**) Regulation of ultramicropore size and the resulting enhancement of low-potential capacity contribution, comparing NUCS and NPUCS; (**e**) N 1s X-ray photoelectron spectroscopy (XPS) fitting comparison showing the increased proportion of pyridinic N in N/P co-doped hard carbon spheres. Reprinted with permission from Ref. [105]. Copyright 2024, Carbon.

To address the low ICE, continuous SEI thickening, and insufficient reversibility of the low-potential plateau in hard carbon, stabilization strategies should simultaneously target both microstructure and interfacial chemistry. On the one hand, the interlayer spacing, degree of disorder, and pore-size distribution should be regulated through carbonization temperature, precursor selection, and activation methods. On the other hand, the composition, thickness, and mechanical properties of the SEI should be precisely engineered so that it can provide effective passivation without excessively increasing Na^+ transport resistance [107,108].

Recent reviews have suggested that high-performance hard carbon generally possesses several key structural characteristics: a moderately enlarged average interlayer spacing (>0.36 nm), an intermediate density of 1.5–1.8 g cm^{-3}, a high sp^2-carbon content that forms a continuous conductive framework, and a hierarchical pore structure dominated by sub-nanometer closed pores with a small fraction of mesopores providing connectivity (Figure 8a) [109]. The open/closed nature of pores and their electrolyte accessibility further regulate SEI formation and Na-storage behavior, showing a strong correlation with high ICE, high plateau capacity, and relatively small volume variation (Figure 8b) [109]. For example, biomass-derived hard carbons with rationally engineered closed nanopores can be obtained through molecular-level precursor regulation and controlled carbonization. Such closed-pore architectures improve the accessibility and utilization of confined nanopores, thereby enhancing low-potential plateau capacity, reversible capacity, ICE, and cycling stability [110].

Representative biomass-derived hard carbons further demonstrate this structure–performance relationship. Coconut-shell-derived hard carbon achieved 372 mAh g^{-1} and an initial Coulombic efficiency of 91.6% after pore regulation [111]; walnut-shell-derived hard carbon showed an interlayer spacing of 0.397 nm and a low-potential plateau capacity of 195.8 mAh g^{-1}, with corresponding full-cell validation (Figure 8c,d) [112]. Controlled carbonization of waste wood likewise increased closed-pore content while preserving cycling stability (Figure 8e,f) [96]. Pre-oxidation-induced closed ultra-micropores have likewise been shown to raise plateau capacity [113]. Operando small-/wide-angle X-ray scattering (SAXS/WAXS) measurements further indicate reversible pore filling and emptying during the low-potential plateau [114]. Together, these results support biomass-derived precursors as scalable routes while avoiding excessive case-by-case description [115].

To address the problems of thick and loose SEI formation and continuously increasing interfacial impedance in carbonate-based electrolytes, electrolyte-side regulation has become a key strategy for improving ICE and wide-temperature cycling performance [116]. Compared with ether-based electrolytes, conventional ester-type carbonate electrolytes often fail to form a thin and uniform SEI, leading to unsatisfactory cycling and rate performance. Taking $NaPF_6$ in ethylene carbonate (EC): diethyl carbonate (DEC) as an example, the organic/inorganic components in the SEI are more randomly distributed and the film is thicker, possibly accompanied by crystalline phases such as Na_2CO_3 or NaF. These features restrict Na^+ diffusion across the SEI and increase interfacial impedance. In contrast, ether-based solvents are more favorable for constructing a stable passivation layer and forming a thinner SEI. For example, in a DEGDME-based electrolyte, the SEI contains a higher proportion of inorganic components such as NaF and exhibits improved mechanical properties, as confirmed by Young's modulus measurements. high-resolution TEM (HRTEM) and atomic force microscopy (AFM) observations also reveal a thinner interphase, which is more beneficial for Na^+ transport kinetics.

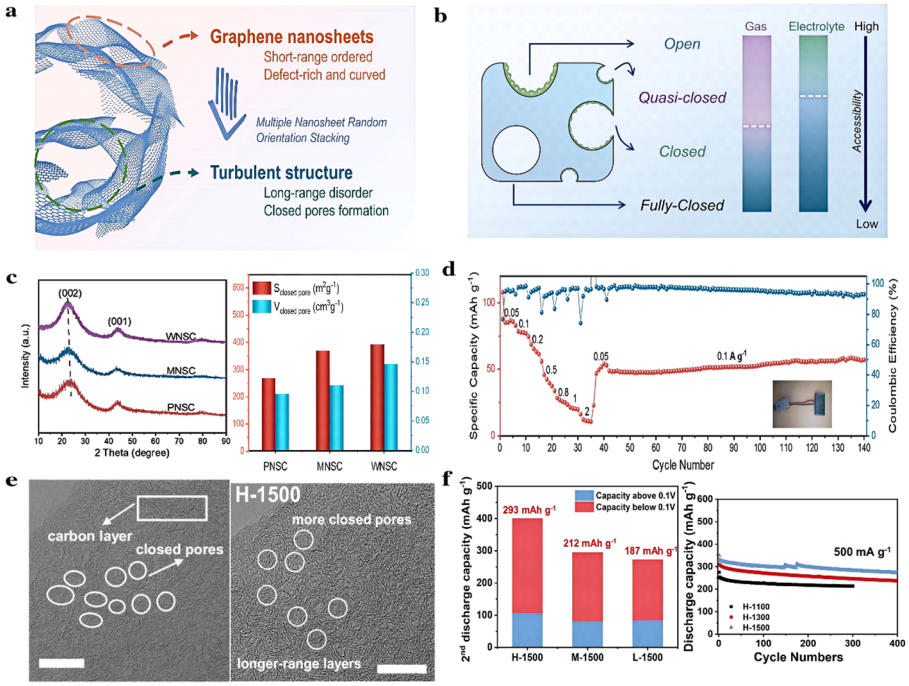


Figure 8. (**a**) Microscopic schematic illustration of graphene nanosheets, highlighted by the pink dashed box, and turbostratic structures, highlighted by the green dashed box, in hard carbon materials; (**b**) Schematic classification of pores based on fluid accessibility. Reprinted with permission from Ref. [109]. Copyright 2025, Nano-Micro Letters; (**c**) Characterization of the interlayer spacing and closed-pore structural parameters of nutshell-derived hard carbon; (**d**) Rate performance and cycling stability of the WNSC//NVP full cell, with an inset schematic showing the illumination of light-emitting diode bulbs. Reprinted with permission from Ref. [112]. Copyright 2025, Carbon; (**e**) Regulation of closed pores and carbon-layer ordering in wood-derived hard carbon by carbonization temperature; (**f**) Enhancement of low-potential plateau capacity by increased closed-pore content while maintaining long-term cycling stability. Reprinted with permission from Ref. [96]. Copyright 2023, Nature Communications.

On this basis, regulating the solvation structure to reduce free solvent molecules, decrease the dissolution of SEI components in the electrolyte, and direct the decomposition pathway toward the formation of less soluble species is also considered an effective strategy for improving interfacial stability. Reviews have indicated that, under typical conditions, electrolyte salts such as NaFSI can be preferentially decomposed to form an inorganic-rich SEI with lower solubility, thereby improving the rate capability and long-term cycling performance of hard carbon [117]. Surface-chemistry characterization further shows that weak-fluorine-bond additives such as MDFA can preferentially participate in interfacial reactions during the initial cycle and induce the formation of a more inorganic-rich SEI containing NaF features (Figure 9a). This enhances interfacial ion transport and mechanical stability. As a result, the ICE of the hard carbon anode increases from 83.2% to 91.6% (Figure 9b), and the pouch cell exhibits markedly superior low-temperature discharge capacity compared with the baseline electrolyte at −20 °C and −40 °C [118].

In addition to constructing the SEI from the electrolyte side, direct modification of the surface chemistry of hard carbon is also an important strategy for enhancing interfacial stability. For example, introducing weak C–F

bond-containing groups such as C–F and –CF_3 allows these groups to preferentially break and reconstruct during the initial cycle, forming a NaF-rich interphase. This can effectively suppress deep decomposition of carbonate solvents and weaken solvent-involved side reactions. Sun et al. [119] grafted fluorine-containing molecules (FB) onto the hard carbon surface to construct an approximately 5 nm NaF-rich thin SEI. time-of-flight secondary ion mass spectrometry (TOF-SIMS), XPS depth profiling, and electrochemical results (Figure 9d) demonstrated that this interfacial design increased the ICE to 90.0% (Figure 9c), reduced interfacial impedance, and improved cycling stability under high-rate conditions [119]. On the other hand, heteroatom doping with elements such as N and P has also been employed to optimize sloping-region capacity and reduce irreversible adsorption sites by modulating the local electronic structure and Na^+ adsorption barriers. Rational doping can improve medium- to high-potential capacity and rate performance without significantly increasing side reactions [120].

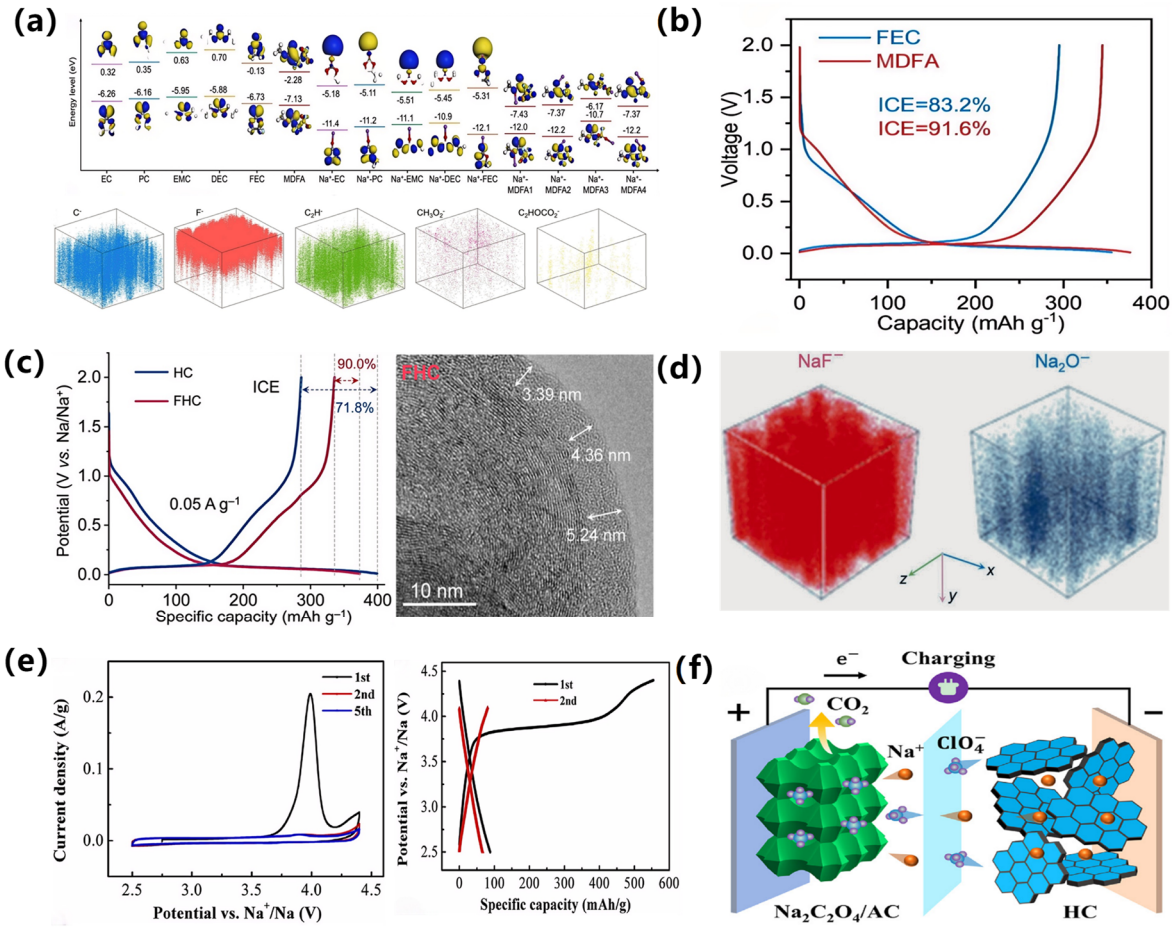


Figure 9. (**a**) Theoretical and statistical evidence showing that MDFA weak-fluorine-bond molecules reconstruct the solvation structure and induce preferential interfacial reactions; (**b**) Initial discharge/charge profiles of the cell. Reprinted with permission from Ref. [118]. Copyright 2025, ACS Nano; (**c**) Electrochemical and HRTEM evidence showing that fluorinated-molecule-grafted hard carbon improves the initial Coulombic efficiency and optimizes the microstructure; (**d**) Distribution of sodium fluoride and sodium oxide contents in the SEI formed on the FHC surface after cycling. Reprinted with permission from Ref. [119]. Copyright 2025, Energy & Environmental Science; (**e**) Electrochemical characteristics of the oxidative decomposition of $Na_2C_2O_4$ sacrificial salt during the initial charge process; (**f**) Schematic illustration of the pre-charging mechanism achieved during the initial charge process. Reprinted with permission from Ref. [121]. Copyright 2022, Journal of Energy Chemistry.

To address the industrial bottleneck of low initial Coulombic efficiency (ICE) in hard carbon, pre-sodiation technologies have been widely proposed and experimentally validated at the laboratory scale [122]. Pre-sodiation can be implemented in several forms, including chemical pre-sodiation, such as using Na–organic sodium salts or $Na_2C_2O_4$ as sacrificial sodium sources, electrochemical pre-sodiation, in which hard carbon electrodes are pre-cycled in an independent electrolyte system, and metallic-Na-contact pre-sodiation. Taking $Na_2C_2O_4$ sacrificial-salt pre-sodiation as an example, Sun et al. [121] first introduced $Na_2C_2O_4$ as a "zero-dead-mass" sacrificial salt into a cathode composite electrode, $Na_2C_2O_4$/activated carbon (AC). During the initial charge process, $Na_2C_2O_4$ undergoes oxidative decomposition at approximately 3.7–4.1 V, with a peak around 4.0 V vs. Na^+/Na (Figure 9e):

$$Na_2C_2O_4 \rightarrow 2CO_2 + 2Na^+ + 2e^-$$

The released Na^+ enters the electrolyte and migrates to the hard carbon anode, thereby realizing pre-sodiation, while the generated CO_2 can be removed by degassing without leaving solid by-products (Figure 9f). This enables efficient sodium compensation and improves the energy density of the device [121]. Although pre-sodiation can effectively compensate for irreversible Na loss during the initial cycle and alleviate the low-ICE issue of hard carbon, its practical manufacturing and application still face several challenges, including process complexity, consistency control, difficulty in large-scale implementation, increased cost, and safety and process-compatibility concerns. Therefore, further improving the intrinsic ICE of hard carbon through material-structure optimization and interfacial design remains a long-term and important objective [123].

Beyond hard carbon, alloy-type anodes, such as Sn, Sb, and P, have attracted considerable attention because of their high theoretical capacities, typically exceeding 600 mAh g^{-1}. However, their severe volume expansion, often above 200–300%, leads to pronounced particle pulverization and rapid cycling degradation. By introducing liquid-metal Ga, which has a melting point of 29.8 °C and self-healing characteristics, and constructing a GaSb@Sn core–shell alloy/carbon composite anode, the sodiation/desodiation stress can be buffered during cycling and the volume effect can be mitigated. Operando electrochemical dilatometry showed that the electrode thickness expansion during sodiation was approximately 33% after stabilization, which is significantly lower than the theoretical expansion of Sn, 420%. The electrode delivered a capacity of approximately 449 mAh g^{-1} at 2 A g^{-1} and retained 82% of its capacity after 2000 cycles [124]. Similarly, Ti-based intercalation-type oxides, such as $Li_4Ti_5O_{12}$, TiO_2, and $Na_2Ti_3O_7$, are considered safer anode systems for sodium-ion batteries because of their small structural variation and excellent cycling stability. Among them, $Na_2Ti_3O_7$ has an average operating potential of approximately 0.3 V and can reversibly accommodate about two Na^+ ions, delivering a capacity of approximately 200 mAh g^{-1} at C/25. However, TiO_2-based materials are still limited by their intrinsically low electronic conductivity and insufficient capacity/energy density, and therefore usually require nanostructuring, coating, or doping to improve rate capability and overall electrochemical performance [125]. Recently, Kojima et al. [126] prepared spinel-type $Na_3LiTi_5O_{12}$ (NTO) through cyclic treatment involving reductive Na insertion into $Li_4Ti_5O_{12}$ followed by Li extraction via water oxidation. The obtained NTO delivered an initial discharge capacity of approximately 158 mAh g^{-1} in Na//NTO half cells, stabilized at approximately 125 mAh g^{-1} after several cycles, and maintained stable cycling for 200 cycles with a capacity retention of 97.6% and a Coulombic efficiency of approximately 99.8% [126].

Overall, practical sodium-ion battery anodes must achieve a balanced optimization among key parameters, including specific capacity, ICE, volume-change ratio, rate capability, and cycling lifespan [127]. Owing to its balanced overall performance, hard carbon remains the preferred anode material for current industrialization. Optimizing closed-pore structures, designing highly ion-conductive SEI layers, and developing safe pre-sodiation processes are the key strategies for further performance breakthroughs. Alloy-type and Ti-based anodes, by contrast, need to continuously evolve toward higher specific energy and improved safety through multilevel structural design and interfacial reinforcement.

A concise comparison of the three major anode routes is provided in Table 2.

Table 2. Representative comparison of major anode-material routes for sodium-ion batteries.

Characteristic	Hard Carbon	Alloy-Type Anodes (Sn/Sb/P)	Ti-Based Intercalation Oxides
Representative capacity	~300–430 mAh g^{-1} for optimized hard carbons [96,98–101,103–115]	>600 mAh g^{-1} theoretical; ~449 mAh g^{-1} demonstrated for GaSb@Sn at 2 A g^{-1} [124]	~125–200 mAh g^{-1} for representative Na/Ti oxides [125,126]
Main failure/stability issue	Low ICE, continuous SEI evolution, pore/electrolyte coupling [94–120]	Large (>200–300%) volume expansion, pulverization, loss of contact [124,125]	Low electronic conductivity and modest capacity/energy density [125,126]
Primary stabilization route	Closed-pore/interlayer regulation, SEI engineering, pre-sodiation [107–123]	Buffering/self-healing architectures and composite design [124]	Nanostructuring, coating, and doping [125,126]
Practical positioning	Closest to current large-scale commercialization [7,127]	High-capacity option but strongly engineering-limited	High-safety/long-life option with lower energy density

Note: Values are representative rather than strictly comparable because electrode loading, voltage window, electrolyte, current density, temperature, and cell configuration differ among the cited studies.

2.3. Electrolytes and Interfaces: Interfacial Failure Mechanisms, Dendrite Suppression, and Interfacial Homeostasis

The solvation structure, decomposition behavior, and the composition and mechanical properties of the solid electrolyte interphase (SEI) and cathode electrolyte interphase (CEI) directly affect the cycling lifespan, safety, and rate capability of sodium-ion batteries. Compared with Li^+, Na^+ generally exhibits lower desolvation energy in various organic solvents. However, in conventional carbonate-based electrolytes, such as 1 mol L^{-1} $NaPF_6$ in EC/DEC, Na^+ still tends to form loose and unstable solvation sheaths, which induce continuous interfacial side reactions, increased polarization, and impedance growth [128,129]. Although sodium metal anodes possess high theoretical capacity, deposited Na is highly chemically reactive. In ester-based electrolyte systems, it readily forms organic-rich SEI layers with insufficient mechanical strength, thereby leading to "dead Na" formation and dendrite risks [130]. Therefore, the core objective of electrolyte and interface design is to construct thin, compact, inorganic-rich, and mechanically robust interphases through solvation-structure regulation, film-forming chemistry control, and solid–solid contact optimization.

Conventional carbonate electrolytes remain the most practical baseline because of their mature processing, cost, and compatibility with existing cell manufacturing. Their optimization therefore relies not only on moving to concentrated electrolytes, but also on solvent/additive synergy. In NFM||HC and sodium dual-carbon cells, combined fluoroethylene carbonate (FEC)/1,3-propane sultone (PS) or cathode–electrolyte additive strategies can construct more robust SEI/CEI layers, suppress transition-metal dissolution and gassing, and improve long-term cycling [131,132]. Film-forming chemistries based on NaDFP or NaDFOB further enrich inorganic NaF/P–O or B/F species and improve interfacial robustness under long-cycle or low-temperature conditions [133–135]. Thus, solvent optimization and dual-additive design remain practical routes for improving NaPF6/EC:DEC-type systems without fundamentally changing the manufacturing platform.

To address the problems of continuous electrolyte decomposition, loose SEI formation, and dendrite growth caused by excessive free solvent molecules, high-concentration electrolytes (HCEs) and localized high-concentration electrolytes (LHCEs) have been developed to reconstruct the primary Na^+ solvation sheath, enabling a transition in interfacial reactions from solvent-dominated to anion-/salt-dominated processes. In these systems, the proportions of contact ion pairs (CIPs) and aggregates (AGGs) increase, allowing anions to preferentially enter the Na^+ coordination environment and decompose on the electrode surface. This induces the formation of stable SEI layers enriched with inorganic components such as NaF, Na_2O, and Na_2S, thereby reducing interfacial impedance and suppressing dendrite growth [136–138].

In liquid electrolyte design, the concept of "salt as a diluent" provides a new strategy for developing low-concentration flame-retardant electrolytes. For example, when $NaNO_3$ is introduced into a low-concentration NaFSI/TMP electrolyte, NO_3^- can competitively replace part of the solvent molecules, forming an AGG-type solvation structure similar to that in high-concentration electrolytes (Figure 10a). This structure further induces the formation of a dense and inorganic-rich SEI on the electrode surface (Figure 10b), thereby balancing safety and interfacial stability [138]. Similarly, in a localized high-concentration NaFSI:DME:MTE system, the AGG-dominated solvation structure enhances interfacial kinetics and promotes the formation of an inorganic SEI enriched with NaF/Na_2S (Figure 10c–f), which contributes to compact and uniform Na deposition morphology [139]. In hard carbon anodes and high-voltage pouch cells, diluent regulation or multianion competitive coordination can also promote preferential anion reduction and construct robust interphases enriched with inorganic elements such as F, P, and B, thereby improving Coulombic efficiency, rate capability, and cycling stability (Figure 10g,h) [140,141]. These results indicate that solvation-structure regulation can alter electrolyte decomposition pathways at the molecular scale, making it an important strategy for achieving interfacial homeostasis and dendrite suppression.

Compared with liquid systems, solid-state electrolytes are expected to fundamentally reduce the risks of electrolyte leakage and flammability, making them an important development direction for all-solid-state sodium batteries. Among them, sulfide solid electrolytes have attracted attention because of their relatively high room-temperature ionic conductivity, reaching 10^{-3}–10^{-2} S cm^{-1}, and certain mechanical ductility [142]. However, they are sensitive to moisture, can release H_2S, and may undergo side reactions at high-voltage cathode or sodium-metal interfaces, leading to chemical/electrochemical instability and thermal safety concerns [143,144]. Heterovalent doping is an effective approach to improving the stability of sulfide electrolytes. For example, introducing W or W/Sn co-doping into Na_3SbS_4 can enhance ionic conduction and interfacial compatibility by generating Na-ion vacancies, stabilizing highly conductive crystalline phases, and suppressing H_2S release (Figure 10i) [145,146]. In addition to sulfides, NASICON-type oxide electrolytes and β-Al_2O_3-type electrolytes generally exhibit good air/thermal stability and wide electrochemical windows. However, their intrinsic ceramic brittleness, sintering difficulty, interfacial point contact, and high interfacial impedance still limit their practical application [136,147,148]. Polymer and composite

solid-state electrolytes offer advantages such as good flexibility, strong processability, and improved interfacial wettability. Their Na^+ transport and electrode contact can be improved by introducing ceramic fillers, plastic-crystal phases, or gel networks, but their room-temperature ionic conductivity, mechanical strength, and long-term chemical stability still require further balancing [149].

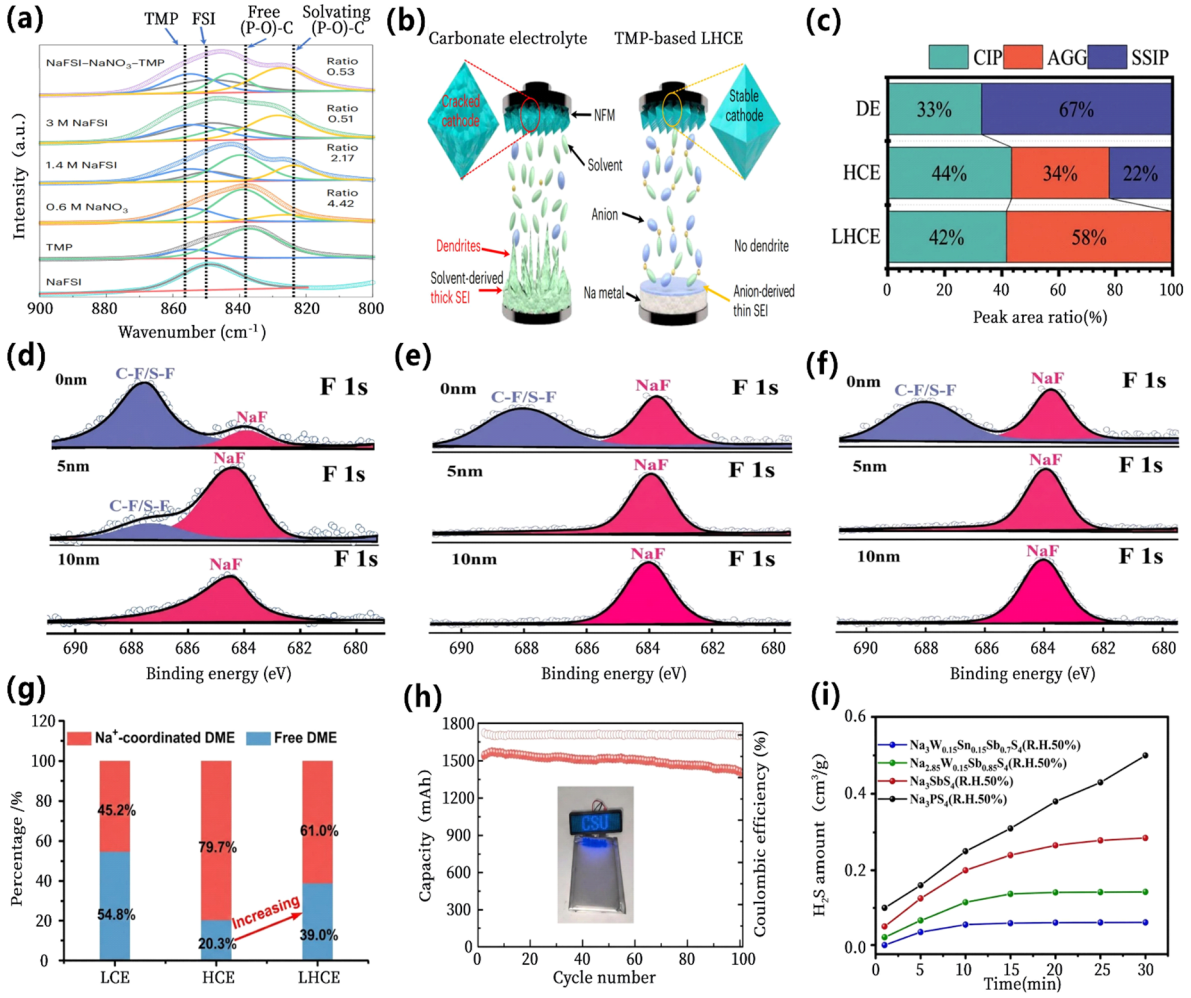


Figure 10. Representative solvation-structure and interphase regulation. (**a**) FTIR spectra and coordination ratios for low-concentration NaFSI/TMP electrolytes regulated with $NaNO_3$; (**b**) corresponding Na-metal cell components after long-term cycling. Reprinted with permission from Ref. [138]. Copyright 2024, Nature Energy; (**c**) Raman-derived proportions of SSIPs, CIPs, and AGGs in NaFSI:DME:MTE electrolyte systems; (**d**–**f**) depth-resolved C 1s and F 1s XPS spectra under Ar+ sputtering showing interphase chemistry. Reprinted with permission from Ref. [139]. Copyright 2025, ACS Energy Letters; (**g**) Raman spectra of FSI^- in three sodium-battery electrolytes. Reprinted with permission from Ref. [140]. Copyright 2025, Energy Materials; (**h**) pouch-cell cycling at 1C within 1.5–4.15 V. Reprinted with permission from Ref. [141]. Copyright 2025, Chemical Engineering Journal; (**i**) H_2S release from sulfide electrolytes in humid air. Reprinted with permission from Ref. [146]. Copyright 2025, Journal of Materials Chemistry C.

To overcome the rigid point-contact interfaces and contact degradation commonly observed between inorganic solid-state electrolytes and electrodes, flexible buffer layers or composite interlayers are required to reduce interfacial impedance and accommodate cycling-induced mechanical mismatch [147]. For example, introducing a PVDF-HFP-based gel polymer buffer layer containing cathode active material (NFM) between a $Na_3Zr_2Si_{2.2}P_{0.8}O_{12}$ (NZSP) ceramic electrolyte and the cathode (Figure 11a) can fill the micropores on the ceramic surface and construct a continuous ion-transport network, leading to a marked reduction in interfacial impedance. Meanwhile, a room-temperature ionic conductivity of 2.19×10^{-3} S cm^{-1} can be achieved (Figure 11b) [148]. In addition, solid plastic-crystal electrolytes (PCEs) based on succinonitrile (SN), FEC, and a $NaClO_4/NaBF_4$ dual-salt system can exploit the high polarity and plasticity of SN to promote sodium-salt dissociation and improve solid–solid interfacial contact. The dual-salt formulation further derives a stable protective layer enriched with F

and B elements at the interface, increasing the ionic conductivity to 3.79 mS cm^{-1} and endowing all-solid-state sodium-ion batteries with improved rate capability and long-term cycling stability (Figure 11c) [149].

These results indicate that the key to solid-state electrolytes lies not only in achieving high bulk ionic conductivity, but also in simultaneously addressing air stability, processing compatibility, and solid–solid interfacial contact. Through doping modification, flexible buffer layers, plastic-crystal/gel interlayers, and composite solid-state electrolyte design, interfacial stress concentration and crack formation can be mitigated to some extent, thereby improving the cycling lifespan and safety of all-solid-state sodium batteries.

For sodium-metal anodes, the synergistic regulation of artificial interphases and electrolyte additives represents an important route to suppressing dendrite growth and parasitic reactions. Room-temperature GaInSn liquid metal can construct a heterogeneous artificial interphase protective layer, denoted as HAIP Na, through self-diffusion and in situ alloying. This interphase improves electrode wettability and sodiophilicity while inducing the formation of a NaF-rich SEI, thereby enabling uniform Na^+ deposition. As a result, Na||SPAN full cells can maintain high capacity after 1000 cycles at 1C (Figure 11d) [150]. In liquid electrolyte systems, the combination of a $Na_2C_2O_4$ cathode additive with FEC can form a uniform inorganic-rich interphase on the anode surface, suppress cation–anion crossover, and improve the cycling stability of sodium-based dual-carbon batteries (Figure 11e) [131]. The combined use of FEC and 1,3-propane sultone (PS) can further construct a composite SEI/CEI film with both high mechanical strength and good flexibility, reducing transition-metal dissolution and cell gassing while improving the long-term cycling performance of NFM||HC pouch cells [132].

Beyond interfacial regulation through artificial interphases and electrolyte additives in liquid systems, the development of solid-state electrolytes represents another key pathway to fundamentally suppress dendrite growth and parasitic reactions. Inorganic oxide solid electrolytes, such as NASICON-type electrolytes, generally possess relatively high room-temperature ionic conductivity; however, their intrinsic brittleness and rigid point-contact interfaces readily induce transgranular fracture and extremely high solid–solid interfacial impedance [151]. To overcome this mechanical limitation, polymer-based and inorganic/organic composite solid-state electrolytes have become important research focuses. For composite systems that are prone to interfacial contact failure during long-term cycling, inspiration can be drawn from advanced flexible materials. For example, a double-network matrix constructed by crosslinking cassava starch with phytic acid has been shown to provide enhanced mechanical robustness [152]. Similarly, a dynamic hydrogen-bonding network formed between tea polyphenols (TP) and polyacrylic acid (PAA) has been demonstrated to markedly improve the structural integrity of silicon anodes; the TP modifier enables the silicon anode to retain an ultrahigh capacity after 300 cycles, with cycling stability far superior to that of the pristine PAA-based system (Figure 11f) [153]. Inspired by these stress-dissipation and self-healing mechanisms, incorporating multiple dynamic bonds into composite solid-state electrolytes may provide an effective strategy to overcome brittle cracking and interfacial delamination. Although interfacial design in solid-state systems shows great potential for mitigating mechanical stress, the overall interfacial stability will face more severe challenges when batteries are deployed in practical applications under harsher operating environments.

Under extreme conditions, such as high temperature, low temperature, and long-term cycling, the thermal stability, ionic conductivity, and regeneration behavior of the interphase become even more critical. The SEI formed in conventional carbonate-based electrolytes often contains a high proportion of organic components, resulting in insufficient thermal stability and mechanical strength. After introducing functional additives such as sodium difluorophosphate (NaDFP), preferential additive decomposition can promote the formation of inorganic components such as NaF and P–O species, constructing an interphase with high ionic conductivity and strong mechanical robustness. This suppresses continuous solvent decomposition and improves the cycling performance of hard carbon anodes (Figure 11g) [133,134]. In addition, sodium difluoro(oxalato)borate (NaDFOB), as a film-forming single main salt, can generate a B- and F-rich inorganic interphase in situ through the reductive decomposition of $DFOB^-$, enabling Na||$Na_3Fe_2(PO_4)P_2O_7$ cells to maintain stable performance under long-term cycling and low-temperature conditions (Figure 11h) [135].

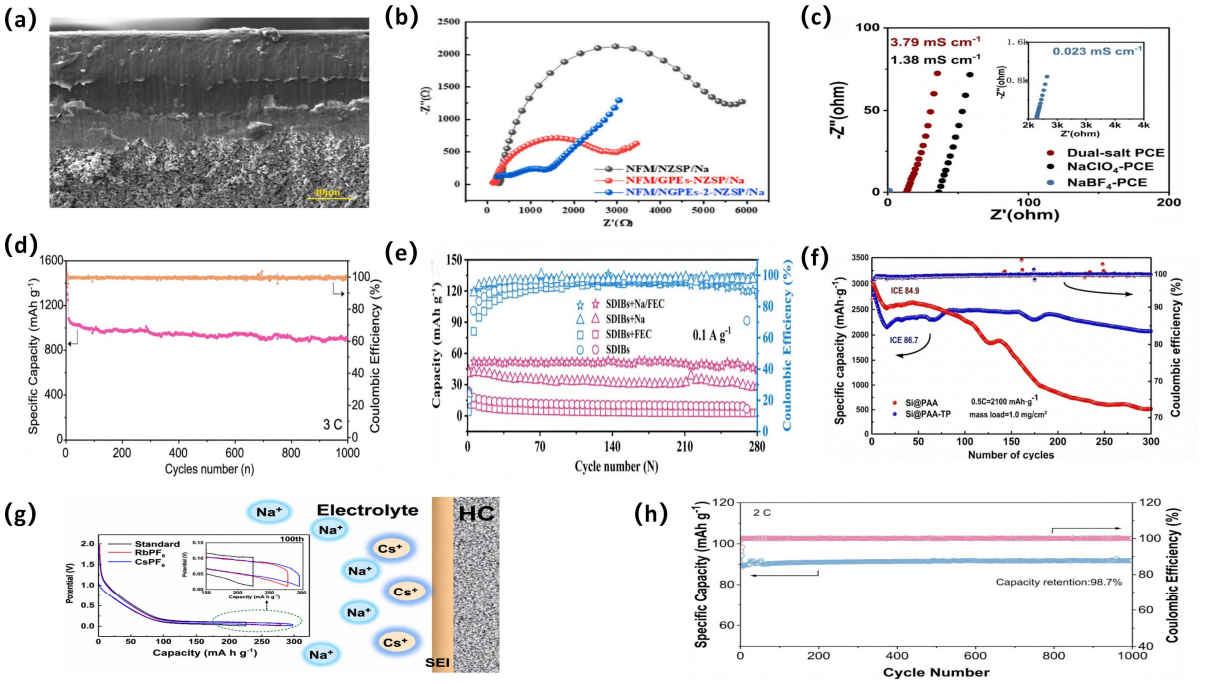


Figure 11. (**a**,**b**) Cross-sectional SEM/EDS characterization of the NFM|PVDF-HFP gel-buffer|NZSP interface (NGPEs-2/NZSP). Reprinted with permission from Ref. [148]. Copyright 2025, Applied Surface Science; (**c**) room-temperature ionic conductivities of the dual-salt plastic-crystal electrolyte (PCE), $NaClO_4$-PCE, and $NaBF_4$-PCE. Reprinted with permission from Ref. [149]. Copyright 2026, Chemical Science; (**d**) Na||SPAN full-cell cycling at 1C with the HAIP-Na artificial interphase. Reprinted with permission from Ref. [150]. Copyright 2025, Interdisciplinary Materials; (**e**) sodium dual-carbon-cell cycling after 280 cycles at 0.1 A g^{-1} using the $Na_2C_2O_4$/FEC interfacial strategy. Reprinted with permission from Ref. [131]. Copyright 2023, Journal of Alloys and Compounds; (**f**) cycling of TP-modified silicon anodes at an areal loading of 1.0 mg cm^{-2}. Reprinted with permission from Ref. [153]. Copyright 2024, ACS Applied Materials & Interfaces; (**g**) proposed working mechanism of the fluorophosphate interphase-forming additive. Reprinted with permission from Ref. [134]. Copyright 2024, Sustainable Polymer & Energy; (**h**) NFPP-electrode cycling at 2C using NaDFOB-based film-forming chemistry. Reprinted with permission from Ref. [135]. Copyright 2024, Advanced Energy Materials.

From the perspective of application scenarios, different electrolyte technologies exhibit clear trade-offs among ionic conductivity, interfacial impedance, cost, and safety. Conventional carbonate-based electrolytes benefit from mature processing technology but generally suffer from insufficient interfacial stability. HCE/LHCE systems and "salt-as-a-diluent" strategies can improve interphase quality and flame-retardant safety by constructing anion-dominated solvation structures. However, further efforts are still needed to reduce diluent cost and optimize viscosity, wettability, and low-temperature transport properties [138,140,154]. Solid-state electrolytes offer considerable potential in terms of safety and high energy density, but the air stability of sulfide systems, interfacial impedance of oxide systems, and room-temperature ionic conductivity of polymer systems remain major barriers to large-scale application [142–149,155]. These application-level trade-offs are summarized in Table 3.

Overall, electrolyte and interface engineering is shifting from the screening of individual additives or solvents toward the synergistic design of solvation structure, interphase formation, solid–solid contact, and processing compatibility. Future studies should integrate in situ/operando characterization, theoretical calculations, and cell-level validation to clarify the failure mechanisms of different electrolyte systems under long-cycle, high-rate, wide-temperature, and high-safety operating conditions. On this basis, stable SEI/CEI layers, flexible buffer interfaces, and processable composite electrolytes should be rationally constructed to support the development of sodium-ion batteries with high energy density, intrinsic safety, and long lifespan. Meanwhile, for large-scale application, electrolyte safety must be considered together with cost control, resource availability, manufacturing consistency, and full-life-cycle sustainability, so as to meet the engineering requirements of both energy-storage and power-battery scenarios [156,157].

Table 3. Representative comparison of electrolyte routes for practical sodium-ion batteries.

Characteristic	Conventional Carbonate Liquid	HCE/LHCE	Solid-State Electrolytes
Representative systems	≈1 M $NaPF_6$ in EC/DEC and additive-modified variants [128,129,131,132]	NaFSI-based HCE/LHCE or anion-dominated formulations [136–141]	Sulfide, NASICON/oxide, polymer, and composite systems [142–149]
Main advantage	Mature processing, lower cost, strong manufacturing compatibility	Anion-rich solvation/interphase chemistry; improved Na deposition and high-voltage stability	Reduced leakage/flammability risk and strong safety potential
Key limitation	Organic-rich/unstable SEI/CEI and continuous side reactions	Higher salt/diluent cost; viscosity, wettability, and low-temperature transport challenges	Sulfide air/H_2S sensitivity; oxide interfacial impedance; polymer conductivity limitations
Practical optimization	Solvent optimization, dual additives, targeted SEI/CEI formation [131–135]	Diluent design, multianion coordination, cost/viscosity reduction [138–141,154]	Doping, flexible buffer layers, plastic-crystal/gel interlayers, composites [145–149]

Note: The table emphasizes qualitative engineering trade-offs. Reported conductivity, cycle life, and safety results depend strongly on salt concentration, solvent/composite formulation, electrode pairing, pressure, temperature, and test protocol.

3. Materials–Electrode–Device Co-Design and Advanced Manufacturing

The performance bottlenecks of sodium-ion batteries are no longer addressed solely through individual material modification, but increasingly through coordinated design across material, electrode, cell/device, and manufacturing levels. Material-scale lattice and interfacial stabilization must be translated through electrode architecture and processing before it can improve cell-level energy density, cycling lifespan, and safety. Accordingly, this section distinguishes material/particle-scale gradient regulation from electrode-scale architecture and then discusses dry processing, thermal management, and interfacial stress control within a materials–electrode–device integration framework.

3.1. Material-Scale Gradient and Electrode-Architecture Design for Coupled Stress and Transport Regulation

Under high areal loading or thick-electrode conditions, ion transport is often limited by tortuous diffusion pathways, leading to concentration gradients and reaction heterogeneity within the electrode. During cycling, such non-uniform reactions can induce local stress concentration, cracking of active particles, and pulverization of secondary particles. Meanwhile, the locally high-overpotential environment near the electrode surface may accelerate SEI thickening, increase interfacial impedance, and reduce active-material utilization (Figure 12a,b) [158]. Therefore, the central objective of electrode-architecture innovation is to simultaneously reduce transport resistance and cycling-induced stress.

At the material/particle scale, composition-gradient design can mitigate local lattice mismatch, phase-transition stress, and interfacial reactivity. In high-voltage P2-type layered sodium cathodes, Ti-rich surface gradients coupled with bulk lattice substitution suppress parasitic reactions and reinforce structural stability during deep desodiation [159,160]. Numerical and post-cycling analyses further show that such material-scale gradients can reduce local stress concentration and irreversible oxygen activity (Figure 12c) [160,161]. By contrast, particle-size or porosity gradients distributed across the electrode-thickness direction belong to the electrode scale; these architectures smooth ion-concentration fluctuations and reaction heterogeneity under high loading (Figure 12d,e) [162,163]. Distinguishing these two length scales avoids grouping particle-composition design and electrode architecture under a single "device-level" category.

At the electrode scale, macroscopic architecture is an important pathway for overcoming transport and mechanical limitations [164]. In multilayer "sandwich" electrodes, a conductive/adhesive bottom layer improves current-collector contact (Figure 12f), a high-loading active middle layer provides capacity, and a conductive-rich or protective top layer compensates for kinetic heterogeneity. Such through-thickness design can reduce internal resistance and polarization while enabling substantially thicker electrodes and higher areal capacity [165,166].

Recently, a study on novel self-supporting electrodes further expanded the performance limits of thick electrodes. In this work, vertically aligned microchannels were constructed within the thick electrode, while a continuous conductive network was woven using carbon nanotube-embedded carbon nanofibers (CNTFs). This architecture not only firmly anchors the active particles, NVPC, through spatial confinement (Figure 12g), but also increases the active-material fraction to 97.5% without using any binder. More importantly, its extremely low pore tortuosity fundamentally opens up the sluggish ion-transport pathways that typically limit conventional electrodes (Figure 12h), ultimately supporting a record-high areal loading of 296 mg cm^{-2} [167]. Overall, multilevel-gradient

and advanced macroscopic electrode architectures provide feasible routes for pushing the energy-density limits of thick electrodes while effectively relieving internal stress and maintaining structural integrity [168].

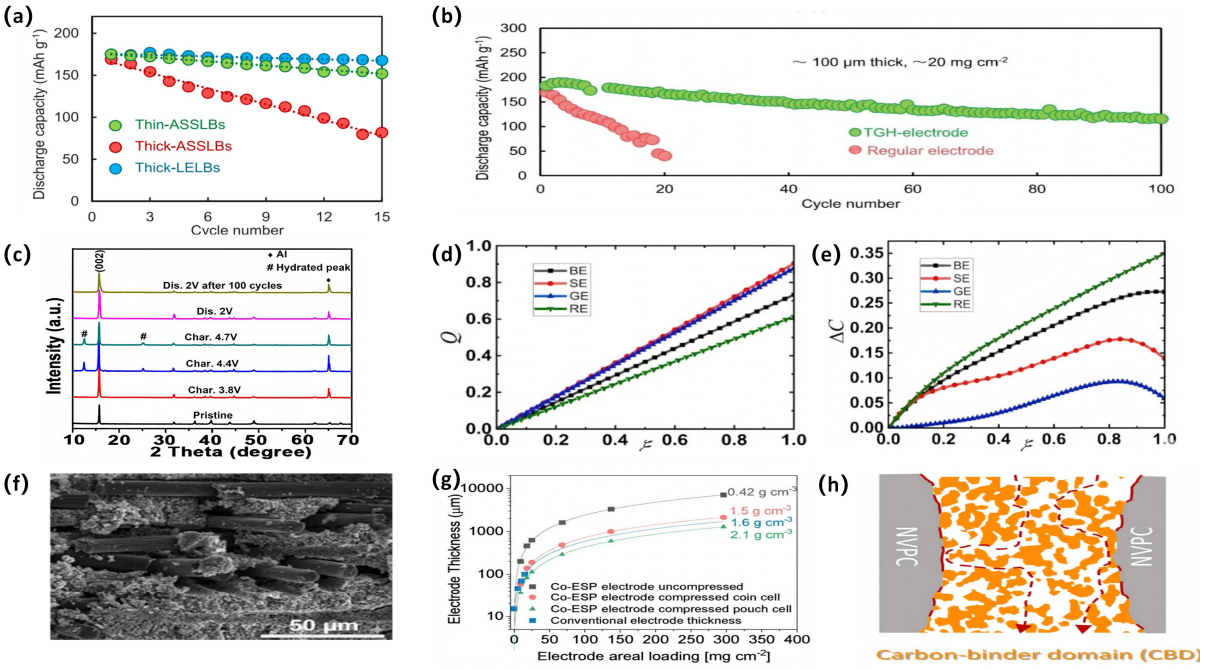


Figure 12. (**a**) Cycling stability of all-solid-state batteries and liquid-electrolyte batteries at 0.1C (**b**) Comparison of cycling performance and specific capacity with reported results in the literature. Reprinted with permission from Ref. [158]. Copyright 2023, National Science Review; (**c**) Characterization of cycled samples at different charge/discharge states. Reprinted with permission from Ref. [160]. Copyright 2021, Chemical Engineering Journal; (**d**,**e**) Relationships among Q, ΔC, and normalized discharge capacity at 1C. Reprinted with permission from Ref. [163]. Copyright 2024, Electrochimica Acta; (**f**) Carbon nanofibers for enhancing electrode stability. Reprinted with permission from Ref. [165]. Copyright 2022, Journal of Power Sources; (**g**) Thickness comparison between the NVPC/CNTF electrode and a conventional electrode; (**h**) Schematic illustration of a conventional electrode with tortuous ion-transport pathways. Reprinted with permission from Ref. [167]. Copyright 2022, Energy & Environmental Science.

3.2. Revolution in Dry Electrode Manufacturing

Conventional electrode fabrication processes rely heavily on organic solvents such as N-methyl-2-pyrrolidone (NMP). In these processes, active materials, binders, and conductive additives are mixed into a slurry, coated onto current collectors, and subsequently dried, resulting in high energy consumption and environmental burdens [168]. In contrast, emerging dry electrode technologies completely eliminate solvents and instead employ fibrillatable binders such as polytetrafluoroethylene (PTFE). Under strong shear forces, active particles and conductive additives are directly mixed into dry powders and pressed into electrode films. This process eliminates the time- and energy-intensive solvent recovery and drying steps required in conventional wet processing, reducing equipment investment and energy-related costs by approximately 15%.

Notably, dry processing endows electrode films with a unique microscopic particle distribution, substantially improving the mechanical stability of thick electrodes. Even in ultrathick electrode configurations, this approach can effectively suppress electrode cracking and significantly reduce interfacial impedance [169,170]. From a microscopic perspective, a three-dimensional fibrous network is formed inside the electrode. Under extrusion and shear mixing, PTFE is stretched into fibers with diameters of only 80–150 nm, which tightly wrap and connect active particles in a “bead-on-string” manner. This structure reduces the interparticle distance to below 500 nm, thereby constructing a continuous and efficient conductive network within the electrode (Figure 13a). Experiments on structurally homogeneous dual-fiber PTFE dry electrodes showed that their volume resistivity was approximately 1.29 Ω cm, only about 70% of that of conventional single-fiber structures, approximately 1.78 Ω cm (Figure 13b). Accordingly, the electronic conductivity of the electrode was estimated to increase by more than 1.4-fold, accompanied by improved cycling performance [171]. In particular, dry processing has been highlighted

as advantageous for all-solid-state batteries (ASSBs), as it can mitigate the binder-covering effect on particle surfaces, thereby preserving more effective ion-conduction pathways and reducing interfacial impedance [172].

Several studies have proposed innovative strategies for process optimization and performance enhancement of dry electrodes. First, compared with conventional wet processing, dry processing effectively suppresses binder migration by eliminating the solvent-drying step. As a result, the compaction density of dry electrode films can reach up to approximately 1.6 times that of conventional wet electrodes, thereby significantly increasing the volumetric energy density of batteries [173]. To further balance the mechanical strength and mass loading of thick electrodes, researchers have constructed a coarse–fine interwoven dual-fiber PTFE structure through stepwise grinding and kneading. This design enables a high areal capacity of 10.1 mAh cm^{-2} while increasing the tensile strength of the electrode film to 1.39 N mm^{-2}, with improved electrical conductivity and reaction uniformity (Figure 13c) [171]. In addition, incorporating 1.0% long carbon fibers (CFs) into the formulation can establish efficient electron-transport pathways throughout the electrode. This increases the electronic conductivity of the electrode film from 35 to 76 mS cm^{-1} (Figure 13d), indirectly confirming that the electron-transport pathways constructed by long CFs reduce internal resistance (Figure 13e), while also enhancing the thermal stability and mechanical framework of the electrode [174]. To address the intrinsic hydrophobicity of PTFE binders, nitrogen-plasma treatment for 2 min can induce C–F bond cleavage and introduce polar functional groups, reducing the water contact angle from 141.9° to 109.5° (Figure 13f). This substantially improves electrolyte wettability without disrupting the bulk structure of the material [175].

For large-scale manufacturing, dry electrode fabrication offers pronounced environmental and cost advantages. Taking solvent-free technologies such as DRYtraec® for sodium-ion battery cathode fabrication as an example (Figure 13g), this process avoids the use of toxic solvents, particularly NMP, from the outset. It not only eliminates the high-energy drying and solvent-recovery steps in conventional manufacturing, but also substantially reduces overall production costs and carbon emissions [176]. The key to this solvent-free process lies in the fibrillation capability of PTFE. Through purely physical operations such as compaction, extrusion, and roll-pressing, PTFE binders can be stretched and interwoven into a network inside the electrode. This mechanism accelerates production while ensuring the physical and electrochemical consistency of thick electrodes [177].

Nevertheless, although dry electrode technology is rapidly advancing from laboratory prototypes toward industrial-scale production, it still faces challenges related to mechanical integrity in practical applications. Studies have indicated that although PTFE fibrillation can provide electrodes with self-supporting capability, binder formulations must be further optimized according to the specific requirements of different battery systems, such as lithium–sulfur batteries and solid-state batteries, to overcome intrinsic limitations such as brittleness or insufficient toughness of electrode films under high mass-loading conditions [178].

A further engineering constraint arises when PTFE-based dry processing is extended to low-potential negative electrodes. Although PTFE provides excellent fibrillation capability and mechanical reinforcement in dry electrodes, its chemical stability under strongly reducing carbon-anode environments should be carefully considered. Possible reductive decomposition or defluorination reactions may consume active alkali inventory and affect binder integrity during long-term cycling. Therefore, practical countermeasures include reducing direct electronic contact between PTFE and deeply sodiated surfaces, minimizing or hybridizing PTFE content where feasible, and designing electrolytes/interphases that improve interfacial passivation. PTFE should therefore not be simply treated as completely electrochemically inert when dry processing is transferred from cathodes to hard-carbon anodes.

3.3. Thermal Management Strategies for Sodium-Ion Batteries

Under high-rate charge/discharge and large-scale energy-storage operating conditions, heat accumulation can accelerate electrolyte decomposition, interfacial side reactions, and electrode structural degradation, while amplifying the risk of thermal runaway. Therefore, thermal management systems must simultaneously consider temperature uniformity, energy consumption, and engineering reliability [179]. For active liquid cooling, bioinspired leaf-vein-like topology-optimized cooling plates can improve coolant-flow uniformity and heat-transfer efficiency through trunk–branch channel architectures. Relevant computational fluid dynamics (CFD) studies have shown that, compared with conventional flow-channel designs, such structures can reduce the maximum cell temperature and significantly decrease the pressure drop, thereby improving module-level temperature consistency and system energy efficiency [180,181].

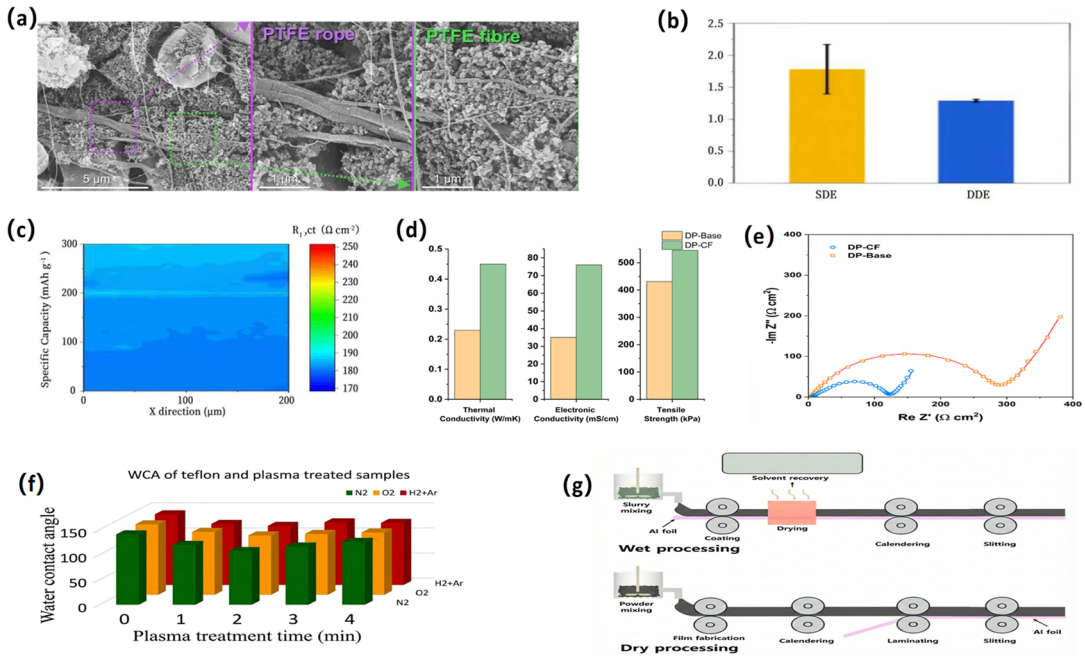


Figure 13. (**a**) SEM images showing PTFE ropes and PTFE fibers in the DDE; (**b**) Volumetric resistivity of SDE and DDE; (**c**) local electrochemical impedance spectroscopy (LEIS) analysis of the DDE. Reprinted with permission from Ref. [171]. Copyright 2025, Energy & Environmental Science; (**d**) Electrochemical performance of DP-Base and DP-CF electrodes; (**e**) Nyquist plots of half cells comparing DP-CF and DP-B electrodes. Reprinted with permission from Ref. [174]. Copyright 2025, Journal of Power Sources; (**f**) Water contact angle (WCA) images of untreated PTFE and plasma-treated PTFE samples. Reprinted with permission from Ref. [175]. Copyright 2023, Polymers; (**g**) Electrode fabrication methods. Reprinted with permission from Ref. [177]. Copyright 2025, Elastomers and Composites.

For passive thermal management, phase change materials (PCMs) can absorb heat through their high latent heat and delay thermal-runaway propagation. To overcome the low thermal conductivity of paraffin-based PCMs, highly thermally conductive fillers such as expanded graphite, graphite foam, and carbon nanotubes can be introduced to construct continuous three-dimensional heat-conduction frameworks. This approach can increase the thermal conductivity from approximately 0.2 W m^{-1} K^{-1} to above 1 W m^{-1} K^{-1}, with some graphite-based composite systems reaching 3.61 W m^{-1} K^{-1} [182–184]. Overall, active liquid cooling is more suitable for rapid heat dissipation in high-rate and high-power modules, whereas passive PCM-based systems offer advantages in suppressing local temperature rise and delaying thermal propagation. Coupled active–passive thermal management designs therefore represent an important direction for improving the safety and lifetime stability of sodium-ion battery modules.

3.4. Adaptive Binding and Interfacial Stress Management

Thick electrodes repeatedly undergo volume contraction and expansion during long-term cycling, which can easily lead to internal stress accumulation, fracture of conductive networks, and degradation of interfacial contact. Therefore, adaptive binder design and interfacial stress management should be considered in coordination with the aforementioned thick-electrode architecture design to maintain the mechanical integrity of electrode films and the uniformity of electrochemical reactions [185].

In terms of conductive-network regulation, constructing a non-uniform gradient distribution of conductive additives along the vertical direction of the electrode can alleviate polarization within thick electrodes and promote balanced charge transport during cycling [185]. For interfacial stabilization, the choice of binder is also decisive. Taking dual-ion batteries as an example, replacing conventional carboxymethyl cellulose (CMC) with a PVDF-HFP binder can substantially suppress parasitic reactions at the cathode–electrolyte interphase (CEI), thereby reducing self-discharge and improving electrochemical stability [186].

To address the severe volume expansion of high-energy-density anodes, room-temperature self-healing microcapsules containing liquid metal have been introduced. The reserved voids inside their conductive carbon shells can directly buffer volumetric strain. When microcracks form in the electrode, the liquid metal flows out under stress and reconnects the conductive pathways, enabling spontaneous healing of electrical contact [187]. In

addition, binders containing dynamic bonds, bioinspired functional groups, or natural biomass-derived components can enhance interparticle adhesion through reversible interactions, relieve local stress concentration during cycling, and repair contact failure, providing new material-design strategies for interfacial stress management in thick electrodes [151,152,188]. In the development of hard carbon anodes for sodium-ion batteries, blending natural biomass-derived sodium lignosulfonate with the LA133 binder can markedly enhance the mechanical adhesion of electrode films while improving charge-transfer kinetics, offering a new strategy for green and sustainable electrode design [189].

Overall, thick-electrode architectures, dry-processing technologies, thermal management, and adaptive binder design collectively reflect a paradigm shift from local material modification toward full-scale co-design across components, devices, and life cycles. Digital twins and physics-based models can further integrate multiscale data for manufacturing-process control, lifetime prediction, and fault warning, while direct regeneration and in situ repair of retired batteries can help reduce the carbon footprint and improve industrial sustainability (Figure 14) [172,190–193].

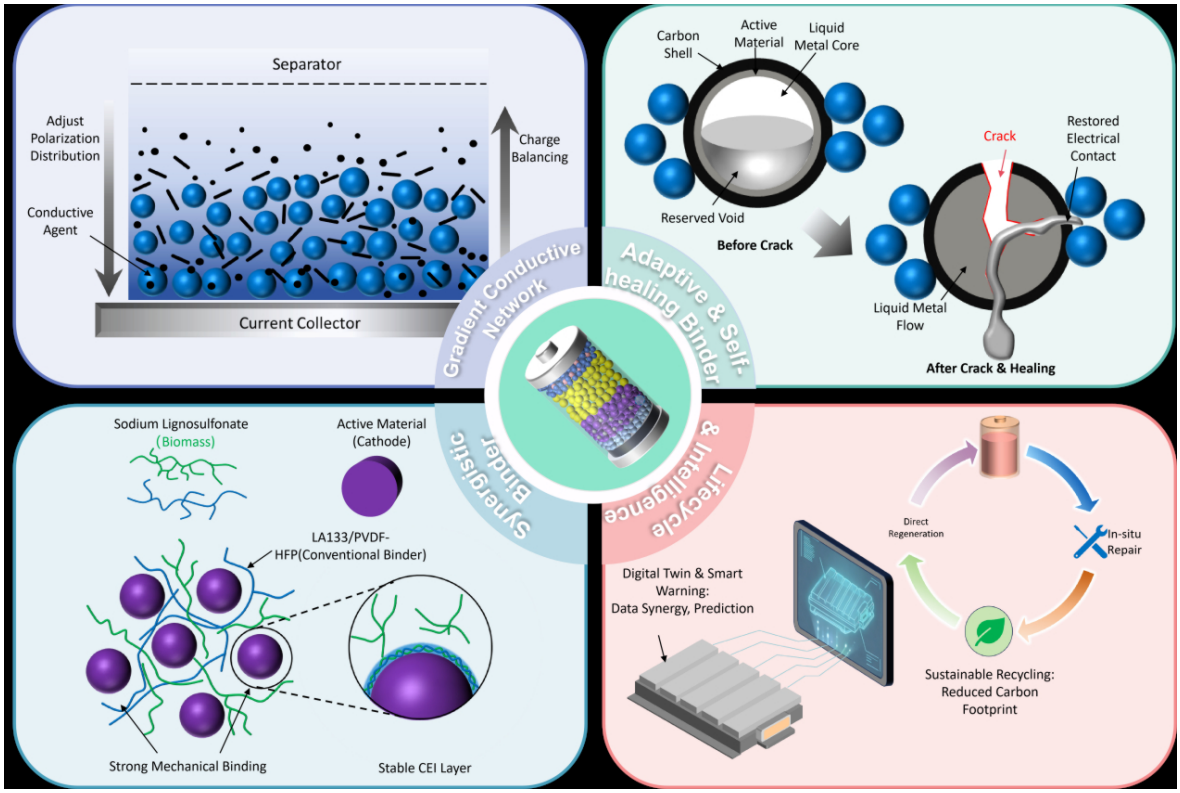


Figure 14. Adaptive binder design and interfacial stress management strategies.

4. Industrialization Pathways and Future Perspectives

Sodium-ion batteries are approaching a critical transition from laboratory validation to large-scale manufacturing. Advances in materials chemistry and process engineering are jointly accelerating their commercialization pathway. Techno-economic analyses further indicate that their competitiveness will depend on coordinated progress in material cost reduction, manufacturing scalability, and supply-chain development. Driven by policy support and industrial-chain advantages, China has become one of the leading regions in GWh-scale production and demonstration deployment [194–196]. Meanwhile, Europe and North America are developing differentiated pathways based on standards and regulations, low-carbon constraints, and specific application scenarios, such as data-center backup power, telecommunication power supplies, and long-life energy storage. Through both institutional design and technological breakthroughs, these regions are enhancing the competitiveness of their domestic industries [129,197]. As an important complement to lithium-ion batteries, sodium-ion batteries, with their combined advantages of low cost, high safety, and wide-temperature operability, are expected not only to reshape the global energy-storage landscape, but also to gradually become a key solution for grid-side energy storage and selected transportation applications.

4.1. Cost Modeling and Technology-Specific Cost-Reduction Strategies

At present, materials generally account for more than 60% of the total cost of sodium-ion battery cells, with cathode materials contributing approximately one-third to one-half and anode materials contributing approximately one-fifth to one-quarter of the total cost (Figure 15a). Therefore, material selection optimization and energy-density improvement have become key pathways for cost reduction [198]. A representative cell-cost model can be expressed as:

$$C_{\text{cell}}=\frac{\sum_i C_{\text{mat},i} M_{\text{act},i}+C_{\text{process}}-\eta_{\text{rec}} C_{\text{rec}}}{\eta_{\text{pack}} E_{\text{grav}} L_{\text{cycle}}}$$

In this model, increasing the recycling efficiency, η_{rec}, and recycling value, C_{rec}, can reduce the full-life-cycle cost while improving resource utilization and system sustainability [199]. The intrinsic cost advantage of SIBs is further supported by the use of Fe/Mn-rich layered oxides, polyanionic compounds, and Prussian blue/white analogues, which reduce dependence on expensive transition metals such as Ni and Co, together with Al-foil current collectors and biomass-derived hard carbon anodes [93]. Industrial tracking and process-modeling analyses further suggest that, under large-scale manufacturing conditions, current-generation SIB cell costs can reach approximately 50–60 USD kWh^{-1} (Figure 15b). With continued expansion of production capacity, improvements in cathode/anode energy density, and higher manufacturing yields, techno-economic analyses indicate that SIBs may progressively approach cost competitiveness with low-cost lithium-ion systems in the 2030s [196,198]. Further cost reduction therefore requires coordinated optimization of cathode materials, anode materials, electrolyte systems, and closed-loop recycling technologies.

For cathode materials, cost reduction relies primarily on the development of low-cost chemistries together with scalable and energy-efficient synthesis routes. Fe/Mn-based layered oxides, NASICON/phosphate-type polyanionic compounds, and Prussian blue/white analogues are attractive candidates because they rely predominantly on earth-abundant elements and reduce or eliminate the use of expensive metals such as Ni and Co (Figure 15c–e). Beyond raw-material selection, elemental doping, phase-structure regulation, and surface/interface stabilization can improve voltage output and cycling durability while retaining the economic advantages of these chemistries [200]. Prussian white materials are particularly attractive for high-rate and long-life applications because of their low-cost solution-precipitation synthesis and open ion-transport frameworks [77,201–203]. In parallel, low-temperature continuous synthesis can reduce process energy consumption and improve production efficiency, further lowering the manufacturing contribution to cathode cost.

For anode materials, hard carbon remains the most practically viable choice for large-scale SIB production because of its relatively low precursor cost, structural tunability, and compatibility with existing manufacturing processes. Renewable biomass resources, including rice husks, coconut shells, and other agricultural residues, provide abundant and potentially low-cost carbon precursors. However, the economic advantage of biomass-derived hard carbon depends on simultaneously controlling precursor purity, carbonization conditions, pore structure, and batch-to-batch reproducibility. Through hierarchical precursor purification, optimization of thermal-treatment windows, and precise regulation of closed pores, improvements in reversible capacity, initial Coulombic efficiency, and production consistency can be achieved. Representative cost targets of approximately 5–10 USD kg^{-1} have been proposed for optimized hard-carbon production, while performance fluctuations have been narrowed to within 10% in representative systems (Figure 15f) [96,204–207]. Such optimization is particularly important because the low-voltage plateau associated with closed-pore Na storage directly influences the achievable energy density of practical full cells.

Electrolyte cost reduction requires a balance among raw-material price, interfacial stability, wide-temperature operation, and manufacturing compatibility. Sodium salts represented by $NaPF_6$ and NaFSI, combined with carbonate- or ether-based solvents, provide practical platforms for simultaneously regulating cost and electrochemical performance. Large-scale production of salts and solvents can reduce unit cost, whereas mixed-salt and additive strategies offer additional opportunities to improve cycling stability and temperature adaptability without substantially increasing formulation complexity [208]. In particular, Na^+/K^+ mixed-salt strategies can enhance ionic conductivity and low-temperature performance, maintaining high capacity at approximately −40 to −50 °C while promoting the formation of more stable SEI/CEI interphases [209–212]. Consequently, electrolyte optimization can contribute to cost reduction not only through lower material expenditure, but also through extended service life and reduced lifecycle replacement demand.

From a lifecycle perspective, closed-loop recycling provides an additional route for reducing both economic and environmental burdens. Al-foil current collectors, residual sodium salts, and partially recoverable electrode materials retain value after battery retirement and can potentially be regenerated for subsequent battery production.

Physical separation and chemical purification therefore provide a means of partially offsetting virgin-material demand and associated procurement costs. More advanced routes combining cryogenic embrittlement, hydrometallurgical leaching, and electrochemical purification can further improve the recovery and regeneration of valuable components and sodium salts, providing an engineering basis for closed-loop material utilization [213–215].

Overall, the cost competitiveness of sodium-ion batteries cannot be achieved through raw-material substitution alone, but requires coordinated improvements in material chemistry, energy density, manufacturing efficiency, electrolyte durability, and end-of-life resource recovery. Such multilevel cost optimization provides the economic foundation for subsequent manufacturing scale-up and industrial deployment.

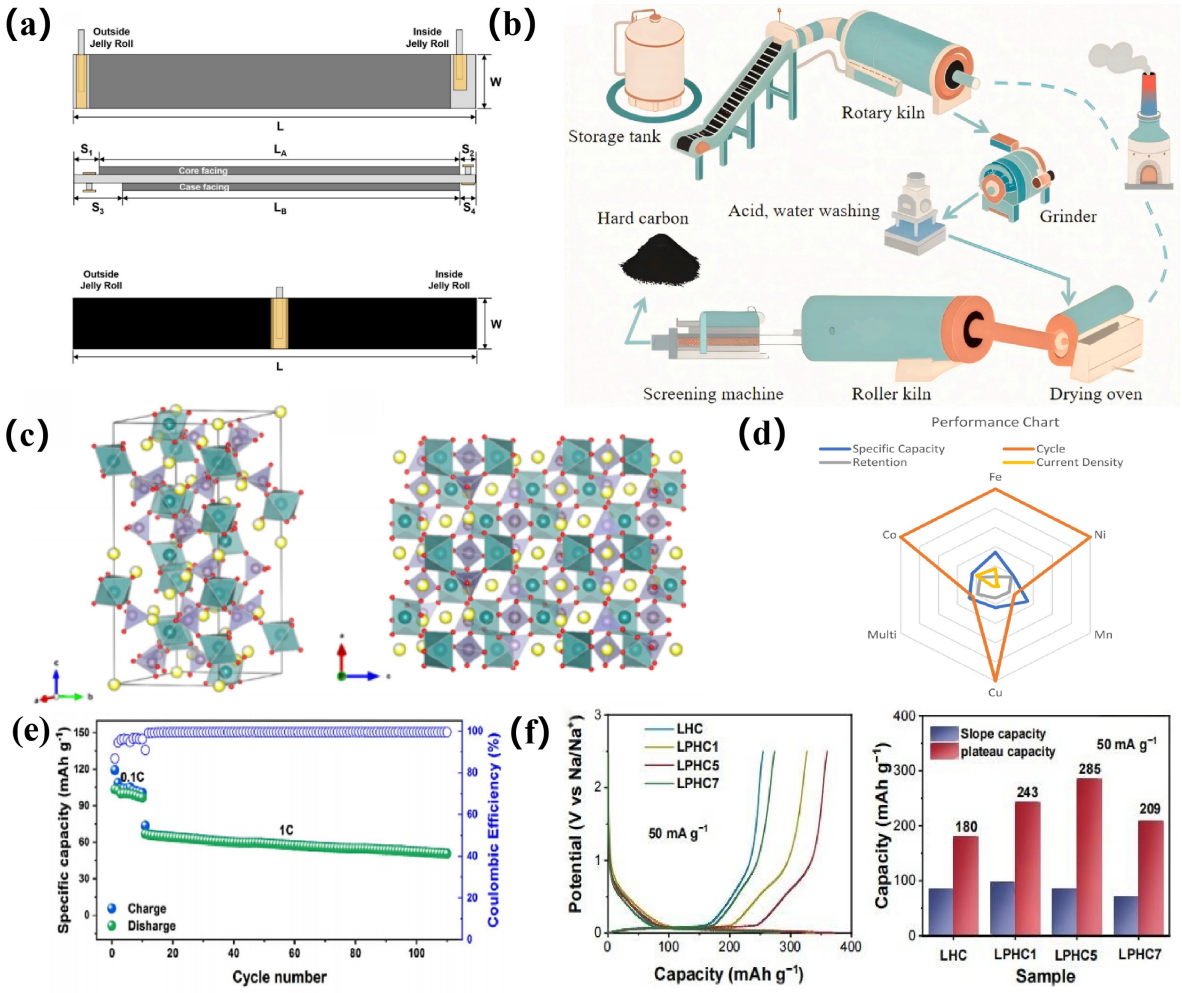


Figure 15. (**a**) Schematic illustration of sodium-ion battery cell design. Reprinted with permission from Ref. [198]. Copyright 2025, Journal of Power Sources; (**b**) Schematic illustration of the industrial production process of hard carbon. Reprinted with permission from Ref. [204]. Copyright 2025, Energy Storage Materials; (**c**) Crystal structure of $Na_3V_2(PO_4)_3$ viewed along different crystallographic directions. The yellow, blue, purple, and red spheres represent Na, V, P, and O, respectively. Reprinted with permission from Ref. [93]. Copyright 2023, ACS Central Science; (**d**) Performance chart comparing five performance metrics of Prussian blue analogues (PBAs) based on different metals, including Fe, Ni, Mn, Cu, multimetallic systems, and Co. Reprinted with permission from Ref. [77]. Copyright 2025, Journal of Energy Storage; (**e**) Cycling stability of the full-cell device at 1C. Reproduced with permission from Ref. [200]. Copyright 2025, Advanced Functional Materials; (**f**) galvanostatic charge–discharge (GCD) profiles of LPHCs at 50 mA g^{-1}, together with the capacity contributions from the sloping region (>0.1 V) and plateau region (<0.1 V) during the second discharge process. Reprinted with permission from Ref. [205]. Copyright 2025, Journal of Power Sources.

4.2. Roadmap for Manufacturing-Process Upgrading

The large-scale manufacturing of sodium-ion batteries increasingly depends on the coordinated advancement of material synthesis, electrode fabrication, process digitalization, and quality-control technologies. Among these routes, continuous solid-state synthesis remains one of the most mature approaches for large-scale cathode production. Processes based on twin-screw extrusion and staged sintering in rotary kilns have already been deployed at scale in China. By combining medium-temperature dehydroxylation with high-temperature

crystallization, such processes enable improved control over phase purity and particle morphology. The annual production capacity of a single line can reach the ten-thousand-ton level, while energy consumption can be maintained below approximately 6000 kWh t^{-1}, supporting the scalable preparation of layered and polyanionic cathode materials.

Beyond conventional solid-state processing, hydrothermal, supercritical, and other solution-based synthesis routes provide alternative pathways for improving reaction kinetics and compositional uniformity. Under supercritical water conditions, typically ≥374 °C and 22.1 MPa, rapid nucleation and crystallization can shorten synthesis time from more than ten hours in conventional processes to approximately 1 h. Such conditions can also promote more uniform particle-size distributions and more precise stoichiometric control, making these routes particularly attractive for highly active layered materials and functional-gradient particles. These technologies are expected to progress toward hundred-ton to thousand-ton pilot-scale validation in the coming years (Figure 16e), thereby complementing established solid-state manufacturing routes [216,217].

At the electrode-manufacturing level, dry-processing technologies are being increasingly explored for sodium-ion battery production because of their potential to reduce solvent-related energy consumption and simplify process flows. Coating speeds of approximately 5 m min^{-1} have been demonstrated, together with progress in the coordinated control of electrode density and pore structure. By eliminating NMP use and reducing drying requirements, dry processing can lower energy consumption while maintaining electrode consistency (Figure 16c). In parallel, the adoption of aqueous binders and in-line monitoring of parameters such as thickness, solid content, and porosity can further reduce process fluctuations and improve manufacturing reproducibility [218].

Digitalization provides an additional route for improving manufacturing efficiency and product consistency. Digital-twin and machine-learning approaches have been introduced into key processes including coating, sintering, and calendering, with representative studies reporting reductions in energy consumption of approximately 15–25% together with improvements in manufacturing yield (Figure 16a). Machine-vision inspection systems based on YOLO-series models and hyperspectral imaging have also been applied to electrode-defect detection (Figure 16b), with reported detection accuracy and recall rates exceeding 99% in representative cases (Figure 16f,g) [219–221]. For automotive-grade applications, increasingly stringent requirements for thermal safety and cell-to-cell consistency, including thermal-runaway triggering-temperature criteria (Figure 16d), are expected to further promote the refinement of process windows, in-line monitoring, and quality-control standards [222].

Overall, the manufacturing upgrade of sodium-ion batteries is evolving from isolated process optimization toward integrated control across material synthesis, electrode fabrication, digital monitoring, and quality assurance. The combination of scalable synthesis routes, solvent-reduced electrode processing, and data-driven process control will be essential for improving production efficiency, reducing energy consumption, and ensuring the consistency required for large-scale industrial deployment.

4.3. Global Capacity Deployment, Lifecycle Management, and Sustainability

The global industrialization of sodium-ion batteries is developing along regionally differentiated pathways, reflecting differences in supply-chain structure, application priorities, and regulatory frameworks. China has developed an increasingly integrated industrial chain covering cathode and anode materials, cell manufacturing, processing equipment, and recycling technologies. Multiple cathode routes, including layered oxides, Prussian blue/white analogues, and polyanionic compounds, are being advanced in parallel, while GWh-scale production lines and demonstration projects are progressively expanding, supported by national deployment plans [223]. Such scale-up is expected to further reduce unit manufacturing cost through improvements in process maturity, capacity utilization, and production yield.

In Europe, the development of sodium-ion batteries is more closely coupled with carbon-footprint regulation, circular-economy requirements, and localized supply-chain considerations [224]. These factors favor chemistries based on earth-abundant elements and application scenarios such as stationary energy storage, where cost, safety, and lifecycle sustainability are particularly important. North American deployment, supported by federal manufacturing programs [225], has meanwhile focused more strongly on high-power and long-life applications, including backup power, data-center support, and uninterruptible power-supply systems. These regional differences indicate that the commercialization of sodium-ion batteries is unlikely to follow a single technological pathway, but will instead depend on the matching of chemistry, manufacturing route, and application requirements.

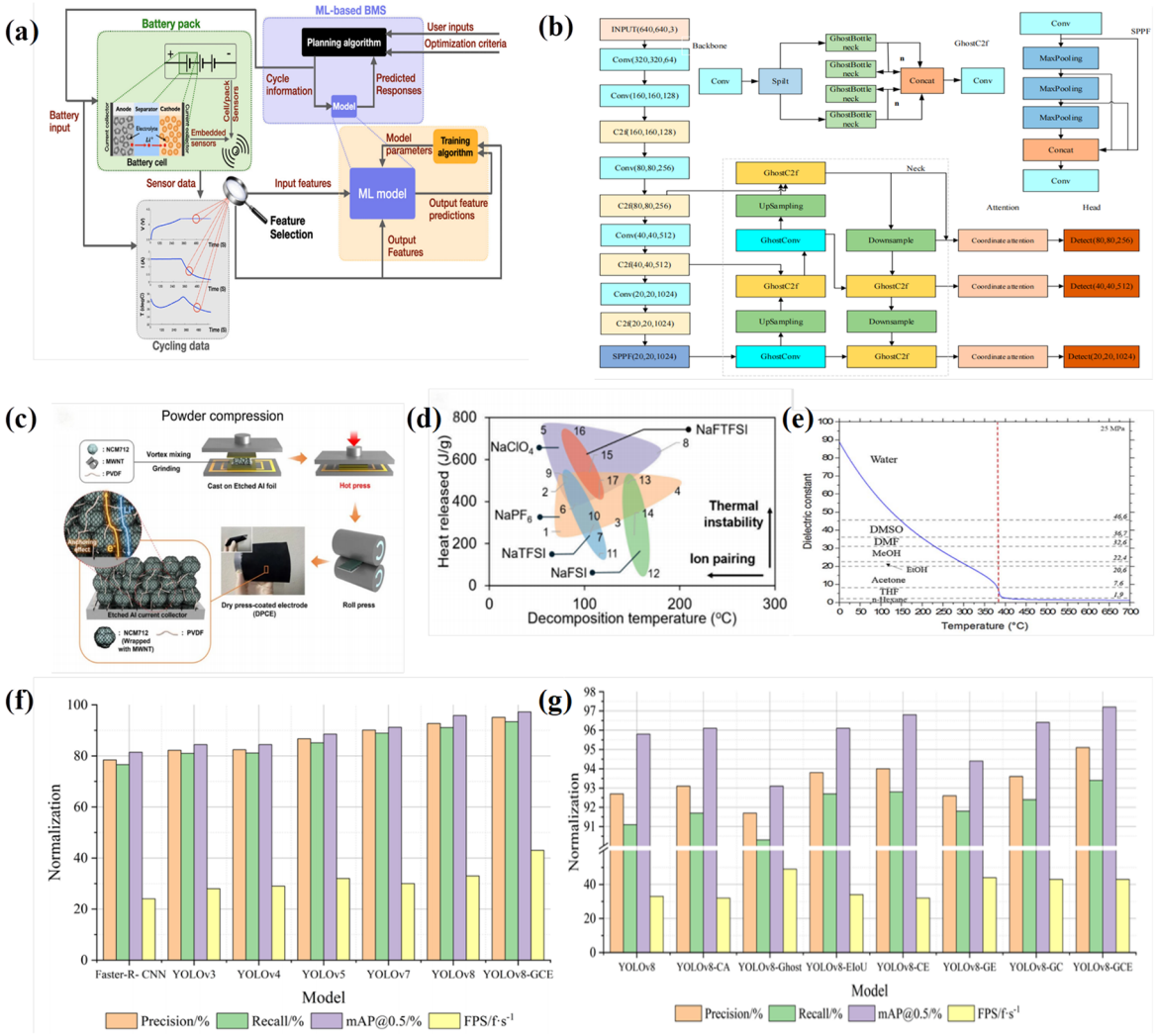


Figure 16. (**a**) Example illustration of machine-learning-based online battery management. Reprinted with permission from Ref. [220]. Copyright 2024, Journal of Power Sources; (**b**) Architecture of the YOLOv8-GCE digital model. Reproduced with permission from Ref. [219]. Copyright 2024, Electronics; (**c**) Typical process for solvent-free dry-coated electrode manufacturing: schematic illustration of powder compaction. Reprinted with permission from Ref. [218]. Copyright 2023, Springer Nature; (**d**) Comparison of the thermal stability of anode interphases formed by various salt–solvent combinations used in sodium-ion batteries. Reprinted with permission from Ref. [222]. Copyright 2025, ACS Energy Letters; (**e**) Temperature-dependent dielectric constant of water at 25 MPa. Reproduced with permission from Ref. [216]. Copyright 2018, Ceramics International; (**f**,**g**) Normalized results of the comparative experiments and overall performance metrics. Reprinted with permission from Ref. [219]. Copyright 2024, Electronics.

Lifecycle management is becoming increasingly important as SIB production scales up. Because many sodium-ion chemistries rely predominantly on Fe, Mn, Na, and carbon rather than high-value metals, recycling strategies differ from those developed for Ni/Co-rich lithium-ion batteries. The economic value of SIB recycling may therefore depend less on maximizing the recovery of precious metals and more on the efficient regeneration of Al foil, sodium salts, electrode materials, and other reusable components while minimizing energy consumption and emissions. Integrated routes combining low-temperature embrittlement for safe disassembly, mild-acid leaching for impurity removal, and electrochemical regeneration of high-purity Na_2CO_3 have been explored for this purpose. Direct-regeneration approaches for layered oxides and Prussian blue/white analogues are also attracting attention because they may bypass complete decomposition and high-temperature resynthesis, thereby reducing process energy demand and carbon emissions [226].

In parallel with material recycling, second-life utilization provides another route for extending battery value before final material recovery. Retired traction or mobility batteries that no longer satisfy demanding power requirements may still retain sufficient capacity for stationary applications, including grid balancing and distributed energy storage. Such cascading utilization can delay final scrappage, improve resource efficiency, and increase the economic return over the full battery lifecycle. Overall, the large-scale sustainability of sodium-ion

batteries will depend on the coordinated development of regional manufacturing capacity, recycling technologies, second-life utilization, and lifecycle-oriented process design. These industrial and sustainability considerations also define the boundary conditions for the next generation of high-energy and highly intelligent sodium-ion battery technologies.

4.4. Technology Outlook and Remaining Challenges

Future sodium-ion battery development is expected to move beyond incremental optimization of conventional cell chemistries toward higher-energy architectures, wider-temperature operation, data-driven materials discovery, and more tightly integrated material–cell–manufacturing design. Among these directions, sodium-metal and anode-free configurations offer a potential route toward substantially higher cell-level energy density by reducing or eliminating inactive anode mass. Recent studies have shown that liquid-metal or alloy-based interphases, as well as multicomponent interfacial layers, can regulate Na nucleation and accommodate interfacial deformation during repeated plating/stripping (Figure 17a). Coulombic efficiencies approaching 99.8–99.9% have been reported in representative systems (Figure 17g), while pouch-cell demonstrations with energy densities above 200 Wh kg^{-1} have also been reported under low-temperature conditions (Figure 17b) [227–230]. Nevertheless, the transition toward substantially higher energy densities will require not only highly reversible Na deposition, but also suppression of dendrite formation, reduction of excess electrolyte and inactive components, and long-term interfacial stability under practical areal capacities and stack pressures.

Wide-temperature operation represents another important frontier. Multication and mixed-salt electrolyte strategies can regulate the primary solvation structure and interfacial decomposition pathways through the coexistence of Na^+ and auxiliary cations such as K^+ (Figure 17c). Such regulation can improve ionic transport and low-temperature reversibility, with representative systems showing markedly improved capacity retention at temperatures as low as approximately −50 °C (Figure 17e) [209–212]. At the same time, these formulations can promote the formation of inorganic-rich SEI/CEI layers containing species such as NaF, thereby improving interfacial stability. However, their practical value will ultimately depend on balancing wide-temperature performance with salt cost, viscosity, compatibility with high-voltage cathodes, and manufacturing requirements.

Artificial intelligence (AI) and data-driven materials design provide a complementary route for accelerating the identification of viable material and electrolyte combinations. AI-assisted electrolyte discovery has already demonstrated the potential of combining high-throughput computation, property prediction, and experimental validation, although many mature examples remain concentrated in lithium-ion systems [231]. For sodium-ion batteries, machine-learning and graph-based deep-learning models are increasingly being applied to cathode screening, composition optimization, and the prediction of multicomponent or high-entropy material properties (Figure 17d,f) [232]. Recent SIB-focused studies and reviews further emphasize the value of integrating data-driven prediction with physical descriptors and experimental feedback to establish closed-loop workflows for cathode, anode, and electrolyte development [233]. The major challenge is therefore shifting from model accuracy alone toward physically interpretable, experimentally validated, and manufacturing-relevant predictions.

Despite these advances, increasing the practical energy density of SIBs remains a fundamental challenge. Moving beyond the present 160–200 Wh kg^{-1} range toward substantially higher values will require coordinated development of high-voltage cathodes, sodium-metal or anode-free architectures, and electrolytes capable of maintaining stable interphases at elevated operating potentials. In particular, electrolyte oxidation, lattice-oxygen instability, transition-metal dissolution, and Na-metal interfacial instability become increasingly severe as the energy density is pushed upward. Addressing these coupled limitations will require integrated salt/solvent design, functional additives, surface/interface stabilization, and cell-level engineering rather than optimization of a single material component.

Long-term lifetime and manufacturing consistency constitute an equally important barrier. Defects and residual water in Prussian blue/white materials, phase transitions and microcrack evolution in layered oxides, and the structural controllability of closed pores in hard carbon remain sensitive to both synthesis history and processing conditions. Achieving thousands of deep cycles and calendar lifetimes extending beyond ten years will therefore require tighter coupling between material design, interphase regulation, electrode fabrication, and manufacturing-process control [222]. Particular attention should be paid to batch-to-batch reproducibility because excellent laboratory-scale electrochemical performance does not necessarily translate directly into stable large-scale production.

Resource availability and supply-chain resilience will also influence the long-term competitiveness of SIB technologies. Reducing reliance on Ni and Co strengthens the resource advantage of Fe/Mn-based layered oxides, polyanionic compounds, and Prussian blue/white cathodes. However, the supply chain of hard-carbon precursors

introduces a different challenge because biomass-derived feedstocks can vary substantially in composition, impurity content, and regional availability. Establishing diversified precursor sources together with standardized purification and pretreatment protocols will therefore be important for maintaining consistent material quality and controlling production cost.

At the manufacturing level, further scale-up from GWh toward TWh production will place increasingly stringent requirements on process yield, quality control, and digital integration. Even small reductions in first-pass yield can translate into substantial material and energy losses at large production scales. Digital twins, machine-vision inspection, physics-informed process models, and in-line sensing therefore provide important tools for narrowing process windows and identifying defects before they propagate through subsequent manufacturing steps. However, intelligent manufacturing should be developed together with sodium-specific process knowledge, because electrode chemistry, moisture sensitivity, slurry or dry-processing behavior, and thermal-management requirements may differ substantially from those of established lithium-ion production systems.

Overall, future progress in sodium-ion batteries will depend on the convergence of high-energy cell chemistry, stable interfaces, wide-temperature electrolytes, data-driven materials discovery, scalable manufacturing, and lifecycle sustainability. The central challenge is no longer to maximize an isolated material metric, but to establish quantitatively coupled relationships among material structure, interfacial chemistry, electrode architecture, manufacturing parameters, and long-term cell degradation. Such integration will ultimately determine whether sodium-ion batteries can evolve from cost-competitive alternatives for stationary storage into a broader class of practical energy-storage technologies.

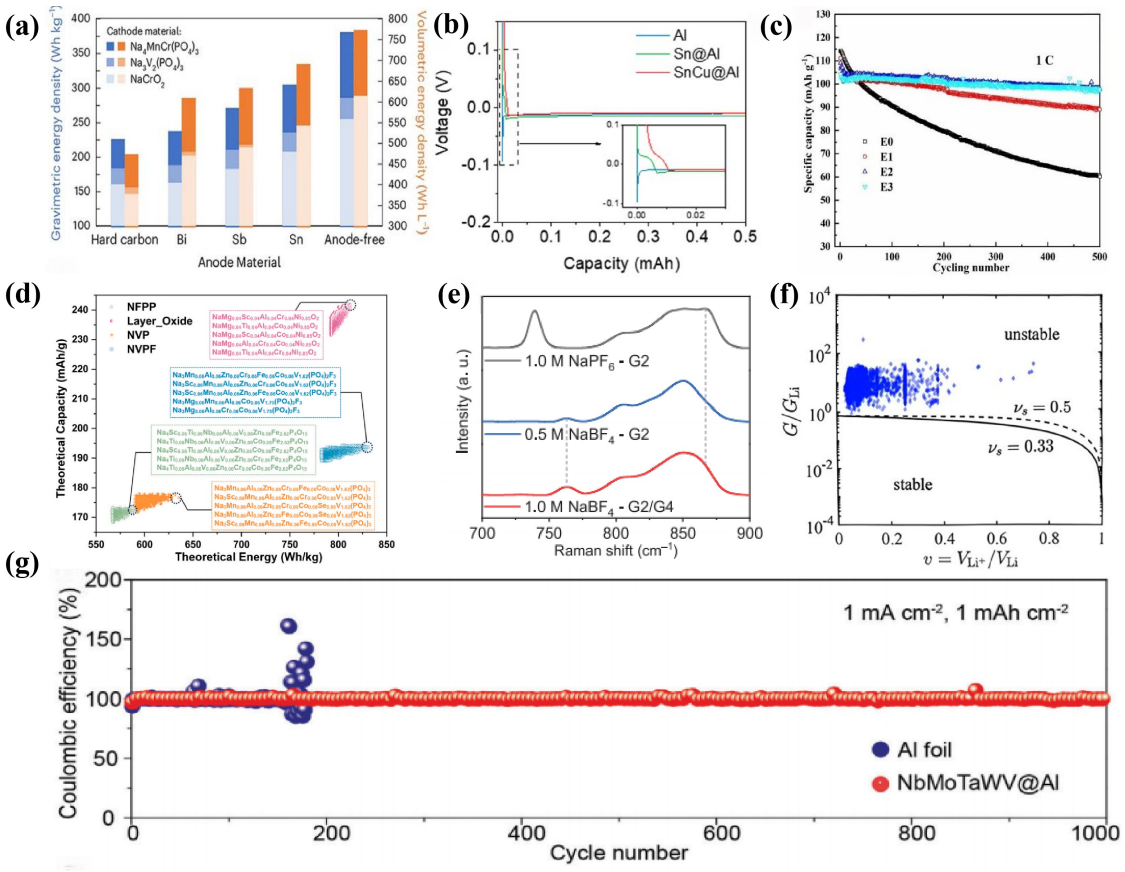


Figure 17. (**a**) Comparison of the theoretical energy densities of different sodium anode materials. Reprinted with permission from Ref. [227]. Copyright 2025, Energy & Environmental Science; (**b**) Nucleation overpotentials for Na plating on different substrates at 0.2 mA cm^{-2}. Reprinted with permission from Ref. [230]. Copyright 2025, Nano Letters; (**c**) Cycling performance of NaMnHCF in different electrolytes. Reprinted with permission from Ref. [210]. Copyright 2024, Nano Energy; (**d**) Relationship between theoretical capacity (mAh g^{-1}) and theoretical energy density (Wh kg^{-1}) for four high-entropy cathode materials. Reprinted with permission from Ref. [232]. Copyright 2024, Journal of Energy Storage; (**e**) Raman spectra of 1.0 M $NaPF_6$-G2, 0.5 M $NaBF_4$-G2, and 1.0 M $NaBF_4$-G2/G4 electrolytes. Reprinted with permission from Ref. [212]. Copyright 2024, National Science Review; (**f**) Isotropic stability map. Reproduced with permission from Ref. [231]. Copyright 2025, Crystals; (**g**) Coulombic efficiencies of Na plating on NbMoTaWV@Al and Al foil at 1 mAh cm^{-2} and 1 mA cm^{-2}. Reprinted with permission from Ref. [229]. Copyright 2024, Advanced Materials.

5. Conclusions

Sodium-ion batteries have progressed from materials-oriented exploration toward integrated optimization across materials, interfaces, electrode architectures, cell engineering, and manufacturing processes. The practical realization of highly stable SIBs requires coordinated advances in several key aspects. For cathode materials, the central challenge lies in reconciling high capacity and high-voltage operation with phase stability, air/moisture tolerance, and suppressed interfacial degradation. For anode materials, particularly hard carbon, improving initial Coulombic efficiency, low-potential plateau capacity, and SEI robustness remains essential for enhancing full-cell energy density and cycling durability. Electrolyte and interphase engineering further determine wide-temperature operation, dendrite suppression, and long-term safety, requiring precise regulation of solvation structures, decomposition pathways, and SEI/CEI chemistry. Across the electrode, cell-engineering, and manufacturing levels, thick-electrode architectures, dry electrode manufacturing, thermal management strategies, adaptive binder systems, and digitalized process control provide critical routes for translating intrinsic material advantages into practical cell performance. Nevertheless, several fundamental issues remain unresolved, including the dynamic formation, dissolution, reconstruction, and mechanical failure of SEI/CEI under realistic cell pressure, temperature, and rate conditions; the long-term structural evolution and scalable reproducibility of high-entropy, multiphase, and composite-interface materials; and the coupled electrochemical–mechanical failure mechanisms at solid–solid interfaces in solid-state and thick-electrode systems. Future progress will depend on the close integration of operando characterization, multiscale modeling, machine learning, electrochemical engineering, and manufacturing science to establish quantitative relationships among material structure, interfacial chemistry, processing parameters, and cell-level degradation. With continued advances in low-cost chemistries, scalable manufacturing, safety management, and closed-loop recycling, sodium-ion batteries are expected to become a technically and economically competitive solution for large-scale energy storage, selected transportation applications, and future low-carbon energy systems.

Author Contributions

Y.L.: Conceptualization, methodology, software; Y.Z.: Data curation, writing—original draft preparation; J.W.: Visualization, investigation; G.N.: Supervision; H.Z.: Software, validation; H.S., W.Z.: Writing—reviewing and editing. All authors have read and agreed to the published version of the manuscript.

Funding

This work was sponsored by the National Natural Science Foundation of China (No. 51802276), Natural Science Foundation of Jiangsu Province (BK20241972), Yancheng City Science and Technology Plan (International Science and Technology Cooperation/Hong Kong, Macau, and Taiwan Science and Technology Cooperation) Projects (Ycgh2025009) and Yancheng Applied Basic Research Program under Grants YCBK2026008.

Data Availability Staement

The original contributions presented in the study are included in the article, further inquiries can be directed to the corresponding authors.

Conflicts of Interest

The authors declare no conflict of interest.

Use of AI and AI-assisted Technologies

No AI tools were utilized for this paper.

References

1. International Renewable Energy Agency (IRENA). *Renewable Capacity Statistics 2024*; IRENA: Abu Dhabi, United Arab Emirates, 2024.
2. National Energy Administration of China. *Monitoring and Evaluation Report on Renewable Energy Power Development in China in 2023 (in Chinese)*; NEA: Beijing, China, 2024.
3. International Energy Agency (IEA). *Global EV Outlook 2024*; IEA: Paris, France, 2024.
4. Zhao, Y.; Kang, Y.; Wozny, J.; et al. Recycling of sodium-ion batteries. *Nat. Rev. Mater.* **2023**, *8*, 623–634. https://doi.org/10.1038/s41578-023-00574-w.

5. Rystad Energy. *Energy Storage Outlook 2025*; Rystad Energy: Oslo, Norway, 2025.
6. Zuo, W.; Innocenti, A.; Zarrabeitia, M.; et al. Layered Oxide Cathodes for Sodium-Ion Batteries: Storage Mechanism, Electrochemistry, and Techno-economics. *Acc. Chem. Res.* **2023**, *56*, 284–296. https://doi.org/10.1021/acs.accounts.2c00690.
7. Wu, C.; Yang, Y.; Zhang, Y.; et al. Hard carbon for sodium-ion batteries: Progress, strategies and future perspective. *Chem. Sci.* **2024**, *15*, 6244–6268. https://doi.org/10.1039/d4sc00734d.
8. Abdul Salam, A.F.; Zheng, X.; Chen, Z.; et al. Sodium-ion battery development since 2020 with future perspectives. *J. Mater. Chem. A* **2026**, *14*, 9115–9137. https://doi.org/10.1039/d5ta07726e.
9. Sada, K.; Darga, J.; Manthiram, A. Challenges and Prospects of Sodium-Ion and Potassium-Ion Batteries for Mass Production. *Adv. Energy Mater.* **2023**, *13*, 2302321. https://doi.org/10.1002/aenm.202302321.
10. Xiao, B.; Zheng, Y.; Song, M.; et al. Protonation Stimulates the Layered to Rock Salt Phase Transition of Ni-Rich Sodium Cathodes. *Adv. Mater.* **2024**, *36*, 2308380. https://doi.org/10.1002/adma.202308380.
11. Bo, S.H.; Li, X.; Toumar, A.J.; et al. Layered-to-Rock-Salt Transformation in Desodiated Na_xCrO_2 ($x \leq 0.4$). *Chem. Mater.* **2016**, *28*, 1419–1429. https://doi.org/10.1021/acs.chemmater.5b04626.
12. Hu, J.; Li, X.; Liang, Q.; et al. Optimization Strategies of $Na_3V_2(PO_4)_3$ Cathode Materials for Sodium-Ion Batteries. *Nano-Micro Lett.* **2025**, *17*, 33. https://doi.org/10.1007/s40820-024-01526-x.
13. Xiao, Y.; Xiao, J.; Zhao, H.; et al. Prussian Blue Analogues for Sodium-Ion Battery Cathodes: A Review of Mechanistic Insights, Current Challenges, and Future Pathways. *Small* **2024**, *20*, 2401957. https://doi.org/10.1002/smll.202401957.
14. Meng, J.; Jia, G.; Yang, H.; et al. Recent advances for SEI of hard carbon anode in sodium-ion batteries: A mini review. *Front. Chem.* **2022**, *10*, 986541. https://doi.org/10.3389/fchem.2022.986541.
15. Lu, Z.; Yang, H.; Guo, Y.; et al. Consummating ion desolvation in hard carbon anodes for reversible sodium storage. *Nat. Commun.* **2024**, *15*, 3497. https://doi.org/10.1038/s41467-024-47522-y.
16. Zeng, Y.; Zhong, H.; Luo, Y.; et al. Interfacial engineering principles for hard carbon anodes in sodium-ion batteries: From mechanisms to synergistic strategies. *Energy Environ. Sci.* **2026**, *19*, 1775–1836. https://doi.org/10.1039/d5ee06849e.
17. Zuo, W.; Liu, Z.; Dopilka, A.; et al. Next-generation anodes for high-energy and low-cost sodium-ion batteries. *Nat. Rev. Mater.* **2026**, *11*, 117–135. https://doi.org/10.1038/s41578-025-00857-4.
18. He, Y.; Liu, D.; Li, Q.; et al. Advances in oxygen-containing functional groups-modified hard carbon anodes for sodium-ion batteries. *Mater. Sci. Eng. R Rep.* **2026**, *168*, 101143. https://doi.org/10.1016/j.mser.2025.101143.
19. Massaro, A.; Lingua, G.; Bozza, F.; et al. P2-Type $Na_{0.84}Li_{0.1}Ni_{0.27}Mn_{0.63}O_2$-Layered Oxide Na-Ion Battery Cathode: Structural Insights and Electrochemical Compatibility with Room-Temperature Ionic Liquids. *Chem. Mater.* **2024**, *36*, 7046–7055. https://doi.org/10.1021/acs.chemmater.4c01311.
20. Domalanta, M.R.B.; Castro, M.T.; del Rosario, J.A.D.; et al. Cost Analysis of a Sodium-ion Battery Pack for Energy and Power Applications using Combined Multi-physics and Techno-Economic Modeling. *Chem. Eng. Trans.* **2022**, *94*, 139–144. https://doi.org/10.3303/cet2294023.
21. Lodico, J.J.; Mecklenburg, M.; Chan, H.L.; et al. Operando spectral imaging of the lithium ion battery's solid-electrolyte interphase. *Sci. Adv.* **2023**, *9*, eadg5135. https://doi.org/10.1126/sciadv.adg5135.
22. Chen, Y.; Wu, W.; Gonzalez-Munoz, S.; et al. Nanoarchitecture factors of solid electrolyte interphase formation via 3D nano-rheology microscopy and surface force-distance spectroscopy. *Nat. Commun.* **2023**, *14*, 1321. https://doi.org/10.1038/s41467-023-37033-7.
23. Steinberg, Y.; Sebti, E.; Moroz, I.B.; et al. Composition and Structure of the solid electrolyte interphase on Na-Ion Anodes Revealed by Exo- and Endogenous Dynamic Nuclear Polarization–NMR Spectroscopy. *J. Am. Chem. Soc.* **2024**, *146*, 24476–24492. https://doi.org/10.1021/jacs.4c06823.
24. Marri, G.K.; Ee, Y.J.; He, Z.; et al. Recent advancements in internal and external thermoregulation strategies for lithium-ion batteries. *Renew. Sustain. Energy Rev.* **2026**, *225*, 116127. https://doi.org/10.1016/j.rser.2025.116127.
25. Wang, X.; Wang, X.; Li, L.; et al. Coupled pore-forming and sodium supplementation strategies for asphalt-based hard carbon anodes to enhance the cycling stability of sodium-ion batteries. *Mater. Sci. Eng. B* **2026**, *323*, 118833. https://doi.org/10.1016/j.mseb.2025.118833.
26. Walker, A.; Desai, J. *Battery Energy Storage System Evaluation Method*; U.S. Department of Energy Federal Energy Management Program (FEMP): Washington, DC, USA, 2023.
27. Luo, T.; Lin, S.; Zhang, C.; et al. A facile synthetic strategy to MnS/NC submicrospheres for high-performance sodium-ion battery anodes. *Mater. Res. Bull.* **2026**, *195*, 113862. https://doi.org/10.1016/j.materresbull.2025.113862.
28. Conover, D.R.; Crawford, A.J.; Fuller, J.; et al. *Protocol for Uniformly Measuring and Expressing the Performance of Energy Storage Systems*; Pacific Northwest National Laboratory and Sandia National Laboratories: Richland, WA, USA, 2016. https://doi.org/10.2172/1561194.
29. IEC. *ESRI and Standards Participation–New Proposal Initiated for Sodium-Ion Battery Chemistry*; IEC: Geneva, Switzerland, 2024.

30. Klick, S.; Laufen, H.; Schütte, M.; et al. Failure Mode and Degradation Analysis of a Commercial Sodium-Ion Battery with Severe Gassing Issue. *Batter. Supercaps* **2025**, *8*, e202400546. https://doi.org/10.1002/batt.202400546.
31. Tan, R.; Hong, W.; Tang, J.; et al. BatteryLife: A Comprehensive Dataset and Benchmark for Battery Life Prediction. In Proceedings of the KDD '25: The 31st ACM SIGKDD Conference on Knowledge Discovery and Data Mining, Toronto, ON, Canada, 3–7 August 2025; pp. 5789–5800. https://doi.org/10.1145/3711896.3737372.
32. TWAICE. *Simulation Model for Sodium-Ion Batteries—Aging Model for Emerging Sodium-Ion Technology*; TWAICE Technologies GmbH: Munich, Germany, 2024.
33. Feng, X.; Li, Y.; Li, Y.; et al. Unlocking the local structure of hard carbon to grasp sodium-ion diffusion behavior for advanced sodium-ion batteries. *Energy Environ. Sci.* **2024**, *17*, 1387–1396. https://doi.org/10.1039/d3ee03347c.
34. Chen, T.; Ouyang, B.; Fan, X.; et al. Oxide cathodes for sodium-ion batteries: Designs, challenges, and perspectives. *Carbon Energy* **2022**, *4*, 170–199. https://doi.org/10.1002/cey2.153.
35. Guo, Y.J.; Jin, R.X.; Fan, M.; et al. Sodium layered oxide cathodes: Properties, practicality and prospects. *Chem. Soc. Rev.* **2024**, *53*, 7828–7874. https://doi.org/10.1039/d4cs00415a.
36. Liu, R.; Huang, W.; Liu, J.; et al. Revealing the Nature of Binary-Phase on Structural Stability of Sodium Layered Oxide Cathodes. *Adv. Mater.* **2024**, *36*, 2401048. https://doi.org/10.1002/adma.202401048.
37. Chen, C.; Ding, Z.; Han, Z.; et al. Unraveling Atomically Irreversible Cation Migration in Sodium Layered Oxide Cathodes. *J. Phys. Chem. Lett.* **2020**, *11*, 5464–5470. https://doi.org/10.1021/acs.jpclett.0c01285.
38. Jian, Z.C.; Guo, J.X.; Liu, Y.F.; et al. Cation migration in layered oxide cathodes for sodium-ion batteries: Fundamental failure mechanisms and practical modulation strategies. *Chem. Sci.* **2024**, *15*, 19698–19728. https://doi.org/10.1039/d4sc05206d.
39. Hou, D.; Gabriel, E.; Graff, K.; et al. Thermal dynamics of P2-$Na_{0.67}Ni_{0.33}Mn_{0.67}O_2$ cathode materials for sodium ion batteries studied by in situ analysis. *J. Mater. Res.* **2022**, *37*, 1156–1163. https://doi.org/10.1557/s43578-022-00519-z.
40. Chen, D.; Zhang, H.; Yang, H.Y.; et al. Promoting Na-ion storage in P2-$Na_{0.67}Ni_{0.33}Mn_{0.67}O_2$ cathode via synergetic Ti and Zn Co-incorporation. *Appl. Phys. Lett.* **2024**, *124*, 083904. https://doi.org/10.1063/5.0188032.
41. Sun, Y.; Zhou, P.; Liu, S.; et al. Manipulating Na occupation and constructing protective film of P2-$Na_{0.67}Ni_{0.33}Mn_{0.67}O_2$ as long-term cycle stability cathode for sodium-ion batteries. *J. Energy Chem.* **2024**, *88*, 603–611. https://doi.org/10.1016/j.jechem.2023.09.042.
42. Wu, S.Y.; Wu, F.; Ye, X.; et al. Inhibiting the P2–O2 phase transition of P2-$Na_{0.67}Ni_{0.33}Mn_{0.67}O_2$ via high-valence tungsten doping for sodium-ion batteries. *Rare Met.* **2025**, *44*, 3806–3816. https://doi.org/10.1007/s12598-024-03217-3.
43. Liang, X.; Song, X.; Sun, H.H.; et al. High-energy and long-life O3-type layered cathode material for sodium-ion batteries. *Nat. Commun.* **2025**, *16*, 3505. https://doi.org/10.1038/s41467-025-58637-1.
44. Zhao, X.; Liu, Q.; He, W.; et al. Uniform Al_2O_3 coating for improved cycling stability of O3-type sodium-ion batteries cathode: Mechanisms and performance insights. *J. Energy Storage* **2025**, *131*, 117548. https://doi.org/10.1016/j.est.2025.117548.
45. Xiao, J.; Xiao, Y.; Wang, S.; et al. Surface engineering of P2-type cathode material targeting long-cycling and high-rate sodium-ion batteries. *J. Energy Chem.* **2024**, *97*, 444–452. https://doi.org/10.1016/j.jechem.2024.06.007.
46. Wang, H.; Zhou, L.; Cheng, Z.; et al. Recent Advances on F-Doped Layered Transition Metal Oxides for Sodium Ion Batteries. *Molecules* **2023**, *28*, 8065. https://doi.org/10.3390/molecules28248065.
47. Li, Y.; Zhou, Q.; Weng, S.; et al. Interfacial engineering to achieve an energy density of over 200 Wh kg^{-1} in sodium batteries. *Nat. Energy* **2022**, *7*, 511–519. https://doi.org/10.1038/s41560-022-01033-6.
48. Massaro, A.; Porporato, S.; Botros, M.; et al. Entropy-driven mechanisms in P2-type layered oxide cathodes for sodium-ion batteries: New insights from first-principles and electrochemical analysis. *J. Mater. Chem. A* **2026**, *14*, 19341–19353. https://doi.org/10.1039/d6ta00673f.
49. Huang, S.; Huang, M.; Liu, L.; et al. O3-$NaNi_{1/3}Fe_{1/3}Mn_{1/3}O_2$ material with excellent rate capability and cycling stability: A strategy of Ce^{4+} doping to facilitate reversible O3–P3–O3 phase transformation and mitigate lattice distortion. *J. Alloys Compd.* **2025**, *1035*, 181503. https://doi.org/10.1016/j.jallcom.2025.181503.
50. Pamidi, V.; Trivedi, S.; Behara, S.; et al. Micron-sized single-crystal cathodes for sodium-ion batteries. *iScience* **2022**, *25*, 104205. https://doi.org/10.1016/j.isci.2022.104205.
51. Xu, G.L.; Liu, X.; Zhou, X.; et al. Native lattice strain induced structural earthquake in sodium layered oxide cathodes. *Nat. Commun.* **2022**, *13*, 436. https://doi.org/10.1038/s41467-022-28052-x.
52. Feng, L.; Xia, Y.; Guo, J.; et al. La-doped O3-type layered oxide cathode with enhanced cycle stability for sodium-ion batteries. *Chem. Eng. J.* **2024**, *496*, 154298. https://doi.org/10.1016/j.cej.2024.154298.
53. Kuang, Y.; Wu, Y.; Zhang, H.; et al. Interface Issues of Layered Transition Metal Oxide Cathodes for Sodium-Ion Batteries: Current Status, Recent Advances, Strategies, and Prospects. *Molecules* **2024**, *29*, 5988. https://doi.org/10.3390/molecules29245988.
54. Moossa, B.; Abraham, J.J.; Ahmed, A.M.; et al. Synergistic effect of NASICON $Na_3V_2(PO_4)_2F_3$ and 2D MXene for high-performance symmetric Sodium-ion batteries. *Mater. Res. Bull.* **2025**, *182*, 113173. https://doi.org/10.1016/j.materresbull.2024.113173.

55. Chen, J.; Wu, X.; Luo, Z.; et al. Nanotechnology engineering of polyanionic $Na_3V_2(PO_4)_2F_3$ cathodes toward high-performance sodium-ion batteries. *Chem. Sci.* **2026**, *17*, 6848–6882. https://doi.org/10.1039/d5sc10141g.
56. Liao, X.; Wu, X.; Xie, M.; et al. Leveraging high-entropy substitution to achieve V^{4+}/V^{5+} redox couple and superior Na^+ storage in $Na_3V_2(PO_4)_3$-based cathodes for sodium-ion battery. *Energy Storage Mater.* **2025**, *77*, 104166. https://doi.org/10.1016/j.ensm.2025.104166.
57. Yin, R.; Guo, Z.; Liu, R.; et al. Ultrafast synthesis of $Na_3V_2(PO_4)_3$ cathode for high performance sodium-ion batteries. *Chin. Chem. Lett.* **2025**, *36*, 109643. https://doi.org/10.1016/j.cclet.2024.109643.
58. Kang, Y.; Lin, X.; Tong, S.; et al. Synergetic impact of high-entropy microdoping modification in $Na_3V_2(PO_4)_3$. *Chem. Commun.* **2024**, *60*, 2512–2515. https://doi.org/10.1039/d4cc00033a.
59. Zhou, M.; Zhou, X.; Li, L.; et al. Emerging high voltage V^{4+}/V^{5+} redox reactions in $Na_3V_2(PO_4)_3$-based cathodes for sodium-ion batteries. *Chem. Sci.* **2024**, *15*, 8651–8663. https://doi.org/10.1039/d4sc01226g.
60. Subaşı, Y.; Altenschmidt, L.; Lindgren, F.; et al. Synthesis and characterization of a crystalline $Na_4Fe_3(PO_4)_2(P_2O_7)$ cathode material for sodium-ion batteries. *J. Mater. Chem. A* **2024**, *12*, 23506–23517. https://doi.org/10.1039/d4ta03554b.
61. Xiong, F.; Li, J.; Zuo, C.; et al. Mg-Doped $Na_4Fe_3(PO_4)_2(P_2O_7)$/C Composite with Enhanced Intercalation Pseudocapacitance for Ultra-Stable and High-Rate Sodium-Ion Storage. *Adv. Funct. Mater.* **2023**, *33*, 2211257. https://doi.org/10.1002/adfm.202211257.
62. Wu, H.; Chen, Y.; Wen, T.; et al. Advances in Vanadium-Redoxed Polyanions for High-Voltage Sodium-Ion Batteries. *Batteries* **2023**, *9*, 56. https://doi.org/10.3390/batteries9010056.
63. Jiang, N.; Wang, X.; Zhou, H.; et al. Achieving Fast and Stable Sodium Storage in $Na_4Fe_3(PO_4)_2(P_2O_7)$ via Entropy Engineering. *Small* **2024**, *20*, 2308681. https://doi.org/10.1002/smll.202308681.
64. Zhou, Q.; Wang, Y.; Ou, R.; et al. Yolk-Shell Construction of $Na_3V_2(PO_4)_2F_3$ with Copper Substitution Microsphere as High-Rate and Long-Cycling Cathode Materials for Sodium-Ion Batteries. *Small* **2024**, *20*, 2310699. https://doi.org/10.1002/smll.202310699.
65. Mahato, S.; Das, S.; Gupta, D.; et al. Vanadium substituted Fe, Cr co-doped high performance C/$Na_3V_2(PO_4)_2F_3$ cathode for sodium-ion batteries. *J. Electroanal. Chem.* **2024**, *955*, 118046. https://doi.org/10.1016/j.jelechem.2024.118046.
66. Zhao, A.; Fang, Y.; Ai, X.; et al. Mixed polyanion cathode materials: Toward stable and high-energy sodium-ion batteries. *J. Energy Chem.* **2021**, *60*, 635–648. https://doi.org/10.1016/j.jechem.2021.01.014.
67. Liang, Y.; Xu, L.; Chen, Z.; et al. Recent research progress in the application of $Na_3V_2(PO_4)_2F_3$ cathode materials in sodium-ion batteries: Synthesis, modification, and battery optimization. *Energy Mater.* **2025**, *5*, 500115. https://doi.org/10.20517/energymater.2024.306.
68. Zhou, B.; Gao, Y.; Lin, X.; et al. Bulk and interface engineering of Prussian blue analogue cathodes for high-performance sodium-ion batteries. *Chem. Sci.* **2025**, *16*, 13594–13628. https://doi.org/10.1039/d5sc02819a.
69. Sun, S.; Jiang, X.; Wang, Z.; et al. Prussian blue analogues for high-performance sodium ion battery cathodes: Recent advances and challenges. *Dalton Trans.* **2025**, *54*, 14254–14261. https://doi.org/10.1039/d5dt01534k.
70. Xu, X.; Zhu, S.; Yang, C.; et al. A novel strategy for the reduction of coordinated water in Prussian blue analogues for their application as cathode materials for sodium-ion batteries. *J. Mater. Chem. A* **2025**, *13*, 11848–11860. https://doi.org/10.1039/d5ta00120j.
71. Li, Z.; Zhong, S.; Zhou, B.; et al. Synthesis of Low-Defect Iron-Based Prussian Blue with Low Water Content for High-Stability Sodium-Ion Batteries. *Materials* **2025**, *18*, 1455. https://doi.org/10.3390/ma18071455.
72. Cheng, H.; Liu, Y.N.; Wang, D.; et al. Ball-milling synthesis of low-water and phase-stable Prussian blue for sodium-ion batteries. *Solid State Ionics* **2024**, *414*, 116633. https://doi.org/10.1016/j.ssi.2024.116633.
73. Wang, Y.; Jiang, N.; Yang, C.; et al. High-entropy prussian blue analogs with 3D confinement effect for long-life sodium-ion batteries. *J. Mater. Chem. A* **2024**, *12*, 5170–5180. https://doi.org/10.1039/d3ta07671g.
74. Li, C.; Xiao, Y.; Zhang, D.; et al. Stable Manganese-Based High-Entropy Prussian Blue for Enhanced Sodium-Ion Storage. *Batteries* **2025**, *11*, 328. https://doi.org/10.3390/batteries11090328.
75. He, B.; Huang, M.; Yu, Y.; et al. High-Entropy Prussian Blue Analogs via a Solid-Solution Storage Mechanism for Long Cycle Sodium-Ion Batteries Cathodes. *Chem. A Eur. J.* **2025**, *31*, e202500880. https://doi.org/10.1002/chem.202500880.
76. Liu, S.; Yu, H.; Zhao, Y.; et al. Inhibiting Phase Transitions of Prussian Blue Analogs with High-Entropy Strategy for Ultralong-Life Sodium-Ion Battery Cathodes. *Small* **2025**, *21*, 2504893. https://doi.org/10.1002/smll.202504893.
77. Goel, G.; Sharma, M.; Tripathi, S.K.; et al. Prussian blue analogue as cathode materials in sodium ion batteries: A review. *J. Energy Storage* **2025**, *126*, 116995. https://doi.org/10.1016/j.est.2025.116995.
78. Zhao, X.; Xing, Z.; Huang, C.; et al. Investigation of high-entropy Prussian blue analog as cathode material for aqueous sodium-ion batteries. *J. Mater. Chem. A* **2023**, *11*, 22835–22844. https://doi.org/10.1039/d3ta04349e.
79. Shi, Q.; Qi, R.; Feng, X.; et al. Niobium-doped layered cathode material for high-power and low-temperature sodium-ion batteries. *Nat. Commun.* **2022**, *13*, 3205. https://doi.org/10.1038/s41467-022-30942-z.

80. Yu, R.; Liu, S.; Li, X.; et al. Study on Thermal Behavior and Safety Properties of $Na_4Fe_3(PO_4)_2(P_2O_7)$ and $NaNi_{1/3}Fe_{1/3}Mn_{1/3}O_2$ Cathode-Based Sodium Ion Battery. *Batteries* **2025**, *11*, 184. https://doi.org/10.3390/batteries11050184.
81. Jing, Z.; Kong, L.; Mamoor, M.; et al. Rational Design of Prussian Blue Analogues for Ultralong and Wide-Temperature-Range Sodium-Ion Batteries. *J. Am. Chem. Soc.* **2025**, *147*, 3702–3713. https://doi.org/10.1021/jacs.4c16031.
82. Wang, X.; Li, H.; Zhang, W.; et al. Unlocking fast and highly reversible sodium storage in Fe-based mixed polyanion cathodes for low-cost and high-performance sodium-ion batteries. *J. Mater. Chem. A* **2023**, *11*, 6978–6985. https://doi.org/10.1039/d3ta00014a.
83. Zou, Z.; Mu, Y.; Han, M.; et al. Integrated polyanion-layered oxide cathodes enabling 100,000 cycle life for sodium-ion batteries. *Energy Environ. Sci.* **2025**, *18*, 2216–2230. https://doi.org/10.1039/d4ee05110f.
84. Cai, T.; Chen, A.; Liang, S.; et al. Machine Learning for Design and Full Chain Research of High-Entropy Na-Ion Cathodes. *Adv. Mater.* **2025**, *37*, e08717. https://doi.org/10.1002/adma.202508717.
85. Rexhausen, W.; Parsons, C.; Garg, U.; et al. Improved interfacial resistance and crystal-structure stability in a low-cobalt P2-type sodium-ion battery cathode material. *arXiv* **2024**, arXiv:2408.01595.
86. Pati, J.; Dhaka, R.S. Mixed polyanionic $NaFe_{1.6}V_{0.4}(PO_4)(SO_4)_2$@CNT cathode for sodium-ion batteries: Electrochemical diffusion kinetics and distribution of relaxation time analysis at different temperatures. *J. Power Sources* **2024**, *609*, 234646. https://doi.org/10.1016/j.jpowsour.2024.234646.
87. Yang, H.; Li, C.; He, L.; et al. Advances in modification strategies of Prussian blue-type cathode materials for sodium-ion batteries. *J. Mater. Eng.* **2025**, *53*, 42–56. https://doi.org/10.11868/j.issn.1001-4381.2024.000625.
88. Zhang, L.; Zhang, Y.; Ma, Y.; et al. Research progress on sodium-ion battery cathode materials based on iron-based Prussian blue analogues. *Energy Storage Sci. Technol.* **2025**, *14*, 525–543. https://doi.org/10.19799/j.cnki.2095-4239.2024.0663.
89. Chen, X.; Wang, C.; Zhao, Y.; et al. Recent progress in layered oxide cathodes for sodium-ion batteries: Stability, phase transition and solutions. *J. Mater. Chem. A* **2024**, *12*, 31797–31817. https://doi.org/10.1039/d4ta03372h.
90. Rostami, H.; Valio, J.; Suominen, P.; et al. Advancements in cathode technology, recycling strategies, and market dynamics: A comprehensive review of sodium ion batteries. *Chem. Eng. J.* **2024**, *495*, 153471. https://doi.org/10.1016/j.cej.2024.153471.
91. Wu, X.; Liu, A.; Lu, S.; et al. Enhancing Voltage Output in Polyanion-Type Cathode Materials for Sodium Ion Batteries. *Batter. Supercaps* **2024**, *7*, e202400290. https://doi.org/10.1002/batt.202400290.
92. Li, Z. Optimization of Interface and Solid Phase Structure of Prussian Blue Analogue Cathode for Sodium Ion Battery. *J. Adv. Phys. Chem.* **2024**, *13*, 670–684. https://doi.org/10.12677/japc.2024.134069.
93. Xu, C.; Zhao, J.; Yang, C.; et al. Polyanionic Cathode Materials for Practical Na-Ion Batteries toward High Energy Density and Long Cycle Life. *ACS Cent. Sci.* **2023**, *9*, 1721–1736. https://doi.org/10.1021/acscentsci.3c00907.
94. Liu, Z.; Lu, Z.; Guo, S.; et al. Toward High Performance Anodes for Sodium-Ion Batteries: From Hard Carbons to Anode-Free Systems. *ACS Cent. Sci.* **2023**, *9*, 1076–1087. https://doi.org/10.1021/acscentsci.3c00301.
95. Zhang, M.; Li, Y.; Wu, F.; et al. Boost sodium-ion batteries to commercialization: Strategies to enhance initial Coulombic efficiency of hard carbon anode. *Nano Energy* **2021**, *82*, 105738. https://doi.org/10.1016/j.nanoen.2020.105738.
96. Tang, Z.; Zhang, R.; Wang, H.; et al. Revealing the closed pore formation of waste wood-derived hard carbon for advanced sodium-ion battery. *Nat. Commun.* **2023**, *14*, 6024. https://doi.org/10.1038/s41467-023-39637-5.
97. Gabrijelcič, M.; Tratnik, B.; Kapun, G.; et al. Probing sodium structures and dynamics in hard carbon for Na-ion batteries using ^{23}Na operando solid-state NMR spectroscopy. *J. Mater. Chem. A* **2025**, *13*, 1042–1056.
98. Li, Q.; Liu, X.; Tao, Y.; et al. Sieving carbons promise practical anodes with extensible low-potential plateaus for sodium batteries. *Natl. Sci. Rev.* **2022**, *9*, nwac084. https://doi.org/10.1093/nsr/nwac084.
99. Stratford, J.M.; Kleppe, A.K.; Keeble, D.S.; et al. Correlating Local Structure and Sodium Storage in Hard Carbon Anodes: Insights from Pair Distribution Function Analysis and Solid-State NMR. *J. Am. Chem. Soc.* **2021**, *143*, 14274–14286. https://doi.org/10.1021/jacs.1c06058.
100. Reynolds, E.M.; Fitzpatrick, J.; Jones, M.O.; et al. Investigation of sodium insertion in hard carbon with operando small angle neutron scattering. *J. Mater. Chem. A* **2024**, *12*, 18469–18475. https://doi.org/10.1039/d3ta04739c.
101. Qiu, C.; Li, A.; Qiu, D.; et al. One-Step Construction of Closed Pores Enabling High Plateau Capacity Hard Carbon Anodes for Sodium-Ion Batteries: Closed-Pore Formation and Energy Storage Mechanisms. *ACS Nano* **2024**, *18*, 11941–11954. https://doi.org/10.1021/acsnano.4c02046.
102. Zhang, X.; Cao, Y.; Li, G.; et al. Exploring Carbonization Temperature to Create Closed Pores for Hard Carbon as High-Performance Sodium-Ion Battery Anodes. *Small* **2024**, *20*, 2311197. https://doi.org/10.1002/smll.202311197.
103. Li, X.; Ding, C.; Liang, Q.; et al. Progress in hard carbons for sodium-ion batteries: Microstructure, sodium storage mechanism and initial Coulombic efficiency. *J. Energy Storage* **2024**, *98*, 112986. https://doi.org/10.1016/j.est.2024.112986.
104. Ma, R.; Chen, Y.; Li, Q.; et al. Oxygen-driven closing pore formation in coal-based hard carbon for low-voltage rapid sodium storage. *Chem. Eng. J.* **2024**, *493*, 152389. https://doi.org/10.1016/j.cej.2024.152389.

105. Wu, S.; Peng, H.; Xu, J.; et al. Nitrogen/phosphorus co-doped ultramicropores hard carbon spheres for rapid sodium storage. *Carbon* **2024**, *218*, 118756. https://doi.org/10.1016/j.carbon.2023.118756.
106. Zhang, Y.; Zhang, S.W.; Chu, Y.; et al. Redefining closed pores in carbons by solvation structures for enhanced sodium storage. *Nat. Commun.* **2025**, *16*, 3634. https://doi.org/10.1038/s41467-025-59022-8.
107. Qiu, R.; Ma, D.; Zheng, H.; et al. Performance degradation mechanisms and mitigation strategies of hard carbon anode and solid electrolyte interface for sodium-ion battery. *Nano Energy* **2024**, *128*, 109920. https://doi.org/10.1016/j.nanoen.2024.109920.
108. Wang, L.; Jia, G.; Chen, Y.; et al. Review, analysis, and outlook of anode materials for sodium-ion batteries. *Ionics* **2026**, *32*, 1263–1307. https://doi.org/10.1007/s11581-025-06748-6.
109. Gan, S.; Huang, Y.; Hong, N.; et al. Comprehensive Understanding of Closed Pores in Hard Carbon Anode for High-Energy Sodium-Ion Batteries. *Nano-Micro Lett.* **2025**, *17*, 325. https://doi.org/10.1007/s40820-025-01833-x.
110. Li, R.; Yuan, B.; Feng, Y.; et al. Molecular-level precursor engineering enables high utilization of closed nanopores in hard carbon for sodium-ion batteries. *Chem. Sci.* **2026**, *17*, 10489–10503. https://doi.org/10.1039/d6sc01648k.
111. Shen, T.; Sun, Y.; He, Z.; et al. Effect of pore structure regulation in coconut shell-derived hard carbon on sodium storage capacity. *Electrochim. Acta* **2025**, *538*, 147046. https://doi.org/10.1016/j.electacta.2025.147046.
112. Shang, L.; Yuan, R.; Liu, H.; et al. Precursor screening of fruit shell derived hard carbons for low-potential sodium storage: A low lignin content supports the formation of closed pores. *Carbon* **2024**, *223*, 119038. https://doi.org/10.1016/j.carbon.2024.119038.
113. Hou, W.; Ma, L.; Liu, Z.; et al. Construction of hard carbon with abundant closed ultra-micropores via a pre-oxidation strategy for high-efficiency sodium storage in the low potential plateau. *J. Energy Chem.* **2025**, *105*, 65–75. https://doi.org/10.1016/j.jechem.2025.01.042.
114. Eren, E.O.; Senokos, E.; Scoppola, E.; et al. An enhanced three-stage model for sodium storage in hard carbons. *Energy Environ. Sci.* **2025**, *18*, 7859–7868. https://doi.org/10.1039/d4ee06029f.
115. Jia, Z.; Hou, S.; Chen, X.; et al. Tailoring hard carbon interfaces in carbonate-based electrolytes for sodium-ion hybrid capacitors. *Energy Mater.* **2025**, *5*, 500073. https://doi.org/10.20517/energymater.2024.291.
116. Lin, S.; Zhang, H.; Shu, C.; et al. Research Progress and Perspectives on Pre-Sodiation Strategies for Sodium-Ion Batteries. *Adv. Funct. Mater.* **2024**, *34*, 2409628. https://doi.org/10.1002/adfm.202409628.
117. Liu, L.; Xiao, L.; Sun, Z.; et al. Rational manipulation of electrolyte to induce homogeneous SEI on hard carbon anode for sodium-ion battery. *J. Energy Chem.* **2024**, *94*, 414–429. https://doi.org/10.1016/j.jechem.2024.02.055.
118. Liao, Y.; Liu, H.; Zhang, Y.; et al. A Weak-Fluorine-Bond Molecule Stabilizes Hard Carbon Anodes for Practical Sodium-Ion Batteries. *ACS Nano* **2025**, *19*, 30466–30475. https://doi.org/10.1021/acsnano.5c10983.
119. Sun, Y.; Zuo, D.; Xu, C.; et al. A "grafting technique" to tailor the interfacial behavior of hard carbon anodes for stable sodium-ion batteries. *Energy Environ. Sci.* **2025**, *18*, 1911–1919. https://doi.org/10.1039/d4ee05305b.
120. Zhang, W.; Du, Y.; Qiu, Y.; et al. Closed-Pore Engineering in Hard Carbon for Sodium Ion Storage: Advances, Challenges and Future Horizons. *Adv. Energy Mater.* **2025**, *15*, e03884. https://doi.org/10.1002/aenm.202503884.
121. Sun, C.; Zhang, X.; Li, C.; et al. A safe, low-cost and high-efficiency presodiation strategy for pouch-type sodium-ion capacitors with high energy density. *J. Energy Chem.* **2022**, *64*, 442–450. https://doi.org/10.1016/j.jechem.2021.05.010.
122. Wang, Y.; Yu, Z.; Li, Q.; et al. Recent advances in presodiation strategies for hard carbon anodes in sodium-ion batteries. *Chem. Commun.* **2025**, *61*, 15061–15067. https://doi.org/10.1039/d5cc04339e.
123. Yuan, W.; Li, X.; Lu, X.; et al. Pre-sodiation strategies for sodium-ion batteries with hard carbon anodes: Techniques, challenges, and future directions. *Mater. Sci. Eng. B* **2025**, *319*, 118378. https://doi.org/10.1016/j.mseb.2025.118378.
124. Deori, D.; Buragohain, M.; Son, Y.; et al. Self-Healing, Ga-Sb Alloy Confined Sn Anode for Stable Na-Ion Storage in Glyme Based Electrolytes. *Small* **2025**, *21*, 2504185. https://doi.org/10.1002/smll.202504185.
125. Bai, X.; Wu, N.; Yu, G.; et al. Recent Advances in Anode Materials for Sodium-Ion Batteries. *Inorganics* **2023**, *11*, 289. https://doi.org/10.3390/inorganics11070289.
126. Kojima, T.; Kitta, M.; Kataoka, R.; et al. Sodiation and Delithiation of $Li_4Ti_5O_{12}$ for the Synthesis of Spinel-Type Sodium Titanium Oxide as an Anode Material for Sodium-Ion Batteries. *J. Electrochem. Soc.* **2023**, *170*, 090531. https://doi.org/10.1149/1945-7111/acf95d.
127. Li, F.; Mo, F.; Zhong, C.; et al. A roadmap toward high-performance hard carbon for sodium-ion batteries: From fundamental studies on synthesis and mechanism to practical application. *Energy Storage Mater.* **2025**, *83*, 104668. https://doi.org/10.1016/j.ensm.2025.104668.
128. Cheng, F.; Hu, J.; Zhang, W.; et al. Reviving ether-based electrolytes for sodium-ion batteries. *Energy Environ. Sci.* **2025**, *18*, 6874–6898. https://doi.org/10.1039/d5ee00725a.
129. Chen, Z.; Yang, L.; Yu, G.; et al. Progress and Prospects in Sodium-Ion Battery Anode Materials: From Fundamentals to Material Engineering Strategies. *Energy Storage Mater.* **2026**, *84*, 104745. https://doi.org/10.1016/j.ensm.2025.104745.

130. Hu, C.; Guo, S.; Huang, F.; et al. Carbonate ester-based sodium metal battery with high-capacity retention at −50 °C enabled by weak solvents and electrodeposited anode. *Angew. Chem. Int. Ed.* **2024**, *63*, e202407075. https://doi.org/10.1002/anie.202407075.
131. Zhang, L.; Liu, Z.; Zhang, X.; et al. Synergistic effect of cathode and electrolyte additives on stabilizing the anodic interface for sodium-based dual-carbon batteries. *J. Alloys Compd.* **2023**, *942*, 168863. https://doi.org/10.1016/j.jallcom.2023.168863.
132. Liu, D.; Zhu, H.; Sun, R.; et al. Synergistic dual-additive boost cyclability of sodium-ion batteries. *Energy Storage Sci. Technol.* **2025**, *14*, 1858–1865. https://doi.org/10.19799/j.cnki.2095-4239.2024.1143.
133. Dey, A.; Pramanik, A.; Purohit, S.; et al. Stable Na^+ Ion Storage via Dual Active Sites Utilization in Covalent Organic Framework-Carbon Nanotube Composite. *ChemSusChem* **2025**, *18*, e202402325. https://doi.org/10.1002/cssc.202402325.
134. Zhang, Z.; Fan, Z.; Li, J.; et al. Research Progress on Electrolyte Additives for Sodium Ion Batteries. *Sustain. Polym. Energy* **2024**, *2*, 10003. https://doi.org/10.35534/spe.2024.10003.
135. Xia, M.; Chen, H.; Zheng, Z.; et al. Sodium-Difluoro(oxalato)Borate-Based Electrolytes for Long-Term Cycle Life and Enhanced Low-Temperature Sodium-Ion Batteries. *Adv. Energy Mater.* **2025**, *15*, 2403306. https://doi.org/10.1002/aenm.202403306.
136. Edelman, D.A.; Brandt, T.G.; Temeche, E.; et al. Sodium-based solid electrolytes and interfacial stability. Towards solid-state sodium batteries. *Mater. Today Commun.* **2022**, *32*, 104009. https://doi.org/10.1016/j.mtcomm.2022.104009.
137. Tian, Z.; Zou, Y.; Liu, G.; et al. Electrolyte Solvation Structure Design for Sodium Ion Batteries. *Adv. Sci.* **2022**, *9*, 2201207. https://doi.org/10.1002/advs.202201207.
138. He, J.; Bhargav, A.; Su, L.; et al. Tuning the solvation structure with salts for stable sodium-metal batteries. *Nat. Energy* **2024**, *9*, 446–456. https://doi.org/10.1038/s41560-024-01469-y.
139. Cheng, Z.; Zhang, Z.; Qiu, F.; et al. Regulating Solvation Shell to Fortify Anion–Cation Coordination for Enhanced Sodium Metal Battery Stability. *ACS Energy Lett.* **2025**, *10*, 177–184. https://doi.org/10.1021/acsenergylett.4c02751.
140. Ke, J.; Kim, Y.; Su, L. Localized High-Concentration Electrolytes for Sodium Batteries: Fundamentals, Challenges, and Applications. *ACS Appl. Energy Mater.* **2025**, *8*, 8850–8861. https://doi.org/10.1021/acsaem.5c01221.
141. Zhu, B.; Gao, J.; Li, S.; et al. Anion competitive coordination for solvation structure regulation in high-voltage sodium-ion batteries. *Chem. Eng. J.* **2025**, *519*, 165626. https://doi.org/10.1016/j.cej.2025.165626.
142. Ren, D.; Lu, L.; Hua, R.; et al. Challenges and opportunities of practical sulfide-based all-solid-state batteries. *eTransportation* **2023**, *18*, 100272. https://doi.org/10.1016/j.etran.2023.100272.
143. Yang, S.; Tang, Y.; Yao, Y.; et al. Sulfide electrolytes for all-solid-state sodium batteries: Fundamentals and modification strategies. *Mater. Horiz.* **2025**, *12*, 1058–1083. https://doi.org/10.1039/d4mh01218f.
144. Kan, R.; Xu, Y.; Chen, R.; et al. Thermal effects of solid-state batteries at different temperature: Recent advances and perspectives. *Energy Storage Mater.* **2024**, *68*, 103366. https://doi.org/10.1016/j.ensm.2024.103366.
145. Königsreiter, J.; Gadermaier, B.; Wilkening, H.M.R.; et al. Unveiling Ultra-High Ionic Conductivity in W-Doped Na_3SbS_4: Grain Boundary Effects and Pure Bulk Transport. *J. Am. Chem. Soc.* **2025**, *147*, 20092–20097. https://doi.org/10.1021/jacs.5c05842.
146. Tao, H.Q.; Yin, J.; Shen, Y.; et al. Achievement of high ionic conductivity and electrochemical stability by W/Sn-doped Na_3SbS_4 conductors designed for all-solid-state sodium-ion batteries. *J. Mater. Chem. C* **2024**, *12*, 19296–19306. https://doi.org/10.1039/d4tc03109a.
147. Huang, L.; Huang, C. Inorganic Sodium Solid-State Electrolytes: Progress, Existing Issues, and Solutions Towards High-Performance All Solid-State Batteries. *Electrochem. Energy Rev.* **2026**, *9*, 6. https://doi.org/10.1007/s41918-026-00279-y.
148. Sun, C.; Xie, L.; Wang, B.; et al. Improve the cycling performance of solid-state sodium batteries through the design of a cathode interface buffering layer. *Appl. Surf. Sci.* **2025**, *680*, 161265. https://doi.org/10.1016/j.apsusc.2024.161265.
149. Jiang, Y.; Wang, R.; Xiong, P.; et al. A solid dual-salt plastic crystal electrolyte enabling rapid ion transfer and stable interphases for high-performance solid-state sodium ion batteries. *Chem. Sci.* **2026**, *17*, 4529–4537. https://doi.org/10.1039/d5sc09186a.
150. Tian, K.; Wei, C.; Wang, Z.; et al. Stable sodium metal anode enabled by interfacial room-temperature liquid metal engineering for high-performance sodium–sulfur batteries with carbonate-based electrolyte. *Interdiscip. Mater.* **2024**, *3*, 425–436. https://doi.org/10.1002/idm2.12163.
151. Li, M.; Sun, C.; Zhang, R.; et al. Unveiling the Electrolyte and Solid Electrolyte Interphase in Sodium Ion Batteries: Mechanisms, Progress, and Perspectives. *Adv. Mater.* **2025**, *37*, e10882. https://doi.org/10.1002/adma.202510882.
152. Li, W.; Wang, W.; Jing, S.; et al. Bio-inspired binder with multi-bond interactions for stress dissipation enables stabilization of electrode structure in lithium-ion batteries. *Energy Storage Mater.* **2026**, *84*, 104797. https://doi.org/10.1016/j.ensm.2025.104797.
153. Jiang, H.; Mo, Z.; Xie, X.; et al. Bio-Inspired Self-Healing Silicon Anodes: Harnessing Tea Polyphenols to Enhance Lithium-Ion Battery Performance. *ACS Appl. Mater. Interfaces* **2024**, *16*, 59291–59301. https://doi.org/10.1021/acsami.4c12880.

154. Passerini, S.; Barelli, L.; Baumann, M.; et al. *Emerging Battery Technologies to Boost the Clean Energy Transition: Cost, Sustainability, and Performance Analysis*; Springer: Cham, Switzerland, 2024. https://doi.org/10.1007/978-3-031-48359-2.
155. Li, S.; Yang, Z.; Wang, S.B.; et al. Sulfide-based composite solid electrolyte films for all-solid-state batteries. *Commun. Mater.* **2024**, *5*, 44. https://doi.org/10.1038/s43246-024-00482-8.
156. Cai, X.; Yue, Y.; Yi, Z.; et al. Challenges and industrial perspectives on the development of sodium ion batteries. *Nano Energy* **2024**, *129*, 110052. https://doi.org/10.1016/j.nanoen.2024.110052.
157. Phogat, P.; Rawat, S.; Dey, S.; et al. Advancements and challenges in sodium-ion batteries: A comprehensive review of materials, mechanisms, and future directions for sustainable energy storage. *J. Alloys Compd.* **2025**, *1020*, 179544. https://doi.org/10.1016/j.jallcom.2025.179544.
158. Liu, Q.S.; An, H.W.; Wang, X.F.; et al. Effective transport network driven by tortuosity gradient enables high-electrochem-active solid-state batteries. *Natl. Sci. Rev.* **2023**, *10*, nwac272. https://doi.org/10.1093/nsr/nwac272.
159. Han, F.; Zhang, S.; Xia, J.; et al. Ultra-high rate and long cycle life sodium-based dual-ion batteries enabled by Li_2TiO_3-modified cathode-electrolyte-interphase. *Energy Storage Mater.* **2025**, *74*, 103912. https://doi.org/10.1016/j.ensm.2024.103912.
160. Zhao, Q.; Butt, F.K.; Guo, Z.; et al. High-voltage P2-type manganese oxide cathode induced by titanium gradient modification for sodium ion batteries. *Chem. Eng. J.* **2021**, *403*, 126308. https://doi.org/10.1016/j.cej.2020.126308.
161. Sun, S.; Rui, B.; Tan, X.; et al. Effects of electrolyte, state of charge, and strain rate on the mechanical properties of lithium-ion battery electrodes and separators. *J. Mater. Chem. A* **2025**, *13*, 20673–20687. https://doi.org/10.1039/d5ta02137e.
162. Huang, Z.; Jiang, F.; Li, F.; et al. Towards high-performance cathodes: Concentration gradient structure design for lithium-ion batteries and sodium-ion batteries. *Energy Storage Mater.* **2026**, *86*, 105017. https://doi.org/10.1016/j.ensm.2026.105017.
163. Zhou, H.; Gao, L.T.; Li, Y.; et al. Electrochemical performance of lithium-ion batteries with two-layer gradient electrode architectures. *Electrochim. Acta* **2024**, *476*, 143656. https://doi.org/10.1016/j.electacta.2023.143656.
164. Wang, X.; Chen, Z.; Liu, S.; et al. Anode interphase design for fast-charging lithium-based rechargeable batteries. *Energy Environ. Sci.* **2025**, *18*, 2648–2667. https://doi.org/10.1039/d4ee06107a.
165. Wang, Z.; Dai, C.; Chen, K.; et al. Perspectives on strategies and techniques for building robust thick electrodes for lithium-ion batteries. *J. Power Sources* **2022**, *551*, 232176. https://doi.org/10.1016/j.jpowsour.2022.232176.
166. Shen, X.; Yu, H.; Ben, L.; et al. High energy density in ultra-thick and flexible electrodes enabled by designed conductive agent/binder composite. *J. Energy Chem.* **2024**, *90*, 133–143. https://doi.org/10.1016/j.jechem.2023.10.052.
167. Ouyang, M.; Guo, Z.; Salinas-Farran, L.E.; et al. High-areal-capacity Na-ion battery electrode with high energy and power densities by simultaneous electrospinning-spraying fabrication. *Energy Environ. Sci.* **2025**, *18*, 6764–6779. https://doi.org/10.1039/d5ee01444a.
168. Du, M.; Hao, Z.L.; Liu, Y.; et al. Architecture Engineering for Thick Electrodes in High-Energy Batteries: Challenges and Strategies. *ACS Appl. Mater. Interfaces* **2025**, *17*, 19230–19246. https://doi.org/10.1021/acsami.5c00264.
169. Park, J.; Kim, J.; Kim, J.; et al. Sustainable and cost-effective electrode manufacturing for advanced lithium batteries: The roll-to-roll dry coating process. *Chem. Sci.* **2025**, *16*, 6598–6619. https://doi.org/10.1039/d5sc00059a.
170. Bouguern, M.D.; Reddy, A.K.M.R.; Li, X.; et al. Engineering Dry Electrode Manufacturing for Sustainable Lithium-Ion Batteries. *Batteries* **2024**, *10*, 39. https://doi.org/10.3390/batteries10010039.
171. Lee, K.H.; Shim, H.; Lee, S.H.; et al. Dual-fibrous PTFE structure enabling uniform and thick dry electrodes for high-energy-density and long-lasting batteries. *Energy Environ. Sci.* **2025**, *18*, 8446–8461. https://doi.org/10.1039/d5ee03240g.
172. Hong, J.; Yoon, J.; Park, J.W.; et al. Optimization of PTFE fibrillation in dry electrode process for scalable all-solid-state battery manufacturing. *J. Power Sources* **2025**, *655*, 237925. https://doi.org/10.1016/j.jpowsour.2025.237925.
173. Zhang, K.; Li, D.; Wang, X.; et al. Dry Electrode Processing Technology and Binders. *Materials* **2024**, *17*, 2349. https://doi.org/10.3390/ma17102349.
174. Choi, J.; Polyzos, G.; Humphrey, H.E.; et al. Long carbon fibers boost performance of dry processed Li-ion battery electrodes. *J. Power Sources* **2025**, *640*, 236603. https://doi.org/10.1016/j.jpowsour.2025.236603.
175. Asrafali, S.P.; Periyasamy, T.; Kim, S.C. Rapid Transformation in Wetting Properties of PTFE Membrane Using Plasma Treatment. *Polymers* **2023**, *15*, 3874. https://doi.org/10.3390/polym15193874.
176. Kühn, J.; Schmidt, F.; Seete, P.; et al. Towards Scalable Production of Sodium-Ion Batteries: Solvent-Free Layered-Oxide Cathodes and Aqueous-Processed Hard Carbon Anodes for Cost-Effective Full-Cell Manufacturing. *Batter. Supercaps* **2025**, *8*, e202400572. https://doi.org/10.1002/batt.202400572.
177. Kim, B.; Yoo, Y. Dry-Electrode Manufacturing for High-Energy Lithium-Ion Batteries: Principles, Advances, and Challenges. *Elastomers Compos.* **2025**, *60*, 39–50. https://doi.org/10.7473/EC.2025.60.1.39.
178. Schumm, B.; Dupuy, A.; Lux, M.; et al. Dry Battery Electrode Technology: From Early Concepts to Industrial Applications. *Adv. Energy Mater.* **2025**, *15*, 2406011. https://doi.org/10.1002/aenm.202406011.
179. Zhang, L.; Yu, J. Computer-aided thermal energy storage research of electric vehicle battery thermal management system. *Therm. Sci.* **2025**, *29*, 4157–4165. https://doi.org/10.2298/tsci2506157z.

180. Zhan, S.; Liang, L.; Li, Z.; et al. Topology optimization of liquid cooling plate for lithium battery heat dissipation based on a bionic leaf-vein structure. *Int. J. Heat Mass Transf.* **2024**, *231*, 125898. https://doi.org/10.1016/j.ijheatmasstransfer.2024.125898.
181. Zhan, S.; Shi, X.; Liu, Y.; et al. Topology optimization of a new leaf-vein type bionic channel liquid-cooling plate for lithium batteries. *Int. J. Heat Fluid Flow.* **2025**, *116*, 109932. https://doi.org/10.1016/j.ijheatfluidflow.2025.109932.
182. Zhang, X.; Luo, S.; Wu, Y.; et al. Research progress of composite phase change materials for thermal management and thermal runaway protection of lithium-ion batteries. *Energy Storage Sci. Technol.* **2025**, *14*, 1040–1053. https://doi.org/10.19799/j.cnki.2095-4239.2025.0137.
183. Yang, Z.L.; Walvekar, R.; Wong, W.P.; et al. Advances in phase change materials, heat transfer enhancement techniques, and their applications in thermal energy storage: A comprehensive review. *J. Energy Storage* **2024**, *87*, 111329. https://doi.org/10.1016/j.est.2024.111329.
184. Liu, F.; Wang, J.; Wang, F.; et al. Battery thermal safety management with form-stable and flame-retardant phase change materials. *Int. J. Heat Mass Transf.* **2024**, *218*, 124764. https://doi.org/10.1016/j.ijheatmasstransfer.2023.124764.
185. He, R.; Cai, C.; Li, S.; et al. Enhancing Electrode Performance through Triple Distribution Modulation of Active Material, Conductive Agent, and Porosity. *Small* **2024**, *20*, 2311044. https://doi.org/10.1002/smll.202311044.
186. Kotronia, A.; van Ekeren, W.W.A.; Asfaw, H.D.; et al. Impact of Binders on Self-Discharge in Graphite Dual-Ion Batteries. *Electrochem. Commun.* **2023**, *146*, 107424. https://doi.org/10.1016/j.elecom.2022.107424.
187. Lin, X.; Chen, A.; Yang, C.; et al. A Room-Temperature Self-Healing Liquid Metal-Infilled Microcapsule Driven by Coaxial Flow Focusing for High-Performance Lithium-Ion Battery Anode. *Small* **2024**, *20*, 2307071. https://doi.org/10.1002/smll.202307071.
188. Long, X.; Xie, L.; Huang, C.; et al. Self-Healing Ion-Conductive Binder for High-Performance SiO_x Anodes in Lithium-Ion Batteries. *ACS Appl. Mater. Interfaces* **2025**, *17*, 53402–53412. https://doi.org/10.1021/acsami.5c11054.
189. Xian, J.; Jiao, J.; Yi, C.; et al. The synergistic optimization of the LA133 binder and electrode interface using sodium lignosulfonate comprehensively enhances the electrochemical performance of sodium-ion batteries. *J. Energy Storage* **2025**, *135*, 118403. https://doi.org/10.1016/j.est.2025.118403.
190. Yao, Z.; Yin, R.; Peng, Q. A review on thermal management system and employed biomimetic technology to enhance lithium-ion battery packs for electric vehicles. *J. Energy Storage* **2025**, *111*, 115399. https://doi.org/10.1016/j.est.2025.115399.
191. Shi, Y.; Gao, F.; Xie, Y.; et al. In Situ interlocked gradient adaptive network binder with robust adhesion and cycle performance for silicon anodes. *J. Power Sources* **2023**, *580*, 233267. https://doi.org/10.1016/j.jpowsour.2023.233267.
192. Dubarry, M.; Howey, D.; Wu, B.; et al. Enabling battery digital twins at the industrial scale. *Joule* **2023**, *7*, 1134–1144. https://doi.org/10.1016/j.joule.2023.05.005.
193. Zhao, Y.; Du, H.; Kang, Y.; et al. Spent battery regeneration for better recycling. *Nat. Rev. Mater.* **2025**, *10*, 722–724. https://doi.org/10.1038/s41578-025-00816-z.
194. Yao, A.; Benson, S.M.; Chueh, W.C. Critically assessing sodium-ion technology roadmaps and scenarios for techno-economic competitiveness against lithium-ion batteries. *Nat. Energy* **2025**, *10*, 404–416. https://doi.org/10.1038/s41560-024-01701-9.
195. Ruppert, J.; Voß, P.; Ihlbrock, L.; et al. Analyzing material and production costs for lithium-ion and sodium-ion batteries using process-based cost modeling—CellEst 3.0. *J. Power Sources Adv.* **2025**, *36*, 100190. https://doi.org/10.1016/j.powera.2025.100190.
196. Mariyappan, S.; Desai, P.; Morcrette, M.; et al. From lab to market with sustainable sodium-ion batteries. *Nat. Sustain.* **2026**, *9*, 360–371. https://doi.org/10.1038/s41893-025-01701-x.
197. Zhang, L.; Huang, S.; Ding, Y.; et al. Research progress in the preparation of sodium-ion battery anode materials using ball milling. *RSC Adv.* **2025**, *15*, 6324–6341. https://doi.org/10.1039/d4ra08061k.
198. Marangon, V.; Bischof, K.; Regalado, A.A.; et al. Cell design and chemistry of commercial sodium-ion battery cells. *J. Power Sources* **2025**, *634*, 236496. https://doi.org/10.1016/j.jpowsour.2025.236496.
199. Wang, Y.; Bian, M.; Chen, Y.; et al. Recycling waste cotton into C@SiO_x/$MoSe_2$@CS@CF composites: Design, synthesis and high-performance sodium-ion battery anode applications. *Electrochim. Acta* **2025**, *543*, 147545. https://doi.org/10.1016/j.electacta.2025.147545.
200. Wu, Y.; Wang, B.; Luo, Z.; et al. High-Voltage Sodium-Ion Batteries: Challenges and Design Strategies. *Adv. Funct. Mater.* **2025**, *35*, 2506098. https://doi.org/10.1002/adfm.202506098.
201. Dreyer, S.L.; Maddar, F.M.; Kondrakov, A.; et al. Elucidating Gas Evolution of Prussian White Cathodes for Sodium-ion Battery Application: The Effect of Electrolyte and Moisture. *Batter. Supercaps* **2024**, *7*, e202300595. https://doi.org/10.1002/batt.202300595.
202. Muneer, W.; Khan, M.I.; Shah, S.K.; et al. Advances in prussian blue analogues: A comprehensive review on synthesis methods and battery applications. *Mater. Chem. Phys.* **2025**, *332*, 130248. https://doi.org/10.1016/j.matchemphys.2024.130248.
203. Gharat, V.V.; Yadav, M.D. Recent progress of Prussian white analogues as cathode active material for sodium-ion battery. *J. Alloys Compd.* **2025**, *1039*, 183244. https://doi.org/10.1016/j.jallcom.2025.183244.

204. Jia, S.; Zhang, B.; Gao, J.; et al. Biomass-derived hard carbon anodes: From structural engineering to industrial sodium-ion battery applications. *Energy Storage Mater.* **2025**, *80*, 104420. https://doi.org/10.1016/j.ensm.2025.104420.
205. Huang, Z.; Zhong, L.; Huang, J.; et al. Closed pore engineering of hard carbons toward remarkable sodium-ion storage. *J. Power Sources* **2025**, *654*, 237847. https://doi.org/10.1016/j.jpowsour.2025.237847.
206. Zhou, L.; Cui, Y.; Niu, P.; et al. Biomass-derived hard carbon material for high-capacity sodium-ion battery anode through structure regulation. *Carbon* **2025**, *231*, 119733. https://doi.org/10.1016/j.carbon.2024.119733.
207. Qu, X.; Yu, X.; Liao, Y.; et al. Structural regulations of biomass-derived hard carbon for high-performance sodium-ion batteries. *J. Power Sources* **2025**, *654*, 237786. https://doi.org/10.1016/j.jpowsour.2025.237786.
208. Lin, W.; Min, W.; Zhang, Q.; et al. Bimetallic co-doping strategy for layered oxides in high-performance sodium-ion batteries. *J. Colloid Interface Sci.* **2026**, *702*, 138985. https://doi.org/10.1016/j.jcis.2025.138985.
209. Shakourian-Fard, M.; Ghenaatian, H.R.; Pasban, S.; et al. In silico navigation of Na^+ ion solvation in deep eutectic solvents to propel the next wave of sodium-ion battery electrolytes. *J. Mater. Chem. A* **2025**, *13*, 33442–33456. https://doi.org/10.1039/d5ta03220b.
210. Jiang, J.; Guo, C.; Ali, S.; et al. Understanding the stabilizing effect of K^+ on the sodium manganese hexacyanoferrate for sodium-ion batteries. *Nano Energy* **2024**, *129*, 110007. https://doi.org/10.1016/j.nanoen.2024.110007.
211. Wei, R.; Lu, Y.; Ren, W.; et al. Enhancing reversible Na-ion intercalation by introducing K-ions into layered vanadyl phosphate for sodium-ion battery cathodes. *J. Phys. Energy* **2024**, *6*, 025022. https://doi.org/10.1088/2515-7655/ad3c27.
212. Zhu, Q.; Wang, J.; Wu, L.; et al. A >200 Wh kg^{-1} anode-free Na pouch battery at −40 °C enabled by manipulating electrolyte equilibrium. *Natl. Sci. Rev.* **2025**, *12*, nwaf124. https://doi.org/10.1093/nsr/nwaf124.
213. Zhang, X.; Yang, S.; Deng, C.; et al. Selective recovery of metals in spent batteries by electrochemical precipitation to cathode material for sodium-ion batteries. *Heliyon* **2024**, *10*, e27127. https://doi.org/10.1016/j.heliyon.2024.e27127.
214. Zhang, J.; Wang, Y.; Kang, Y.; et al. Cathode Recycling of Spent Sodium Ion Batteries. *Energy Mater. Adv.* **2024**, *5*, 0128. https://doi.org/10.34133/energymatadv.0128.
215. Joo, J.; Moon, J.K.; Jang, Y. A study on the desalination process for high-concentration Na_2SO_4 using pilot-scale bipolar membrane electrodialysis. *Desalin. Water Treat.* **2025**, *322*, 101222. https://doi.org/10.1016/j.dwt.2025.101222.
216. Ye, N.; Yan, T.; Jiang, Z.; et al. A review: Conventional and supercritical hydro/solvothermal synthesis of ultrafine particles as cathode in lithium battery. *Ceram. Int.* **2018**, *44*, 4521–4537. https://doi.org/10.1016/j.ceramint.2017.12.236.
217. Liu, S.; Zhou, W.; Song, X.D.; et al. Hard carbons prepared by a salt-assisted hydrothermal method as anodes for the sodium-ion battery. *New Carbon Mater.* **2025**, *40*, 346–354. https://doi.org/10.1016/s1872-5805(25)60954-1.
218. Zhang, C.; Wang, Y.; Sun, H. Dry-coating electrode fabrication for sustainable, high-performance batteries. *Sci. China Chem.* **2025**, *68*, 6391–6402. https://doi.org/10.1007/s11426-025-3119-x.
219. Zhou, H.; Yu, Y.; Wang, K.; et al. A YOLOv8-Based Approach for Real-Time Lithium-Ion Battery Electrode Defect Detection with High Accuracy. *Electronics* **2024**, *13*, 173. https://doi.org/10.3390/electronics13010173.
220. Nozarijouybari, Z.; Fathy, H.K. Machine learning for battery systems applications: Progress, challenges, and opportunities. *J. Power Sources* **2024**, *601*, 234272. https://doi.org/10.1016/j.jpowsour.2024.234272.
221. Kim, S.; Lee, H.; Lim, J.; et al. Digital Twin Battery Modeling and Simulations: A New Analysis and Design Tool for Rechargeable Batteries. *ACS Energy Lett.* **2024**, *9*, 5225–5239. https://doi.org/10.1021/acsenergylett.4c01931.
222. Kausthubharam; Vishnugopi, B.S.; Sengupta, A.; et al. Perspective on Thermal Stability and Safety of Sodium-Ion Batteries. *ACS Energy Lett.* **2025**, *10*, 5383–5397. https://doi.org/10.1021/acsenergylett.5c02345.
223. National Development and Reform Commission; National Energy Administration. *Implementation Plan for the Development of New Energy Storage during the 14th Five-Year Plan Period (in Chinese)*; NEA: Beijing, China, 2022.
224. European Commission. *Battery 2030+ Roadmap 2024–2030*; Publications Office of the European Union: Luxembourg, 2024.
225. U.S. Department of Energy. *Bipartisan Infrastructure Law: Battery Material Processing and Manufacturing Grants*; DOE: Washington, DC, USA, 2023.
226. Gan, S.; Zeng, X.; Liu, D.; et al. Direct upcycling of spent layered oxide cathodes via a dual-functional eutectic salt for sodium-ion batteries. *J. Mater. Chem. A* **2025**, *13*, 24880–24888. https://doi.org/10.1039/d5ta02389k.
227. Li, H.; Wu, F.; Wang, J.; et al. Anode-free sodium metal batteries: Optimisation of electrolytes and interphases. *Energy Environ. Sci.* **2025**, *18*, 3887–3916. https://doi.org/10.1039/d5ee00136f.
228. Li, A.M.; Pollard, T.P.; Wang, Z.; et al. Non-fluorinated electrolyte for high-voltage anode-free sodium metal battery. *Nat. Sustain.* **2026**, *9*, 306–316. https://doi.org/10.1038/s41893-025-01710-w.
229. Liu, L.; Cai, Z.; Yang, S.; et al. Multifunctional High-Entropy Alloy Nanolayer Toward Long-Life Anode-Free Sodium Metal Battery. *Adv. Mater.* **2025**, *37*, 2413331. https://doi.org/10.1002/adma.202413331.
230. Shi, J.; Wang, D.; Liu, Q.; et al. Intermetallic Layers with Tuned Na Nucleation and Transport for Anode-Free Sodium Metal Batteries. *Nano Lett.* **2025**, *25*, 1800–1807. https://doi.org/10.1021/acs.nanolett.4c04282.

231. Alzamer, H.; Jaafreh, R.; Kim, J.G.; et al. Artificial Intelligence and Li Ion Batteries: Basics and Breakthroughs in Electrolyte Materials Discovery. *Crystals* **2025**, *15*, 114. https://doi.org/10.3390/cryst15020114.
232. Meng, K.; Bai, K.; Sun, S.; et al. Artificial intelligence driven design of cathode materials for sodium-ion batteries using graph deep learning method. *J. Energy Storage* **2024**, *101*, 113809. https://doi.org/10.1016/j.est.2024.113809.
233. Cong, J.; Luo, S. Artificial intelligence empowering innovation in key materials for sodium-ion batteries: Machine learning driven design and optimization of cathode and anode materials. *J. Energy Chem.* **2026**, *116*, 434–453. https://doi.org/10.1016/j.jechem.2026.01.011.